Department of Mathematics
Imperial College London
180 Queen's Gate London, SW7 2AZ

Gait optimality for undulatory locomotion with applications to *C. elegans* phenotyping

Madeleine Grace Hall

Thesis submitted in partial fulfilment
of the requirements for the degree of
Doctor of Philosophy
and the Diploma of the
Imperial College of Science, Technology and Medicine

12 May 2022

Supervisors:

Dr. Eric E. Keaveny,
Imperial College London

Dr. André E. X. Brown,
Medical Research Council London Institute of Medical Sciences (MRC LMS)

External Examiner:

Professor Netta Cohen,
University of Leeds

Internal Examiner:

Professor Mauricio Barahona,
Imperial College London

Statement of originality

I, Madeleine Hall, declare that the work contained in this thesis is my own, or else is appropriately referenced. Any material for which I am not responsible is explicitly indicated by the appropriate use of references and citations.

Copyright declaration

Acknowledgements

Firstly, I would like to thank you for reading this thesis.

I would like to thank my supervisors for their academic expertise, guidance, and encouragement throughout the course of this research degree. Thank you to Eric Keaveny for providing invaluable mathematical and technical insight throughout this research, as well as general support, patience and advice. And thank you to André Brown for providing me with the opportunity to expand my experimental knowledge, for sharing scientific expertise and enthusiasm through many enjoyable discussions, and for encouraging my resilience and perseverance throughout the past few years.

Many thanks go to my examiners Netta Cohen and Mauricio Barahona. I am grateful for the consideration of the thoughts, ideas, and research on these pages.

It has been a privilege to undertake such a highly interdisciplinary research project, and to have been a part of two research groups here at Imperial. I am grateful to other researchers in the Department of Mathematics who have profoundly shaped my experience as a PhD student: thanks to Emily for the early morning swims in the Serpentine, to other members of Eric's research group over the years, and to occupiers of Huxley 730/731 past and present. I am also grateful to members past and present of the Behavioural Phenomics group at the Institute of Clinical Sciences. Thank you for welcoming me and making me feel like a part of the lab. In particular, thanks to Ida and Tom for collecting the worm data analysed in the second part of this thesis, and thanks to Luigi for consistent coding-related support.

This research was funded by the Wellcome Trust (grant number 215345/Z/19/Z), and I would like to thank them for providing me with the means to undertake this PhD. I am forever grateful to have been a part of the 2017 Theoretical Systems Biology and Bioinformatics PhD cohort along with Tara, Jonathan, Heather, and Léonie. I cannot imagine this journey without you, and I am so proud of all of us. You all inspire me, and I look forward to seeing your bright futures unfold.

I would like to thank Adam Townsend for graciously reviewing draft copies of this thesis, and for being a mentor and a friend.

Lastly, I would like to thank my family. Thanks to my parents and siblings for their unconditional love and support, and for shaping me into the person I am today. And thank you to Ronan for being my teammate — since the beginning of this endeavour we have celebrated the highs together, and your support has kept me going through the lows. Thank you for always believing in me.

Abstract

This thesis focuses on the optimality and efficiency of organism locomotion strategies, specifically of microscopic undulators, in two distinct parts. Undulators locomote by propagating waves of bending deformation along their bodies, and at the microscale (ie low Reynolds number) interactions between undulators and their surroundings are well-described by biomechanical models due to high viscosity and negligible inertia. Frameworks such as resistive force theory enable the determination of optimal gaits for micro-undulators, often defined as the waveform maximising the ratio of swimming speed to energetic cost.

Part I explores this avenue of research in a theoretical setting. Primary mathematical focus has been on finding optimal waveforms for straight-path forwards locomotion, but organisms do not move exclusively this way: turning and manoeuvring is key to survival. Here we establish a mathematical model, extending previous approaches to modelling swimming micro-undulators, now introducing path curvature, to obtain optimal turning gaits. We obtain an analytical result demonstrating that high-curvature shapes minimise energetic cost when the penalty for bending is reduced. Imposing limitations on the curvature, and investigating multiple high-dimensional shape-spaces, we show that optimal turning results can be closely approximated as constant-curvature travelling waves.

Part II adopts an experimental approach. Quantitative phenotyping tools can be used in behavioural screens of the model organism *C. elegans* to detect differences between wildtype and mutant strains. Expanding the current set of tools to include more orthogonal features could enable increased detection of deficiencies. Here we develop efficiency as a phenotyping lens for *C. elegans*, quantifying the gait optimality of rare human genetic disease model strains. Genetic diseases in humans are modelled in *C. elegans* with disease-associated orthologs. We find worm gait efficiency is found to correlate highly with percentage time paused. High efficiencies are exhibited during reversals and backing motions, due to suppressed head-swinging and increase in speed.

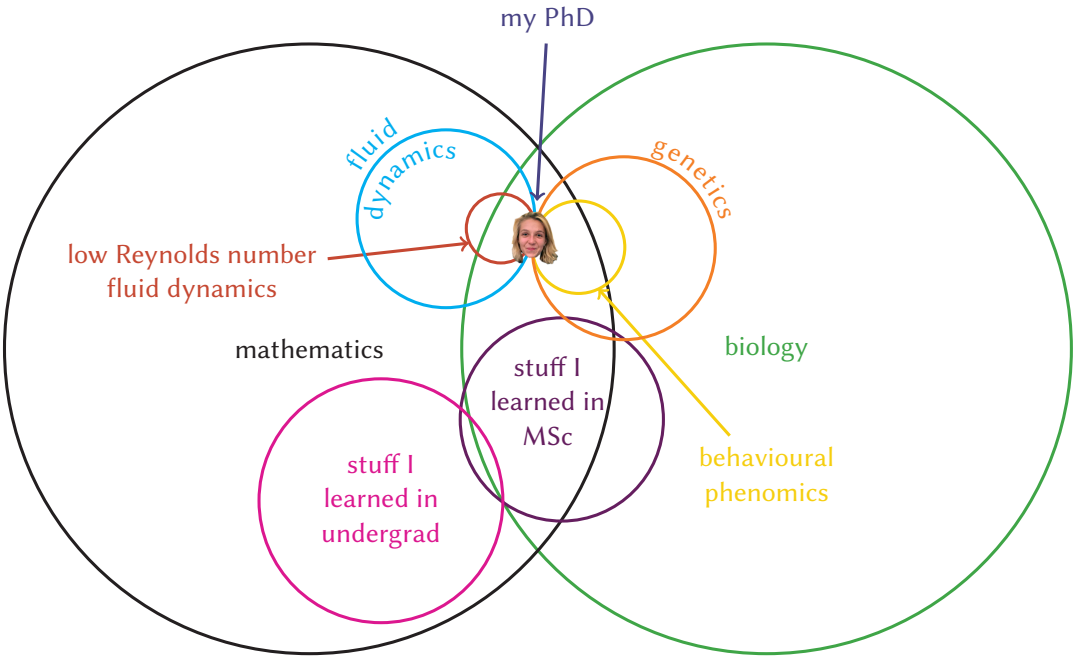
my PhD
fluid dynamics
genetics
low Reynolds number fluid dynamics
mathematics
biology
stuff I learned in MSc
stuff I learned in undergrad
behavioural phenomics

Figure 0

Contents

List of Tables

List of Figures

Chapter 1

Introduction

1.1 Motivation

All types of organisms on this planet maintain their existence by means of reproduction, growth, development, and maintenance. In addition, responding to stimuli (averse or otherwise) is also key to survival. Many organisms can engage in these existential activities without motility (eg trees, corals, sponges). However, for a vast number of organisms the ability to self-locomote is crucial to staying alive. Many organisms need to move to find food, to find a suitable habitat, to seek a mate, or to avoid aversive stimuli such as toxins or predators. Even for some sessile organisms, there is a motile stage during development. Motility is therefore essential for survival for many species, and evolutionary processes have thus shaped the locomotion strategies that motile organisms employ when traversing their surroundings.

One such strategy is undulatory locomotion, which is motion characterised by the propagation of waves along an often long, slender body. This wave-like movement pattern exists across all scales to generate organism propulsion through a variety of different media: from snakes on sand and eels in the ocean, to nematodes

on agar and spermatozoa in mucus. The prominence of undulatory locomotion across life is evidence of the effectiveness of this particular movement strategy, and thus has inspired many man-made devices in technology and robotics. Bio-inspired robots have been designed to employ this undulatory movement strategy across a wide range of applications and scales. From the microscale for medical diagnosis and drug delivery in precision medicine [1], to the macroscale for searching for victims in rubble-composed disaster sites [2], biomimetic design is becoming increasingly popular in modern robotics, often taking inspiration from undulatory gaits exhibited by organisms in nature [3].

Underlying both design in robotics, and also metabolism in organism motility, is an energetic cost associated with such undulatory motions. To build an efficient robot, designers can seek to attain maximum functionality per unit power input. Likewise, for many organisms it is preferable to achieve the required displacement for survival (eg to find food), while conserving as much energy as possible. Biologically, there is a cost associated with this kind of motion, and thus one of the avenues of research is understanding that cost, how it can be optimised for manoeuvrability, and how this impacts the gaits that are exhibited by these undulatory organisms.

The avenue of research on efficient organism locomotion spans across a broad range of scales (from snakes and eels at the macroscale to nematodes and flagellates at the microscale), and also spans across a broad range of definitions of 'efficiency'. How we mathematically define the energetic cost of locomotion, and how this might differ between different modes of motion (eg moving forwards, reversing, turning), as well as differ between different organisms or different strains of organism depending on their physiological properties, is an active area of research. The focus of this thesis is at the microscale, and this thesis is split into two related by distinct parts which respectively explore these theoretical mathematical approaches and differences between optimality in individuals. The overarching motivation across both parts is to expand the current understanding of optimality

and efficiency of microscale undulatory locomotion. This is done by extending the current mathematical approaches to previously unconsidered motion modes (undulatory turning strategies) in Part I, and then investigating behavioural differences across models of Mendelian genetic diseases in *C. elegans* in Part II.

C. elegans is a model organism that is used extensively across a wide breadth of scientific research areas. It is a microscopic worm (approximately 1mm long) and locomotes by propagating planar waves along the length of its body. It has an extremely well-characterised nervous system [4,5], and the ability to perform genetic perturbations on this animal [6,7] combined with the excellent availability of large datasets characterising its movement patterns to a high resolution make it an excellent opportunity for studying organism gait efficiency.

1.2 Thesis outline

This thesis explores this avenue of optimal undulatory locomotion in two parts. Part I lies in the realms of mathematical biofluid dynamics and computational micromechanics, addressing the question of optimal undulatory locomotion — initially for straight-path forwards locomotion in chapter 2, and then for novel considerations of undulatory turning in chapter 3. Part II addresses the question of optimal undulatory locomotion in an experimental setting, applying gait efficiency as a phenotyping tool in a *C. elegans* behavioural screen in chapter 4.

Part I

The anatomical simplicity and elegant wave-like movement patterns of undulatory organisms inherently lends themselves to mathematical analysis. Developing a mathematical framework to describe this type of movement is an active area of research, and many models have been devised to further understanding of how

undulatory organisms traverse their surroundings. In particular, at the microscopic scale where these organisms live in a world of high viscosity and negligible inertia (termed "low Reynolds number"), the simplification of the associated hydrodynamics allows for rigorous theoretical analysis of the fluid mechanical forces involved in swimming micro-undulation. Chapter 2 provides an overview of the mathematics of low Reynolds number undulatory locomotion, and quantitatively replicates results from the literature for optimal straight-path forwards undulatory motion for planar undulations. The optimal undulatory gait in this chapter is defined as the shape which maximises a generalised swimming efficiency function, which includes a dimensionless parameter allowing for variation in the relative importance of energetic cost for bending versus energetic cost due to dissipation.

We are explicit in saying straight-path undulatory movement above because, for the vast majority of the literature concerning planar undulations, the focus of the mathematical models has been emphatically for the case of straight-path forwards motion of these organisms. There exists a gap in the literature for the consideration of optimal turning strategies of these undulatory organisms. To this point, one of the main focuses of this thesis is to extend current approaches to modelling optimal microscale undulatory locomotion, for the question of optimal *turning* gaits. This is addressed in chapter 3, in which optimal turning gaits for a variety of parametrisations of the shape space are obtained. The motion of a slender rigid body through a surrounding fluid of high-viscosity is analysed by the *resistive force theory* (of Gray and Hancock, 1955 [8]). This thesis considers the propagation of planar waves along the length of a microscopic slender body. The resistive force theory framework assumes that hydrodynamic forces are proportional to the local body velocity only — nonlocal forces that account for long-range hydrodynamic interactions are disregarded in this framework. This is a widely-used simplification of *slender body theory*, and neglecting nonlocal forces provides a suitable approximation for flagella locomotion in the absence of a cell body, and also for propagating waves of large amplitude (discussed in more detail in chapter 2).

The optimal undulatory turn is determined via numerical optimisation, and is defined as the body shape that minimises the energetic cost of motion (the objective function), subject to the constraint that after one wave-period the net-orientation of the body is equal to some specified turning angle (a parameter that is set prior to optimisation). The objective of the optimisation in this chapter has changed from the previous chapter: in chapter 2 we maximise a measure of efficiency, whereas in chapter 3 we minimise a measure of energetic cost. This energetic cost is precisely the denominator of the efficiency function in chapter 2. This change in objectivity allows for the consideration of reorientation strategies without inherently rewarding or penalising gaits with high velocities or large net-displacement.

The shape of the waveform is decomposed onto a finite number of modes which prescribe the shape of the body. These modes are the control parameters in the optimisation routine, which are modified at each iteration such that the objective function is optimised. Several parametrisations of the shape space are investigated: Fourier travelling waves, shapes parametrised with Chebyshev polynomials, and travelling waves of constant curvature. The optimal turning results from high-dimensional shape spaces (travelling waves and wave shapes given by Fourier series or Chebyshev polynomials) are shown to in fact be well-characterised both qualitatively and quantitatively by constant curvature waves, which are prescribed by only a two-parameter family. The approach is applied to all kinds of turns: from slight steers to sharp u-turns. The results are analysed and investigated by approximating high-dimensional shape spaces with low-dimensional families of shapes, parametrised by variables that are comparatively easily interpreted.

The optimal turning gait of a low Reynolds number undulatory organism is found to depend fundamentally on the penalty for bending since the most efficient turns require high-curvature postures. These results expand the current theoretical understanding of micro-undulatory locomotion to more complex movement behaviours, adding to the overall picture of mathematical considerations of why

these organisms move the way they do. The optimal turning results from part I pertain to the microscopic (Stokesian) regime, and can provide insight into how undulators at small scales employ reorientation strategies, from nematodes like *C. elegans* to flagellates like spermatozoa.

Part II

Part II of this thesis pertains to a different question regarding microscopic undulatory locomotion. In contrast to the theoretical and analytical questions addressed in chapters 2 and 3, chapter 4 analyses experimental data from a *C. elegans* behavioural phenotypic screen. We apply gait efficiency as a phenotyping tool in the context of human genetic disease model *C. elegans* strains. Rare genetic diseases in humans can be modelled in *C. elegans* with disease-associated genetic variants of conserved genes. Such disease models exhibit locomotion changes compared to wildtype 'healthy' worms, and these changes can be quantified in behavioural phenotypic screens. Expanding the set of current quantitative phenotypes to include more orthogonal features, like gait efficiency, is a worthwhile pursuit as it could lead to the detection of more movement defects.

It remains an open question to what extent animal gaits are optimal. We use *C. elegans* in this thesis due to the high volume of data that exists characterising its movement patterns in a variety of contexts, in order to study the question of efficiency. Specifically, we test the suitability of gait efficiency as a phenotyping tool, seeking to establish if quantitative differences can be detected between individuals in a behavioural screen.

This is tested by looking at strong genetic perturbations in the organism, and genes where disruption causes severe disease in humans might be expected to be strong perturbations. We therefore consider such human genetic disease model strains, testing efficiency as a phenotyping lens. A detailed analysis of the 25 *C. elegans* strains, each with a human genetic disease association, provides insight into

how movement differences affect the computationally determined efficiency. Parallels between resulting gait efficiencies can be drawn between strains associated with the same or similar genetic disease in humans, ultimately determining that efficiency as a *C. elegans* phenotype can yield quantitative differences between individuals in a behavioural screen.

The complex natural gaits of *C. elegans* analysed in part II are taken as given — that is, accepted as true or real representations of the animals behaviour. Due to the complexity of their movements, the quantitative measure of efficiency applied as a phenotyping lens is taken to be the most simple expression of hydrodynamic efficiency used for straight-path microscopic undulatory locomotion (introduced by Lighthill (1975) [9] and discussed in chapter 2). This is a different metric from the objective function applied in chapter 3, which contains the other main results of this thesis. To explicitly emphasise: the results from parts I and II of this thesis are presented distinctly from one another, and little intersection between the main results of this thesis exists.

The data analysed in part II of this thesis is a recently-obtained dataset in the Behavioural Phenomics lab, within the Medical Research Council London Institute of Medical Sciences (MRC LMS). Data is unpublished at time of submission of this thesis (May 2022). Experimental (wet lab) methods were performed by Ida Barlow and Tom O'Brien. The data was collected using state-of-the-art imaging systems which allows for multiple worms to be tracked in parallel and the collection of high-quality imaging data. Analysis of the worm videos obtained was performed using the Tierpsy Tracker software (developed and maintained by the Behavioural Phenomics lab, MRC LMS) [10, 11]. Feature extraction and gait optimality features were obtained with novel computational pipelines constructed by Madeleine Hall in the MATLAB programming platform. The advantage of analysing this particular dataset in this thesis lies solely in its availability and recentness of acquisition within the lab — no assumptions of optimality or efficiency across any of the strains are imposed.

1.3 Contributions of this thesis

This thesis is the outcome of a highly interdisciplinary research degree seeking to apply resistive force theory and principles from low Reynold's number hydrodynamics to understand the locomotion of microscopic undulatory organisms, an example of which is given by the model organism, the nematode worm *C. elegans*. The results presented in parts I and II respectively in this thesis, whilst related, are distinct, and investigate two different questions pertaining to the overall theme of microorganism gait efficiency.

1.3.1 Part I

Previously there has been extensive work on how microscopic undulators can move optimally in straight lines. Given how obviously important changing direction is for animals, there is surprisingly little research and consideration on how undulators can turn optimally. Part I of this thesis makes fundamental contributions to our understanding of optimal turning, including the interesting discovery that simply propagating a wave of constant curvature (about the simplest way of implementing a turn for an undulator) is close to optimal. The simplicity of this insight is likely to spur further work and find applications in slender robotics, as well as lend insight towards the broader question of how and why organisms move the way they do.

1.3.2 Part II

Part II of this thesis applies resistive force theory and principles from low Reynold's number hydrodynamics to derive new features that are applied to quantify the behaviour of *C. elegans* worm models of Mendelian genetic diseases. These new features improve our ability to detect so-called worm "symptoms" of these human disease mutations. Identifying behavioural differences in the disease models is

the first step in understanding the function of the disease genes and in designing drug screens to search for treatments.

Part I

Chapter 2

Optimal undulatory locomotion at low Reynolds number

2.1 Introduction

This chapter covers the mathematical background, model, and results for optimal undulatory locomotion at low Reynolds number. We begin with a review of the key literature pertaining to this part of the thesis, which includes an introduction of the fluid dynamics associated with microscopic undulatory locomotion, outlining key results and theories which fundamentally underpin our model framework. This includes considerations of optimising undulatory locomotion such that the most efficient gait can be determined, based on a mathematically defined measure of efficiency.

In this thesis, as in many studies in this area of research, we prescribe a given undulatory shape or beat pattern (ie gait) to our theoretical micro-undulator. Then the propulsive velocity, rate of working against the surrounding fluid, and distribution of applied viscous bending moments along the slender body can be calculated. The *optimality* of the gait can then be determined from these values. Here the no-

tion of optimality specifically refers to incurring the lowest possible mechanical cost (or energy dissipation) for a given movement. The most *efficient* gait can be defined as the undulation that maximises the ratio of propulsive velocity to this energy dissipation. The rate of working against the surrounding fluid (the hydrodynamic cost) describes the force required by the body to distort its surroundings in order to move. At the microscale, the hydrodynamic cost plays a dominant role in the overall cost of moving, due to these organisms experiencing high viscosity, and therefore high resistance in their surroundings. To illustrate this, you can imagine the difference in effort required between walking through a large vessel of honey versus walking across a field (ie through air). Aside from any differences in difficulty breathing between these two scenarios, in the high-viscosity scenario (the honey) the energy you spend distorting the fluid contributes dominantly to the overall cost of moving. This contrasts the scenario of walking through air, where the viscosity is orders of magnitude less, and thus the hydrodynamic cost of distorting the surroundings in negligible.

Of course, the way to minimise the hydrodynamic cost associated with distorting the fluid surrounding the body is to not distort it at all. That is, remaining completely still and not changing shape at all incurs no hydrodynamic cost, since no effort is being made to push against the surrounding fluid. For micro-undulators, if we also account for the cost associated with distorting the body (as it is reasonable to assume that there is a cost for bending and assuming high-curvature shapes), this means that the gait which minimises the mechanical cost is a completely still, straight posture. This gait of course is not optimal in many senses, as no net motion is incurred, and the organism is not navigating through its surroundings seeking food, a mate, etc. The most *efficient* gait can therefore be determined by minimising this mechanical cost, whilst maximising the propulsive velocity or net motion of the organism. That is, the most efficient gait maximises the ratio of the propulsive velocity to the mechanical cost of moving.

To this point and this particular definition of ‘optimal’ gait, it is of course the

case that not all costs associated with locomotion are purely hydrodynamical or mechanical. There is, for example, a metabolic cost associated with an organism moving through its surroundings. There are many possible notions of optimality — being alive is a multi-objective function. That being said, in this thesis we consider only the mechanical cost of locomotion (capturing the hydrodynamical cost and bending cost) for these micro-undulators.

We present a hydrodynamical model, laying out the kinematic framework which describes the motion of our theoretical undulatory microswimmer, and apply resistive force theory (Gray and Hancock (1955) [8]) to model the interactions between the body and the surrounding fluid. Optimising over a quantitative measure of efficiency, we present the optimal gait for a micro-undulator swimming forwards. This chapter replicates existing results in the literature (Ligthill (1975) [9], Spagnolie and Lauga (2010) [12]) using a numerical approach with an independently-developed code framework. The results presented in this chapter align with and agree with those from the literature.

2.2 Background

The following section provides a review of literature covering key results relating to the study of microscopic undulatory locomotion, and the optimality thereof. This literature underpins the results presented in this thesis. Across the literature, and in this thesis, key assumptions regarding the theoretical micro-undulator are that it is deformable, but inextensible. We consider a planar, two-dimensional undulatory beat pattern propagating along the length of a slender body, and assume the body neither stretches nor twists about its local axis. Since all points on a particular cross-section of the body then move at approximately the same velocity, the motion of the undulating body can be described by a two-dimensional position vector, describing the shape of the body in the 2D plane.

2.2.1 Related literature

Theoretical considerations of undulatory locomotion for microscopic organisms extend back to the 1950s, in which Taylor (1951) [13], motivated by spermatozoa, analysed the swimming of microscopic organisms by considering propagating waves of lateral displacement along a thin, flexible infinite sheet. Though this geometry has little physiological relevance, it allowed a relatively straightforward solution of the Stokes equations, and the results of this analysis gave the first explanation of how a propulsive tail can move a body through a viscous fluid without relying on inertial forces.

This contribution by Taylor, along with others throughout the 1950s and 60s (including studies from Gray, Hancock, Lissman and Wallace [8, 13–16]) formulated the methods of describing the force interactions involved with long, thin bodies locomoting in a planar fashion at the microscale. Namely, it was at this time that widely used *slender body theory* and the also widely-used approximation of *resistive force theory* were developed. These theories provide the frameworks for mathematical models of undulatory microscopic locomotion, and are explained in more depth in section 2.2.2.

A pioneering publication by Pironneau and Katz (1974) [17] established that at an instant in time, a travelling wave in the direction opposite to propulsion is hydrodynamically optimal. In this study, the ideal question to address is: "Given that an organism swims from A to B in a given time, how can the total energy expenditure during this interval be minimised?" However, given that this question posed an optimal control problem of non-standard type (ie the boundaries are non-stationary), an alternative closely-related problem was solved. Starting from the fact that an organism is swimming forward in a straight line at a given rate, they considered what the most economical way of doing so is, minimising the instantaneous rate of working at each time [17]. The propulsive hydrodynamics in this analytical study are modelled by the resistive force theory of Gray

and Hancock (1955) [8]. Requiring that the rate of viscous working by the organism against the fluid be minimal at all times, the equivalent condition imposed is to minimise the global rate of instantaneous viscous dissipation in the fluid (as discussed in section 2.2.2).

Following this, implementing local analysis on the theoretical microscopic undulatory slender body, Lighthill (1975) analytically derived his famous 'saw-tooth' result as the hydrodynamically optimal shape for a flagella travelling wave [9] (the derivation of this result is discussed in more detail in section 2.2.2). In the above studies, optimality is defined as the gait that minimises the rate of working (which is equivalent to the rate of dissipation due to viscosity in the surrounding fluid) for a given rate of swimming forward (swimming speed or net motion). As discussed in the introduction, it is not only the rate of working against the surrounding fluid which contributes to the complete cost of moving. We may also include a cost for bending in the body, which is incurred due to the elastic nature of the internal structure. Recently, studies have been carried out to investigate the relationship between internal structure and hydrodynamics [18, 19]. These organisms can be considered as rod-like elastic structures which move and bend as a result of stresses that are generated internally, allowing for the cost of bending the body to be accounted for using approaches from classical elastic beam theory [20].

This approach was considered by Spagnolie and Lauga (2010) [12], who determined the optimal travelling wave shape for an elastic flagellum which maximises a *generalised* swimming efficiency. The generalised swimming efficiency was similar to Lighthill's hydrodynamic efficiency, however it also included this penalty for bending discussed above. Along with the work done by the swimmer against the surrounding fluid, there is also included an energetic cost capturing the elastic energy stored in the bending of the body, penalising high curvature shapes. When varying the importance of rate of mechanical work versus bending cost in the generalised efficiency expression, they found a regularisation of Lighthill's sawtooth

solution, and that the optimal waveform becomes increasingly sinusoidal as the importance of the bending cost increases. These results from Spagnolie and Lauga (2010) are replicated both qualitatively and quantitatively later in this chapter of the thesis, using an independently-developed code and numerical framework. This replication verifies that the novelly constructed numerical framework aligns with preexisting results.

The results from Spagnolie and Lauga (2010) were extended upon by Lauga and Eloy (2013) [21], who computationally determined the optimal travelling-wave flagellum shape, maximising the swimming speed for a fixed energetic cost. More recently, Lauga (2020) [22], for a periodic long-wavelength model of flagella, shows that the planar flagellar waves maximising the time-averaged propulsive force for a fixed amount of energy dissipation correspond to waves travelling with constant speed, ie travelling waves are hydrodynamically optimal for long-wavelength flagella.

Having discussed some of the key studies from the relevant literature, we now go on to explain the associated hydrodynamics on a more technical level. The results of these studies discussed above were derived in the context of *low Reynolds number* hydrodynamics. These microscopic undulatory organisms swim through a fluid that surrounds their bodies. In the following section we present how the flow of that fluid is modelled, what Reynolds number is, and discuss in detail how the propulsive speed, rate of working, and bending cost are determined.

2.2.2 Fluid dynamics and microscopic undulatory locomotion

Reynolds number

The flow of the fluid surrounding the swimming microorganism is governed by the incompressible Navier–Stokes equations:

$$\boldsymbol{\nabla} \cdot \boldsymbol{u} = 0 \tag{2.1}$$

$$\rho \frac{D\boldsymbol{u}}{Dt} = \boldsymbol{\nabla} \cdot \boldsymbol{\sigma} + \boldsymbol{G} \tag{2.2}$$

where $\boldsymbol{u}$ is the velocity, its material derivative $D\boldsymbol{u}/Dt$ (describing the time rate of change of the quantity) is given by

$$\frac{D\boldsymbol{u}}{Dt} = \frac{\partial \boldsymbol{u}}{\partial t} + \boldsymbol{u} \cdot \boldsymbol{\nabla} \boldsymbol{u}\,, \tag{2.3}$$

and ρ is the density, $\boldsymbol{\sigma}$ the stress tensor, and $\boldsymbol{G}$ the external forcing, all of which will be explained in more detail below. These equations assume that the fluid is Newtonian, meaning that the viscosity is flow-independent. Specifically, for a Newtonian fluid, the stress tensor $\boldsymbol{\sigma}$ — which models the stress in the fluid that is attributed to the strain rate (the rate at which the the fluid is deforming), and is the sum of the viscous stress and hydrostatic pressure — is given by

$$\boldsymbol{\sigma} = -(p\boldsymbol{I}) + \mu(\boldsymbol{\nabla} \boldsymbol{u} + (\boldsymbol{\nabla} \boldsymbol{u})^T) \tag{2.4}$$

with p the pressure, μ the viscosity, and $\boldsymbol{I}$ the identity tensor. The viscosity μ is a coefficient that relates the stress to the deformation. Viscous stresses describe the resistance to shear, which is the gradient of the velocity field. The higher the viscosity, the more resistance there is to shear.

The pair of equations that is Navier–Stokes (for an incompressible fluid) are referred to as the incompressibility equation and the momentum equation. As a

result of the incompressibility equation ($\boldsymbol{\nabla} \cdot \boldsymbol{u} = 0$), the fluid density remains constant. The momentum equation ($\boldsymbol{\nabla} \cdot \boldsymbol{\sigma} + \boldsymbol{G} = \rho D\boldsymbol{u}/Dt$) is a manifestation of Newton's second law, which is popularly referred to as "$F = ma$" ("force equals mass times acceleration").

In the momentum equation, the "acceleration" is the material derivative of the fluid velocity with respect to time, and the "mass" is described by the density of the fluid (how 'heavy' or 'concentrated' the particles are in the fluid). The forces in the momentum equation can be separated into internal forces $\boldsymbol{\sigma}$ (how the fluid is interacting with itself) and external forces $\boldsymbol{G}$ (which account for things like gravity, or electromagnetism). The internal forces are the pressure force and the viscous stress, and are captured in the expression of the stress tensor $\boldsymbol{\sigma}$. The pressure force describes the movement of particles from areas of high pressure to low pressure, and the viscosity force describes the internal friction of the fluid — the stronger the friction, the higher the viscosity. For a Newtonian fluid (meaning the viscosity is flow-independent), and under the assumption that there are no external forces (ie $\boldsymbol{G} = 0$), the momentum equation can be written as

$$\underbrace{\rho \frac{D\boldsymbol{u}}{Dt}}_{\text{“}ma\text{”}} = \underbrace{-\boldsymbol{\nabla} p + \mu \nabla^2 \boldsymbol{u}}_{\text{“}F\text{”}}, \tag{2.5}$$

where ρ is the density, $\boldsymbol{u}$ the velocity, p the pressure, and μ the viscosity.

The Reynolds number is a dimensionless number that arises from the non-dimensional form of the Navier–Stokes equations for a Newtonian fluid [23]. It can be written as

$$\mathrm{Re} = \frac{\rho L U}{\mu} \tag{2.6}$$

for an object of length L moving through the fluid at a characteristic velocity U (eg U might be the mean swimming speed of the undulator). Non-dimensionalising with typical length, time, and force scales, the momentum equation can be re-

written as

$$\mathrm{Re}\frac{D\boldsymbol{u}}{Dt} = -\boldsymbol{\nabla} p + \nabla^2 \boldsymbol{u}. \tag{2.7}$$

In the limit $\mathrm{Re} \to 0$, the above expression reduces to

$$-\boldsymbol{\nabla} p + \nabla^2 \boldsymbol{u} = 0, \tag{2.8}$$

which when paired with the incompressibility equation comprises the Stokes equations, which describe fluids for which velocities are very slow, viscosities very large, and/or length-scales very small (termed "Stokes flow"). In eq. (2.8), time has disappeared from our momentum equation, as the only term that had time associated with it was the acceleration term. This means that Stokes flow has no dependence on time other than through time-dependent boundary conditions. For a given initial condition, if a force is enacted on the fluid at one time, and the exact opposite force is enacted on the fluid at a later time, the initial condition will be exactly recovered — this property of Stokes flow is termed "time reversibility".

The Reynolds number becomes very small in environments with very large viscosity (like a person swimming in honey) or very small speeds and length scale (like a microscopic undulatory organism swimming in water). Undulators like eels, nematodes, and spermatozoa propel themselves through their environment by propagating waves along the length of their bodies, exerting a force on the surrounding fluid in order to push through the medium. At the microscale, in the low Reynolds number regime, there is instantaneous diffusion of momentum throughout the fluid, which means that inertia is negligible, and swimming stops the instant the body stops deforming. It is therefore the case that, at each instant in time, the total force acting on the microswimmer is always zero. Thus there is no coasting or drifting, and in order to keep moving through its environment a microscopic undulator must constantly deform its body in order to keep progressing through its surroundings.

This wavy undulatory locomotion strategy of organisms at the microscale regime originated due to the time-reversibility of Stokes flow. In his classic animated introduction "Life at low Reynolds number", Purcell (1977) [24] presented his renowned scallop theorem, laying out the mechanical necessity of so-called breaking of temporal symmetry in order to make progress whilst swimming at low Reynolds number. In the absence of inertia, the translation of a microscopic body is fully determined by its sequence of body postures. A scallop switches between opening its shell and closing its shell. It is able to swim through its usual (high Reynolds number) environment because it closes more rapidly than it opens, which results in a propulsive force which transports the body. However, at low Reynolds number this difference in speed of closing and opening would not generate propulsion. Simply changing its shape followed by performing the exact same motion in reverse, regardless of the speed of the manoeuvre, would result in the body returning to its exact initial starting position. Hence, the scallop cannot swim at low Reynolds number. This scallop motion is often referred to as "time-reversible deformation", as the motion is the same forwards in time as it is backwards, ie it is temporally symmetric.

In order to actually progress through the surrounding fluid, swimming microorganisms therefore need to change their shape in a manner that indicates a clear direction of time. The prototypical example of such a motion is that of a travelling wave [25]. Comprehensive texts on microorganism locomotion in the low Reynolds number regime include concise works by Childress (1981) [23] and Lighthill (1975,1976) [9, 26], a beginners guide to undulatory locomotion by Cohen and Boyle (2010) [27], and a review of principles by Lauga and Powers (2009) [28]. Childress (1981) includes a detailed explanation of the equivalence of rate of working and viscous dissipation, which is discussed later in this chapter. Lighthill (1975, 1976) includes a derivation of the normal and tangental resistance coefficients experienced by the microswimmer (the ratio of which is termed the 'drag anisotropy'), as well as his famous saw-tooth result. Beyond theoretical

foundations and key concepts, the review by Cohen and Boyle (2010) includes simulation tools and also extends to considering non-Newtonian media, considering not only flagella but also microscopic worms (nematodes).

Modelling microscale undulatory locomotion

A popular framework for modelling microscale undulatory locomotion is slender body theory, which was formulated throughout the 1950s [13, 14], and significantly developed further some decades later by contributions including Keller and Rubinow (1976) [29], Lighthill (1976) [26], and Johnson (1980) [30]. The theory reduces the Navier–Stokes equations for the specific case of long, thin cylinders, (ie high aspect ratio) in order to model the flow of the fluid surrounding the body. That is, for a cylinder of length L and radius a, the ratio $a/L = \epsilon \ll 1$. The respective derivations of the theory [26, 29, 30] are all based on matched asymptotic expansions, and although formulated slightly differently, are high related.

The problem of solving Navier–Stokes for high aspect ratio cylinders is reduced from describing a two dimensional surface (ie the structures body) to simply describing a curve. For a long, thin cylinder of length L with arclength $s \in [0, L]$ (ie distance along the length of the body), with curve of the centreline given by $Y(s)$, the result of slender body theory is that there exists a collection of point forces along the curve in the fluid [26, 30]. Then, the velocity at a point along the centreline is given by

$$\boldsymbol{u}(Y(s)) = \mathcal{L}[\boldsymbol{f}](Y(s)) + \mathcal{K}[\boldsymbol{f}](Y(s))$$

where $\boldsymbol{f}$ is the force per unit length, $\mathcal{L}$ is the local force operator (capturing the fluid-body interactions at s), and $\mathcal{K}$ is the nonlocal force operator (accounting for long-range interactions away from the point). Fundamentally, we see that the point-velocity is simply only related to the force at that point.

A widely used simplification of slender body theory is the resistive force theory of Gray and Hancock (1955) [8], which assumes that the hydrodynamic forces are proportional to only the local body velocity. That is, the nonlocal force operator $\mathcal{K}$ is disregarded. Under this assumption, the force acting on the fluid by the undulating body scales linearly with the velocity in the tangential and normal directions:

$$\boldsymbol{f}_T = K_T \boldsymbol{u}_T, \quad \boldsymbol{f}_N = K_N \boldsymbol{u}_N, \tag{2.10}$$

where K_T, K_N are respectively, the resistance coefficients in the tangential and normal to the body centreline directions. The ratio of these coefficients $r_k = K_T/K_N$ is often termed the 'drag anisotropy'.

By resistive force theory, and uniformly discretising the body along its length, the linear force–velocity relationship can be applied to each point along the body, in order to determine the force per unit length acting on the fluid by the undulatory motion. In the asymptotic limit, the body is now reduced to a one-dimensional curve, as opposed to a two-dimensional surface in the fluid. The underlying assumption of resistive force theory is that the hydrodynamic forces scale linearly with the *local* velocity along the body, with some constant of proportionality (the resistance coefficient) [31].

This assumption (ie the omission of nonlocal forces), as pointed out by Lighthill (1976), may be inconsistent with the true hydrodynamic situation in which viscous effects dominate and can produce long-range interactions [26]. For the case of a swimming flagellum, the flow field actually experienced by a moving point along its length will also be influenced by: i) the movement of the other points along the flagellum, especially by the proximity of the ends ($s = 0$ and L), and ii) by the presence, position and movement of a cell body attached to one end of the flagellum [31]. Slender body theory can model the hydrodynamic interactions between nearby points along the flagellum, provided the curvature is not too large. This means that points far away in space are also far apart on the flag-

ellum. As established by Johnson and Brokaw (1979), resistive force theory is a satisfactory approach when the beating pattern of the undulatory planar wave is large amplitude, and also when there is no cell body present (ie the long slender body encapsulates the organism in its entirety, as is the case for nematodes) [31].

Swimming drag anisotropy

Lighthill (1976) [26] derived in the context of zero-thrust (free, unaccelerated swimming) flagellar undulations that the tangential and normal resistance coefficients can be expressed as

$$K_T = \frac{2\pi\mu}{\ln(2q/a)}, \qquad K_N = \frac{4\pi\mu}{\ln(2q/a)+\frac{1}{2}}, \tag{2.11}$$

and their ratio

$$r_k = \frac{K_T}{K_N} = \frac{1}{2} + \frac{1}{4}(\ln(2q/a))^{-1} \tag{2.12}$$

for a the flagellar radius, and $q = 0.09\Lambda$ a small fraction of the flagellar wavelength (where Λ is the wavelength measured along the flagellum). In particular, setting q to this value accurately captures the resistance coefficients and drag anisotropy for undulations of arbitrary wave amplitude. An assumption of this derivation is that q is also a large multiple of the radius a, and it is clear that $\lim_{2q/a\to\infty} r_k = 1/2$.

For low Reynolds number undulatory swimming, it is generally approximated that $r_k = 1/2$ [23]. This approximation is made based on the context of the result which was derived by Lighthill in the limit of infinitessimal radius ($a \to 0$) or infinite length ($L \to \infty$). To provide a concrete example, consider a swimming nematode of length 1mm and width 80μm, ie aspect ratio $a/L = 0.04$. Assuming a wavelength of $\Lambda \approx 1.5$, which is approximately the typical observation for nematodes swimming in water and fluids of similar viscosity [32, 33], then $r_k \approx 1/2 + (1/4)\ln(27/4)^{-1} \approx 0.6$. The value of r_k approaches $1/2$ for greater Λ,

and strictly speaking cannot subceed this value in Newtonian fluids. However, *C. elegans* and other nematodes are often studied crawling across agar surfaces and in other higher-viscosity environments.

To this point, although the development of the theory pertains to microscopic undulatory swimming flagella in viscous fluids, resistive force theory has in fact been shown to provide an effective empirical framework for modelling crawling microscopic undulators, eg nematodes on the surface of agar. This environment is not only higher viscosity, but also has higher ratios of normal to tangential resistivity. This makes the medium non-Newtonian, and such environments may hold elastic properties or may be governed by some nonlinear stress-strain relationship. An experimentally determined value of r_k can be used in such models. Rabets *et al* (2014) [34] directly measured drag forces experienced by crawling *C. elegans* with a micro-cantilever based measurement technique, for a range of different substrate viscoelasticities (1.0% agar to 6.0% agar). Drag forces were found to increase for gels with higher agar concentration, as well as with worm crawling speeds. For high worm speeds (between 500–1000 μm/s), across all agar concentrations the drag anisotropy $r_k \approx 1.4^{-1}$, which is close to the value of 1.5^{-1} suggested by Gray and Lissman [15]. For lower speeds, the drag anisotropy ceases to scale linearly with worm velocity, and measurements across different substrate viscoelasticities were found to range from approximately 1/2 to 1/10. An overall representative measure determined by Rabets *et al* (based on typical worm speeds measured across different substrate viscoelasticities) is $r_k = 1/7$. This is one of the values used by Keaveny and Brown (2017) [35] for predicting the paths of *C. elegans* from sequences of undulations and body postures. Empirical resistive force theory for undulatory crawling of *C. elegans* is discussed in more detail in section 4.2.1, but by example we see that the value $r_k = 1/7$ can be used in empirical resistive force models of microscopic undulatory crawling. This value is used later in this chapter (section 2.5) when determining the optimal straight path undulatory gaits, to compare optimised shapes for swimming

undulators versus crawling, and to study differences between results for these two different scenarios.

2.2.3 Optimality and efficiency

It is natural to consider the optimality of a given locomotion strategy for an undulatory organism, since efficient motion is intrinsic to survival. In particular, low Reynolds number undulatory organisms are a popular choice for studying optimal locomotion. Their microscopic size, living in a world of high viscosity and negligible inertia, simplifies physical analysis as outlined above. Furthermore, their anatomical simplicity, and elegant sinusoidal movement patterns inherently lend themselves to mathematical analysis.

Due to linearity of the Stokes equations, undulatory organism locomotion in Stokes flow will scale linearly with wave frequency (if you undulate twice as fast you will simply get from A to B in half the time). Therefore, quantitative measures of hydrodynamic efficiency need to be normalised such that the optimal undulatory gait is frequency-independent [9].

Rate of mechanical work

To determine the most efficient or optimal swimming undulatory motion at low Reynolds number, we can seek the motion that achieves a maximum swimming speed U for a minimum rate of working. At a given time t, for any object with surface boundary $S(t)$ moving through a fluid, the rate of working on the fluid surrounding the object, denoted by $W_S(t)$, is obtained by integrating the scalar product of the velocity with the force acting on the fluid over the surface [23]:

$$W_S(t) = -\int \boldsymbol{u} \cdot \boldsymbol{\sigma} \cdot \boldsymbol{n} \, \mathrm{d}S. \tag{2.13}$$

where recall $\boldsymbol{u}$, $\boldsymbol{\sigma}$ are the fluid velocity and stress tensor respectively, and $\boldsymbol{n}$ is the outward normal from S. An in-depth derivation is provided by Childress (1981) [23], but to summarise, in relation to the first law of thermodynamics (the law of conservation of energy, colloquially known as "energy can neither be created nor destroyed"), under the relevant assumptions pertaining to swimming microorganisms, this rate of working W_S can be expressed as

$$W_S = \frac{\mathrm{d}E}{\mathrm{d}t} + \tilde{\Phi}(t) \tag{2.14}$$

where $\mathrm{d}E/\mathrm{d}t$ is the rate of change of kinetic energy $E(t)$ between the surface of the organism and the fluid boundary, and $\tilde{\Phi}$ is the rate of heat output due to viscous dissipation. Explicitly, eq. (2.14) directly expresses the first law of thermodynamics: rate of working = change in energy + rate of heat output. The mean (time-averaged, denoted by angular brackets) work done by the organism on the surrounding fluid is obtained by

$$\langle W_S \rangle = \lim_{T^* \to \infty} \frac{1}{T^*} \int_0^{T^*} W_S \, \mathrm{d}t \tag{2.15}$$

and given that $\langle \mathrm{d}E/\mathrm{d}t \rangle = 0$, since

$$\left\langle \frac{\mathrm{d}E}{\mathrm{d}t} \right\rangle = \lim_{T^* \to \infty} \frac{1}{T^*} \int_0^{T^*} \frac{\mathrm{d}}{\mathrm{d}t} E(t) \, \mathrm{d}t = \lim_{T^* \to \infty} \frac{1}{T^*} (E(T^*) - E(0)) = 0 \tag{2.16}$$

it results that the mean work done is in fact equivalent to the time-averaged heat generated due to viscous dissipation:

$$\langle W_S \rangle = \left\langle \tilde{\Phi} \right\rangle. \tag{2.17}$$

Hydrodynamic efficiency

Lighthill (1975) [9] studied the problem of minimising the rate of working (denoted by W_S) for a given swimming speed U for a headless flagellum of length L

by maximising the hydrodynamic efficiency of the undulatory locomotion given by

$$\eta = \frac{K_T L U^2}{W_S}, \tag{2.18}$$

which is arrived at by non-dimensionalising the ratio of the animal's rate of working at the swimming speed U to the rate of working required by an external force to drag the animal through the water at speed U with its flagellum stretched out straight behind it.

Lighthill's sawtooth

The optimal gait (ie planar undulatory motion) that maximises η is determined by Lighthill to be a shape that has constant angle to the body centreline (up to sign $\pm$) almost everywhere. Specifically, the optimal gait is the shape where the cosine of the tangent angle along the length of the body, denoted by ψ (see fig. 2.2), is constant almost everywhere. Furthermore, the value of this maximum efficiency for this optimal motion is determined to be

$$\eta_{\max} = (1 - {r_k}^{1/2})^2 \tag{2.19}$$

which interestingly depends critically on the value of the drag anisotropy. The optimal value of ψ, which also fundamentally depends on r_k, is given by

$$\psi^* = \tan^{-1}(r_k^{1/4}). \tag{2.20}$$

This optimal angle does not vary drastically for different values of r_k. For $r_k = 1/2$, $\psi^* \approx 40^\circ$ and $\eta_{\max} \approx 0.0858$. This means that, at this drag anisotropy, the theoretically best undulator (that is, Lighthill's sawtooth) locomotes with a hydrodynamic efficiency of 8.5%. If $\eta = 1$, this would imply one full body length progress per undulation of the body. Hence, in this low Reynolds number Newtonian fluid, Lighthill predicts that the optimal swimmer would need to undulate

approximately 12 times to progress a single body length.

Lighthill's result of optimal undulatory motion of constant tangent angle must necessarily be saw-tooth shaped: the slender body must alternate between diagonal straight segments each making an angle of approximately 40° with the direction of motion, with infinite curvature at the vertices between the segments. Obviously, this saw-tooth shape is not physically possible in reality, as organisms cannot attain such sharp shapes with points of infinite curvature. Nevertheless, this optimal saw-tooth result is interesting and unintuitive, and the true biological optimum (subject to the individual organisms achievable radius of curvature) is postulated to be a saw-tooth with rounded corners of circular arcs [9]. This gait was in fact observed by Brokaw (1965) [36] for spermatozoa, and by Gray and Lissman (1964) for nematodes [15] (see fig. 2.1).

Generalising efficiency to include bending energy

Eukaryotic flagella have an internal structure (the axoneme) comprised of nine microtubule doublets encircling a central singlet pair, which slide between each other to propagate waves along the length [23, 37]. *C. elegans*' internal digestive and reproductive systems are surrounded by its neuromuscular system, hypodermis, and cuticle [38]. In addition to energetic cost due to dissipation in the surrounding fluid, it also costs energy to bend the body, which needs to be accounted for in the objective of efficiency. We can account for this by applying results from classical beam theory (also known as Euler–Bernoulli beam theory). The active, energy-consuming propagation of waves along the length of the body results in a bending movement being produced that balances the external and internal viscous resistance and the elastic properties of the body [39]. By including elastic energy in the evaluation of the cost of moving, we are capturing not only the cost of deforming the environment (the viscous dissipation), but also the metabolic cost of the undulator deforming *itself*, which forms a significant proportion of the

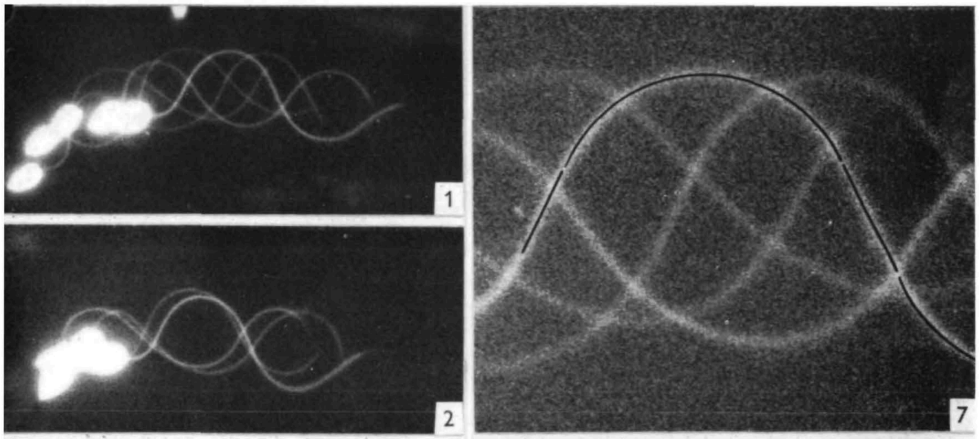

(i) Adapted from Brokaw 1965 [36]. Typical wave patterns of spermatozoa. Successive positions at intervals of 0.02 seconds (flash rate of 50/sec). Images labelled 1 and 2 display spermatozoa of the sea urchin *Lytechinus*. Image labelled 7 is an enlargement of a portion of 1, with circular arcs and straight lines drawn on the image of the flagellum.

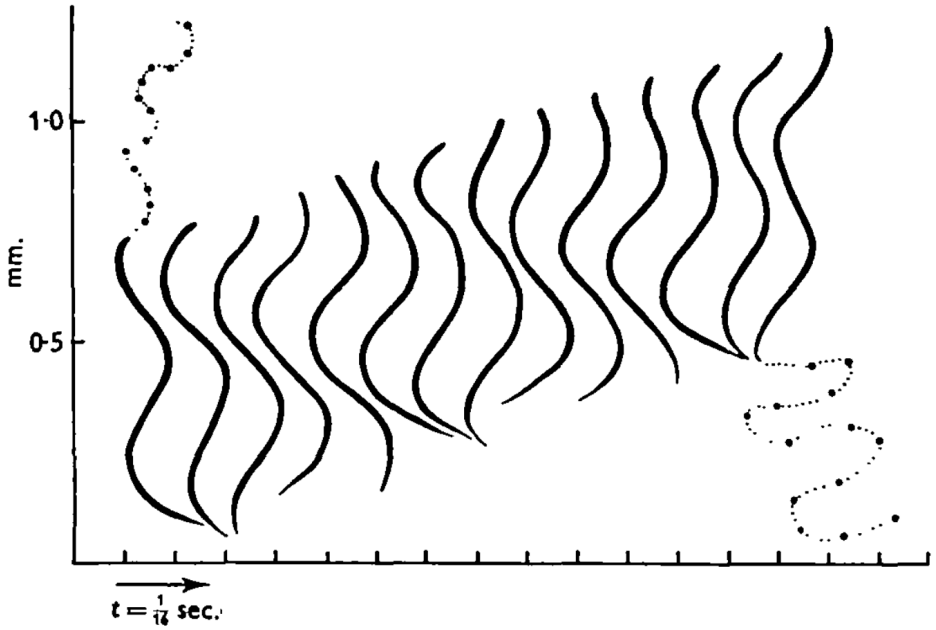

(ii) Adapted from Gray and Lissman 1964 [15]. Successive positions (tracings from successive photographs) at intervals of 0.0625 seconds of a swimming *Turbatrix aceti* nematode.

Figure 2.1: Example images of saw-tooth with rounded corners of circular arcs gait, adapted from the literature.

cost of moving for the organism.

The elastic energy stored in the bending of the body $\tilde{\mathcal{E}}(t)$, by classical elastic beam theory [20], is a function of the effective Young's modulus E, its second moment

of area I, and local curvature $\kappa(s,t)$:

$$\tilde{\mathcal{E}}(t) = \frac{1}{2}EI\int_0^L \kappa^2(s,t)\,\mathrm{d}s\,, \tag{2.21}$$

and represents the potential energy due to the internal forces. The Young's modulus E describes the body's tendency to deform along its axis when force is applied, and the second moment of area I geometrically describes the distribution of points with respect to the body axis. Their product EI (the flexural rigidity, which describes the resistance offered by the body whilst undergoing bending) for spermatozoa flagella has been determined to be $EI \approx 2\times10^{-22}\mathrm{N\ m^2}$ [40,41], yielding an elastic energy stored of $\tilde{\mathcal{E}} \approx 3.6\times10^{-16}\mathrm{N\ m}$ for typical curvatures [12]. Relative to the rate of working, the time-averaged viscous dissipation for spermatozoa has been found to be $\Phi \approx 3.5\times10^{-13}\mathrm{N\ m/s}$ [12]. Hence, the elastic energy is of the same order as the rate of working for 10^{-3}s (approximately 1/30th of a flagellum beat). The (non-dimensionalised) time-averaged elastic energy stored in the flagellum per unit period of the propagated wave describes the energy cost per time:

$$\mathcal{P}_{\text{Bending}} = \gamma_B \left\langle \tilde{\mathcal{E}}(t) \right\rangle \tag{2.22}$$

with $\gamma_B = EI/2$. Employing this, Spagnolie and Lauga (2010) [12], in studying the optimal elastic flagellum, introduce and use a generalised swimming efficiency:

$$\eta = \frac{r_k U^2}{(1-A_B)\Phi + A_B\mathcal{P}_{\text{Bending}}} \tag{2.23}$$

where $\Phi = \left\langle \tilde{\Phi} \right\rangle$ is the time-averaged rate of mechanical work (equivalently, time-averaged viscous dissipation), $\mathcal{P}_{\text{Bending}}$ is the time-averaged elastic energy stored in the flagellum, and $A_B \in [0,1]$ is a dimensionless parameter (set prior to optimisation) allowing for the control of relative importance of mechanical work versus bending in the objective function of efficiency. In including the energy stored elastically in the bending of the body, this approach recovers Lighthill's saw-tooth waveform when $A_B \ll 1$, as well as shapes that optimise the efficiency for vari-

ous importances of bending energy costs. As bending becomes more costly, the optimal solution becomes decreasingly saw-tooth in shape, and more like those postulated by Ligthill: straight segments with rounded corners of circular arcs.

2.3 Model

Determining the optimal undulatory gait

To answer the question of optimal locomotion strategy for a low Reynolds number undulator, an optimisation problem must be solved. Explicitly, the optimisation procedure must compute the shape which maximises the defined efficiency, subject to relevant constraints. The optimisation problem can be solved by decomposing the undulatory shape onto a finite number of modes n^* which describe the time-dependent tangent angle along the body length, for example:

$$\psi(s,t) = \sum_{n=1}^{n^*} \alpha_n f(2\pi n k(s-t)) \tag{2.24}$$

where f is some function of the travelling wave described by the coefficients α_n, k is the wavenumber (how many times along the bodylength the wave is repeated), and the values of α_n for $n = 1, ..., n^*$ are to be determined by the optimisation. When the tangent angle is prescribed, the shape and velocity of the undulator are recovered by integration and differentiation. In the following section we lay out the model framework, kinematics, objective function and constraints of this optimisation problem, in order to determine the optimal undulatory gait.

A schematic summarising our model framework is shown in fig. 2.2. Working with a mechanical and hydrodynamical model, we consider a slender inextensible body along which planar waves propagate down the length, resulting in a net movement in the opposite direction. We consider the problem of prescribing the undulatory movement via a time-dependent tangent angle along the body length,

which we denote by $\psi(s,t)$. We revisit the results established by Spagnolie and Lauga (2010) [12], using independently developed code to both qualitatively and quantitatively reproduce the results. We also explore what happens when the drag anisotropy changes, investigating how the optimal gait changes for a higher friction environment.

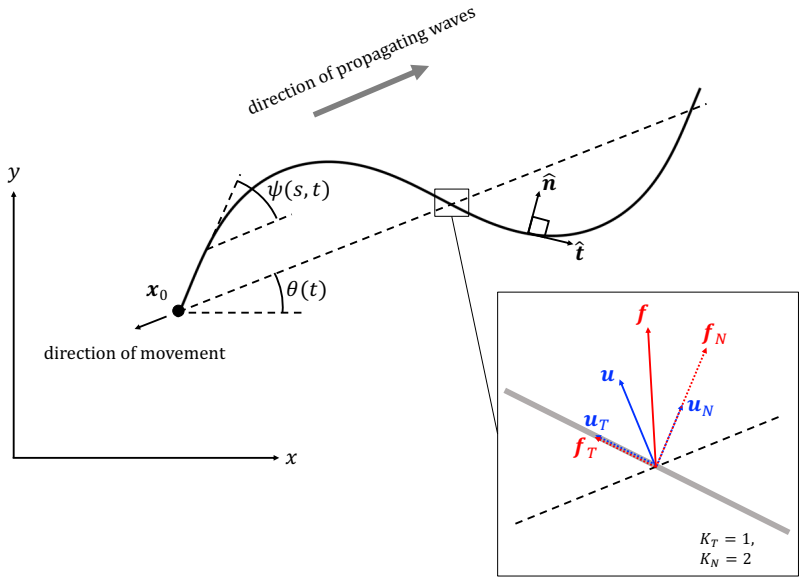

Figure 2.2: Reproduced from Spagnolie and Lauga (2010) [12]. A schematic summarising the kinematic and resistive force model framework. In the x–y plane, a wave of bending deformation is propagated from the head $\boldsymbol{x}_0$ down along the length of the body, resulting in a net movement in the opposite direction. The shape of the wave is prescribed via the tangent angle $\psi(s,t)$. At time t, the wave passes along the length of the body at an angle $\theta(t)$ to the x-axis. By resistive force theory, the velocity of the body $\boldsymbol{u}(s,t)$ is separated into tangential and normal components, as is the corresponding force per unit length $\boldsymbol{f}(s,t)$. To illustrate this in this diagram, the tangential and normal resistance coefficients are respectively $K_T = 1$ and $K_N = 2$.

2.3.1 Kinematics

For an undulator of length L confined to movement in the x–y plane, the position of the body centreline as a function of arclength $s \in [0, L]$ at time t is

$$\boldsymbol{x}(s,t) = \begin{bmatrix} x(s,t) \\ y(s,t) \end{bmatrix} = \boldsymbol{x}_0(t) + \boldsymbol{R}\boldsymbol{r}(s,t) \tag{2.25}$$

where $\boldsymbol{x}_0(t) = \boldsymbol{x}(s=0,t)$ is the position of the head, $\boldsymbol{r}(s,t)$ is the position vector in the body frame, and the rotation matrix

$$\boldsymbol{R} = \begin{bmatrix} \cos\theta(t) & -\sin\theta(t) \\ \sin\theta(t) & \cos\theta(t) \end{bmatrix},$$

with $\theta(t)$ being the angle the body centreline is to the x-axis (see fig. 2.2). The unit tangent vector along the body (in the direction of increasing s) is given by

$$\hat{\boldsymbol{t}} = \frac{\partial \boldsymbol{x}}{\partial s} = \boldsymbol{R}\frac{\partial \boldsymbol{r}}{\partial s}, \tag{2.26}$$

and the velocity of each point is

$$\boldsymbol{u} = \frac{\partial \boldsymbol{x}}{\partial t} = \dot{\boldsymbol{x}}_0(t) + \dot{\theta}(t)\frac{\mathrm{d}\boldsymbol{R}}{\mathrm{d}\theta}\boldsymbol{r}(s,t) + \boldsymbol{R}\frac{\partial \boldsymbol{r}}{\partial t} \tag{2.27}$$

where the dot represents differentiation with respect to time.

We consider the problem of prescribing the tangent angle at each point along the length of the body over time $\psi(s,t)$ in order to determine the optimal gait. When $\psi(s,t)$ is prescribed, the position and velocity are recovered by integration:

$$\hat{\boldsymbol{t}} = \boldsymbol{R}\begin{bmatrix} \cos(\psi(s,t)) \\ \sin(\psi(s,t)) \end{bmatrix}, \tag{2.28}$$

$$\boldsymbol{r}(s,t) = \begin{bmatrix} \int_0^s \cos(\psi(s',t))\,\mathrm{d}s' \\ \int_0^s \sin(\psi(s',t))\,\mathrm{d}s' \end{bmatrix}, \tag{2.29}$$

$$\frac{\partial \boldsymbol{r}}{\partial t} = \begin{bmatrix} \int_0^s -\sin(\psi(s',t))\frac{\partial \psi}{\partial t}\mathrm{d}s' \\ \int_0^s \cos(\psi(s',t))\frac{\partial \psi}{\partial t}\mathrm{d}s' \end{bmatrix}. \tag{2.30}$$

2.3.2 Resistive force model

Let the unit normal be represented by $\hat{\boldsymbol{n}} = \hat{\boldsymbol{t}}^{\perp}$, and K_N, K_T be respectively the normal and tangential resistance coefficients. Defining $\boldsymbol{u}_T$ and $\boldsymbol{u}_N$ as the tangential and normal components of the velocity respectively (see fig. 2.2), we have

$$\boldsymbol{u}_T = (\hat{\boldsymbol{t}} \cdot \boldsymbol{u})\hat{\boldsymbol{t}}\,, \quad \boldsymbol{u}_N = (\hat{\boldsymbol{n}} \cdot \boldsymbol{u})\hat{\boldsymbol{n}}, \tag{2.31}$$

and hence

$$\boldsymbol{u} = \boldsymbol{u}_T + \boldsymbol{u}_N. \tag{2.32}$$

From resistive force theory, the force per unit length (on the fluid) depends linearly on the velocity and with the respective directional resistance coefficients:

$$\hat{\boldsymbol{t}} \cdot \boldsymbol{f}(s,t) = K_T \hat{\boldsymbol{t}} \cdot \boldsymbol{u}, \qquad \hat{\boldsymbol{n}} \cdot \boldsymbol{f}(s,t) = K_N \hat{\boldsymbol{n}} \cdot \boldsymbol{u}. \tag{2.33}$$

This is the fundamental assumption of resistive force theory. Similarly to the velocity, we denote $\boldsymbol{f}_T$ and $\boldsymbol{f}_N$ as the tangential and normal components of the force respectively:

$$\boldsymbol{f}_T = (\hat{\boldsymbol{t}} \cdot \boldsymbol{f})\hat{\boldsymbol{t}}\,, \quad \boldsymbol{f}_N = (\hat{\boldsymbol{n}} \cdot \boldsymbol{f})\hat{\boldsymbol{n}} \tag{2.34}$$

and

$$\boldsymbol{f} = \boldsymbol{f}_T + \boldsymbol{f}_N. \tag{2.35}$$

Hence, by eq. (2.33),

$$\boldsymbol{f} = K_T(\hat{\boldsymbol{t}} \cdot \boldsymbol{u})\hat{\boldsymbol{t}} + K_N(\hat{\boldsymbol{n}} \cdot \boldsymbol{u})\hat{\boldsymbol{n}} \tag{2.36}$$

$$= K_T(\hat{\boldsymbol{t}} \cdot \boldsymbol{u})\hat{\boldsymbol{t}} + K_N(\boldsymbol{u} - (\hat{\boldsymbol{t}} \cdot \boldsymbol{u})\hat{\boldsymbol{t}}). \tag{2.37}$$

Thus the force acting on the fluid per unit length of the body is

$$\boldsymbol{f} = (K_T - K_N)\,\hat{\boldsymbol{t}}\,(\hat{\boldsymbol{t}} \cdot \boldsymbol{u}) + K_N\,\boldsymbol{u}. \tag{2.38}$$

In the absence of inertia, the translation and rotation of the body are obtained by imposing conditions of zero net force and zero net torque:

$$\int_0^L \boldsymbol{f}(s,t)\,\mathrm{d}s = \boldsymbol{0}, \tag{2.39}$$

$$\int_0^L [\boldsymbol{x}(s,t) - \boldsymbol{x}_0(t)] \times \boldsymbol{f}(s,t)\,\mathrm{d}s = \boldsymbol{0}. \tag{2.40}$$

These conditions are linear in the velocities $\dot{x}_0, \dot{y}_0, \dot{\theta}$, and thus can be solved by inverting a 3×3 linear system (derivation in appendix section A.1). This linear system is solved at each $t \in (0, T)$ given the shape of the body at that time $\boldsymbol{x}(s,t)$, in order to calculate the velocity of the body at that time $\boldsymbol{u}(s,t)$. Thus, the geometry of the body at each instant is what enables the unique determination of the velocities $\dot{x}_0, \dot{y}_0, \dot{\theta}$ at each instant.

2.3.3 Determining the optimal gait

To determine the optimal gait for our swimming micro-undulator, we need to determine the ratio of mechanical cost incurred for an achieved swimming speed. Our cost considers both rate of mechanical work due to viscous dissipation, and also bending cost due to deformation of the body.

Energetic cost due to dissipation

In order to determine the energetic cost of the undulatory movement, we consider the work done on the surrounding fluid by the swimmer. The rate of work on the surrounding fluid by the undulator is obtained by integrating the scalar product of velocity and the force per unit length along the body:

$$\tilde{\Phi}(t) = \int_0^L \boldsymbol{f}(s,t) \cdot \boldsymbol{u}(s,t)\,\mathrm{d}s. \tag{2.41}$$

In our optimisation, we consider the time-averaged rate of mechanical work (equivalently, the viscous dissipation), given by

$$\Phi = \left\langle \tilde{\Phi}(t) \right\rangle \tag{2.42}$$

where angular brackets denote period-averaging:

$$\left\langle \tilde{\Phi}(t) \right\rangle = \frac{1}{T} \int_0^T \tilde{\Phi}(t)\,\mathrm{d}t \tag{2.43}$$

where $T = 1/k$ is the fundamental period of the waveform, for wavenumber k. To perform period-averaging, the time-average of a quantity $Q(t)$ is given by

$$\langle Q(t) \rangle = \frac{1}{T} \int_0^T Q(t)\,\mathrm{d}t \approx k\,\Delta t \sum_{n=0}^{N_t-1} Q(t_n) \tag{2.44}$$

where $t_0 = 0$ and $t_{N_t-1} = T - \Delta t$.

Energetic cost due to bending deformation

The work required for bending deformations is included by explicitly taking into account the elastic nature of the body, considering the bending energy of an inextensible elastic rod in a viscous fluid [12, 20, 42]. The (non-dimensionalised) time-averaged elastic bending energy stored internally in the body $\mathcal{P}_{\text{Bending}}$ is cal-

culated by integrating the square of the curvature along the length of the body:

$$\mathcal{P}_{\text{Bending}} = \left\langle \int_0^L \kappa(s,t)^2 \, \mathrm{d}s \right\rangle \tag{2.45}$$

where

$$\kappa(s,t) = \frac{\partial \psi}{\partial s} \tag{2.46}$$

denotes the curvature.

Efficiency

A widely-used measure of hydrodynamic efficiency for undulatory gaits in the low Reynolds number regime is given by

$$\eta_H = \frac{r_k U^2}{\Phi} \tag{2.47}$$

where $r_k = K_T/K_N$, and U is a measure of mean undulatory speed of the body, which we determine by calculating

$$\begin{aligned} U &= |\,\langle \dot{\boldsymbol{x}}_0 \rangle\,| \\ &= (\langle \dot{x}_0 \rangle^2 + \langle \dot{y}_0 \rangle^2)^{1/2}. \end{aligned} \tag{2.48}$$

This quantity for the efficiency arises from considering the ratio of the rate of mechanical work required to drag the swimmer with a frozen shape though the fluid at speed U to the average rate of work done by the swimmer [28].

A generalised measure of efficiency which incorporates bending cost (from Spagnolie and Lauga [12]) is given by

$$\eta = \frac{r_k U^2}{(1-A_B)\Phi + A_B \mathcal{P}_{\text{Bending}}}, \tag{2.49}$$

where A_B is a dimensionless parameter fixed prior to optimisation that takes a

value between 0 and 1, which controls the relative importance of the rate of mechanical work Φ versus the bending cost $\mathcal{P}_{\text{Bending}}$. As A_B increases from 0 towards 1, curvature in the waveform is penalised increasingly, and incurs a greater cost.

2.4 Numerical methods and optimisation

Time is discretised into N_t equal time steps over $t \in [0, T]$ where $T = 1/k$ (k the wavenumber), the period of motion, is the fundamental period of the waveform. Space is discretised into N_s uniformly distributed points on the domain $s \in [0, L]$, where L is the length of the body.

The optimisation problem posed is to determine the optimal undulatory gait which maximises the efficiency (the objective function), subject to necessary constraints. As mentioned prior, determining the optimal gait is achieved by decomposing the shape of the body onto a finite number of modes which describe the time-dependent tangent angle $\psi(s,t)$. For this chapter, the expression for the tangent angle (as in Spagnolie and Lauga (2010) [12]) is given by:

$$\psi(s,t) = \sum_{n=1}^{n^*} a_n \cos(2\pi nk(s-t)) + b_n \sin(2\pi nk(s-t)) \tag{2.50}$$

which is a finite sum over n^* Fourier modes, yielding a linear combination of functions which prescribe a travelling wave. The Fourier modes a_n, b_n are the control parameters which are to be determined by the numerical optimisation routine, such that the efficiency is maximised. The wavenumber k is, in this chapter, also included as a control parameter to be determined by the optimisation.

Numerical optimisation is performed using a sequential quadratic programming (SQP) method in the MATLAB optimisation toolbox. For an initial undulatory shape prescribed by the parameters a_n, b_n, k, given the tangent angle $\psi(s,t)$ the body kinematics are determined by integration, and the body motion is uniquely

determined at each time step by solving the 3 by 3 linear system of the velocities (eqs. (2.38) to (2.40), the terms in this system are provided in appendix section A.1). Following calculation of the velocity at each time step, the force, rate of mechanical work, and bending cost are all calculated as outlined by the model framework (section 2.3). Hence, the efficiency is determined by evaluating eq. (2.49).

At each iteration in the optimisation routine, the control parameters a_n, b_n, k which prescribe the shape of the body are modified in order to maximise the gait efficiency η, until the change in the value of the objective function is within a certain tolerance (which we set to be 10^{-14}). This tolerance level follows that of previous studies [12], and at higher tolerances the results are indistinguishable.

The problem is intrinsically constrained by the fact that the velocity is determined by the resistive force theory, requiring zero net force and zero net torque. In accordance with Spagnolie and Lauga (2010), an extrinsic constraint is imposed in the optimisation problem, requiring that the body rotation remains the same over the total period of the wave:

$$\theta(0) = \theta(T). \tag{2.51}$$

This constraint is necessary numerically in the case of maximising efficiency for straight-path locomotion as it ensures that the body does not rotate in circles over many periods. Without this constraint, the undulator does not actually only move along a straight line. It is implemented in the numerical optimisation routine (MATLAB's `fmincon` which optimises a constrained nonlinear multivariable function) in the nonlinear equality constraints argument. The constraints in the optimisation routine are also satisfied to within a certain tolerance (again, 10^{-14}).

The parameters that are fixed prior to optimisation are: i) $r_k = K_T/K_N$, the drag anisotropy ratio, and ii) A_B, the relative importance of mechanical work

versus bending cost. To compare the results of swimming versus crawling drag anisotropy, we obtain results for two different values of r_k: $1/2$ and $1/7$. The optimal gaits for different values of A_B were obtained for $A_B = 10^{\delta}$ for $\delta \in \{-7, -6, ..., -1, 0\}$. Seeking to quantitatively replicate results from the literature [12], we take $n^* = 160$, $N_t = 160$, $N_s = 2400$, with $L = 1$.

In this scenario, it is not possible to run the numerical optimisation for the purely hydrodynamic efficiency ($A_B = 0$), as this is a singular case. For a finite length swimmer, you obtain (analytically) the optimal gait as an infinite number of infinitesimally small amplitude waves. This gait is therefore not numerically viable, as one would need an infinite number of modes in order to capture it. This limitation of the numerical framework could be considered problematic, but as we will see the $A_B = 10^{-7}$ in fact recovers Lightill's sawtooth, and the variability of A_B for the generalised swimming efficiency regularises the behaviour of this optimal gait.

2.5 Results for optimal straight-path locomotion

2.5.1 Swimming drag anisotropy

For $r_k = 1/2$, optimal waveforms for a selection of A_B values are shown in fig. 2.3. A plot displaying the results of both hydrodynamic efficiency η_H and generalised swimming efficiency η in this case for all values of A_B is shown in fig. 2.4. For $A_B = 10^{-7}, 10^{-4}, 10^{-2}$ and 1, the resulting optimal waveforms have efficiency $\eta = 0.0858, 0.08, 0.0369$, and 7.86×10^{-4} respectively. These results are not only in agreement with [12] ($\eta = 0.0858, \sim 0.08, \sim 0.035$, and 7.68×10^{-4}, approximate values obtained from results figures), but the value of η for the smallest value of $A_B = 10^{-7}$ recovers exactly the optimal hydrodynamic efficiency $\eta_{\max}$ derived by Lighthill given the drag anisotropy (eq. (2.19)). Furthermore, as A_B decreases from 1 towards zero, the waveform becomes increasingly saw-tooth, visually re-

covering Lighthill's analytical study which determined this global optimum [9] . This can be seen in fig. 2.5, where the tangent angle ψ as a function of s becomes increasing like alternating between diagonal straight segments with increasingly abrupt change in curvature at the vertices between the segments. Furthermore, as $A_B \to 0$ the angle which those straight segments make with the body centreline approaches Ligthill's analytically determined optimal: $\psi^* = \tan^{-1}(r_k^{1/4}) \approx 40.06°$ for $r_k = 1/2$.

As the bending cost increases from 10^{-7} to 1 the efficiency η of the undulatory locomotion decreases. Both the optimal wavenumber k and the mean swimming speed U also decrease (see fig. 2.8), aligning with results from the literature [12]. For physical swimmers, the value of A_B could be modified from one type of organism to another. To determine A_B in a context-specific manner, this value will depend on the ratio of flexural rigidity and viscosity. That is, it should appropriately balance the ratio of bending cost to viscous dissipation. For highly flexible organisms intuitively one would have a lower A_B than for more rigid organisms. For example, A_B for spermatozoa would be expected to be smaller than for a nematode. Typically observed efficiencies of biological swimming cells are frequently found to be approximately 1%, suggesting that A_B could be between 10^{-1} and 10^{-2} for this case (as $\eta = 0.007$ and 0.037 respectively for these values). However, it could also (and likely) be that real biological cells do not move completely efficiently, and indeed indications that there exists room for further biological tuning have been suggested [12]. A perhaps more appropriate alternative to inferring from observed biological efficiencies is examining estimates of bending costs and viscous dissipation separately, which could yield better determination of A_B in specific contexts. As discussed in section 2.2.3, typical estimates of these quantities for biological swimming cells (flagellates) are found to be around $\tilde{\mathcal{E}} \approx 3.6\times10^{-16}$N m and $\Phi \approx 3.5\times10^{-13}$N m/s. If we assumed that these quantities contribute comparably to the mechanical cost of locomotion, this indicates that $A_B \approx 1 - 10^{-3}$ could be a reasonable estimate, which is notably different from suggestions above.

The precise approach to determining A_B in a context-specific manner remains an open question.

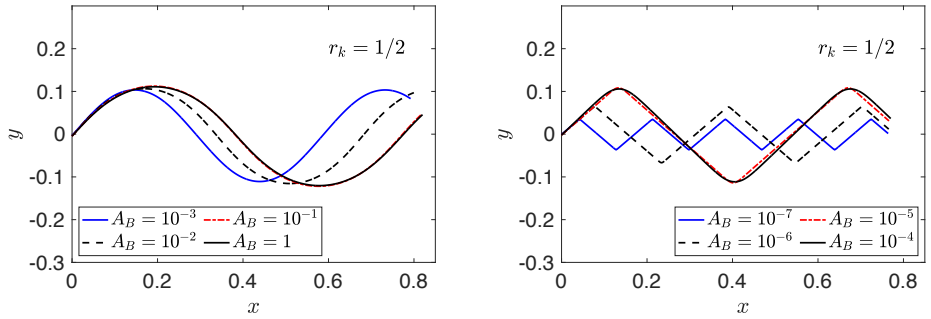

Figure 2.3: Optimal swimming ($r_k = 1/2$) waveforms for a selection of $A_B \in [0, 1]$. As the bending cost increases, the optimal waveforms become decreasingly saw-tooth like, with smaller wavenumber. These optimal waveforms align with those found in [12].

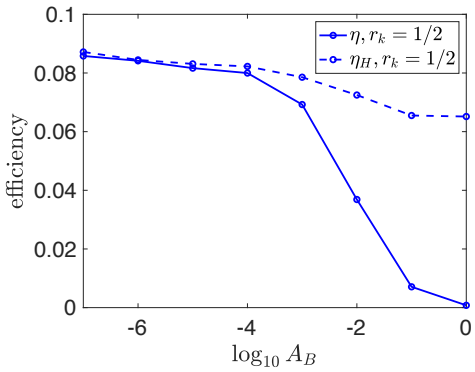

Figure 2.4: Maximum swimming ($r_k = 1/2$) efficiencies for a selection of $A_B \in [0, 1]$.

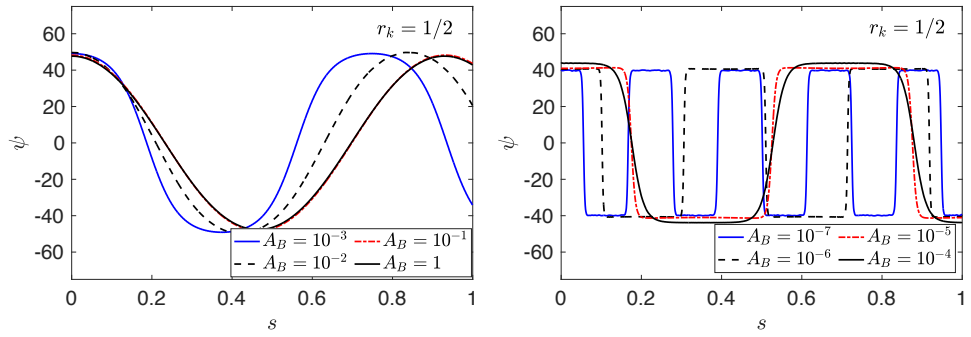

Figure 2.5: The tangent angle ψ as a function of s along the length of the undulator, for values of $A_B \in [10^{-7}, 1]$. As $A_B \to 0$, ψ becomes increasingly like diagonal straight segments of alternating sign, and the angle which those segments make with the body centreline approaches Lighthill's analytically determined $\psi^* \approx 40°$.

2.5.2 Crawling drag anisotropy

For $r_k = 1/7$, optimal waveforms for a range of values for A_B are shown in fig. 2.6. Analogously to the results for $r_k = 1/2$, again the waveforms become increasingly saw-tooth with wavenumber increasing as A_B tends towards zero from 1. Comparing these with results for swimming drag anisotropy, the amplitude of the waveforms is decreased (see fig. 2.7). Furthermore, with the relative increase in normal resistance, the undulator moves with less slip.

For $A_B = 10^{-7}, 10^{-4}, 10^{-2}$ and 1, the efficiency of the optimal waveforms is $\eta = 0.3851, 0.3644, 0.1440$ and 0.0027 respectively. These values are compared with those for $r_k = 1/2$ in fig. 2.8. Interestingly, again referring to Lighthill's derived maximum hydrodynamic efficiency as a function of the drag anisotropy, for $r_k = 1/7$ we have that

$$\eta_{\max} = (1 - (1/7)^{1/2})^2 \approx 0.386 \tag{2.52}$$

which agrees quantitatively very closely for our $A_B = 10^{-7}$ result.

The overall trends are consistent with those for swimming drag anisotropy, with η, k, and U decreasing as A_B tends from zero to 1. The values for the wavenumber k for both cases of r_k are consistent. For efficiency η and speed U, the values are

higher for the crawling drag anisotropy. The reduce in slip results in an optimal waveform with which the undulator moves faster through the space, with lower dissipation, and thus by definition increasing η.

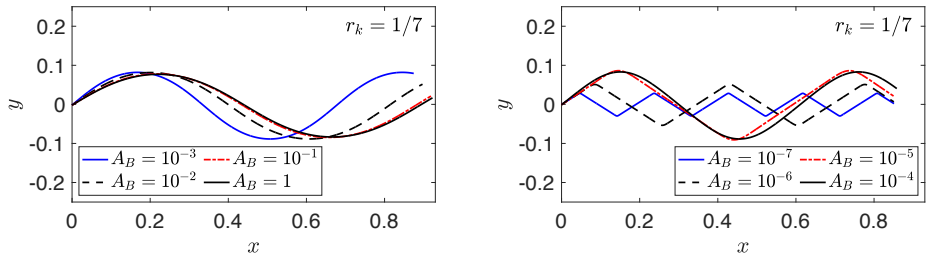

Figure 2.6: Optimal crawling ($r_k = 1/7$) waveforms for some values of $A_B \in [0, 1]$. Analogously to $r_k = 1/2$, decreasing the relative importance of the bending cost results in progressively saw-tooth shapes.

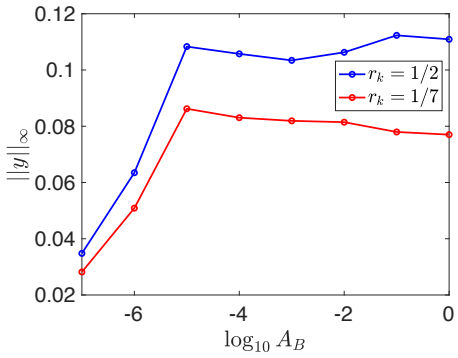

Figure 2.7: Amplitude of optimal waveforms for swimming ($r_k = 1/2$) and crawling ($r_k = 1/7$). The amplitude for crawling drag anisotropy is decreased to compared with swimming.

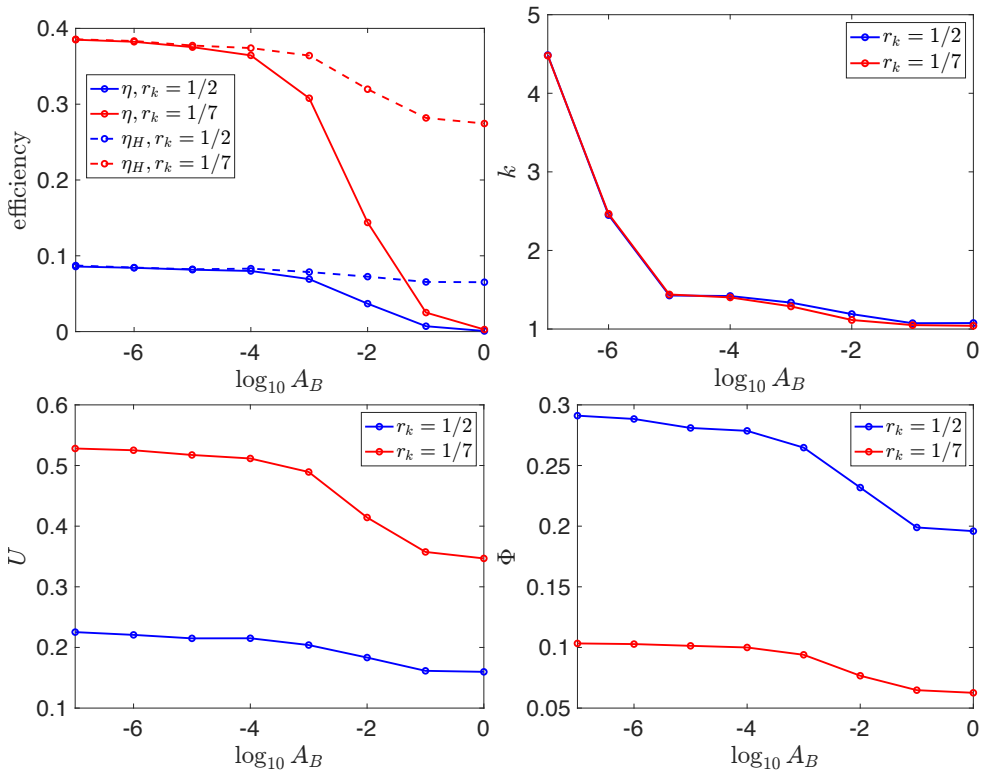

Figure 2.8: Comparison of properties of the optimal waveforms as a function of the bending cost. From top left to bottom right: (i) the efficiency η, (ii) the wavenumber k, (iii) the swimming speed U, (iv) the rate of mechanical work Φ. Trends are maintained and consistent for the cases $r_k = 1/2$ (swimming) and $r_k = 1/7$ (crawling).

2.5.3 Discussion

There is an interesting modulation of the wavenumber across the different values of A_B as it decreases from 1 towards zero. For A_B between 1 and 10^{-4}, the wavenumber k of the optimal waveform increases gradually from 1.08 to 1.42. An interesting transition occurs beyond $A_B = 10^{-4}$, where the optimal wavenumber jumps discontinuously to the next half integer wavenumber (approximately 2.5). This discontinuous jump occurs again beyond $A_B = 10^{-6}$. This observation was also made in [12], where these transitions were found to also result in more locally optimal solutions arising. As emphasised in [12], the bias towards half-integer wavenumbers is an output of the optimisation, and yields hydrodynamic benefits as the half-integer spatial modes limit vertical drift.

This discontinuous jumping in the wavenumber as A_B decreases highlights the qualitative behaviour change from sinusoidal to sawtooth waveforms. In fig. 2.7, for $A_B < 10^{-5}$ the behaviour of the amplitude as a function of A_B changes notably. This is in the sawtooth regime and is a result of a coupled effect. The body is finite length, so the increase in wavenumber results in this decrease in amplitude.

As opposed to this theoretical analysis, in an experimental context in many systems the observed trend is: the lower the viscosity the lower the wavenumber. For example, *C. elegans* swimming gait which occurs in a lower-viscosity environment characteristically has lower wavenumber (approximately 0.5) than its crawling gait which occurs in a higher-viscosity environment (with wavenumber greater than 1) (this is discussed in much more detail in chapter 4). This suggests that the lower the resistivity of the environment, the lower the hydrodynamic cost (since there is less resistance from the environment to being distorted). Hence the fixed bending cost increasingly dominates, suggesting further that A_B is a function of viscosity, and could be higher in such environments.

2.6 Summary

In this chapter we have presented a model framework to determine the optimal undulatory locomotion for a microswimmer in the low Reynolds number regime. For the context of straight-path forwards locomotion, the optimal travelling wave gait which maximises the hydrodynamic efficiency is that of a saw-tooth, derived theoretically by Lighthill (1975) [9] and recovered computationally here. When the generalised swimming efficiency is maximised (Spagnolie and Lauga (2010) [12], increasing the penalty for bending deformation in the body results in increasingly smooth optimal gaits. For both swimming and crawling drag anisotropies tested, Lighthill's maximum hydrodynamic efficiency is recovered for the lowest bending penalty tested.

The majority of research up to this point on optimal microscopic undulatory locomotion has wholly focused on optimal gaits for straight-path forwards locomotion. However, it is not the case that these organisms move exclusively forwards and in straight lines. Indeed, they turn and reverse and reorient themselves in order to navigate their surroundings. In the following chapter we extend the approaches described above, to introduce path curvature, modelling optimal undulatory *turning* for low Reynolds number microswimmers. Addressing this question from a theoretical perspective has the potential to provide us with insight into the biomechanics and behavioural characteristics of different motion modes of undulatory microorganisms.

Chapter 3

Optimal undulatory turning

3.1 Introduction

In the previous chapter we reviewed optimal undulatory locomotion in the context of low Reynolds number hydrodynamics, established a model framework, and recreated results from the literature (Spagnolie and Lauga, 2010 [12]) with independently-developed numerical framework and code for straight-path forwards locomotion. Lighthill's famous saw-tooth is the optimal shape which maximises hydrodynamic efficiency (Lighthill, 1975 [9]). For a generalised measure of efficiency, which accounts for bending energy stored in the body, as the relative importance of bending cost versus viscous dissipation is increased, the optimal shape becomes increasingly smooth with less extreme curvature [12].

The majority of research in this realm up to this point has focused on optimal straight-path forwards locomotion. It is of course not the case that organisms move exclusively forwards and in straight lines. *C. elegans*, for example, employs many types of movement patterns when swimming or crawling to navigate its surroundings. Its well-known omega turn, in which the worm makes a sharp turn forming an Ω-shape, and the reversal, in which the worm draws it-

self backwards, are commonly observed motion modes. These behaviours have been well-characterised for several decades [43–46]. Episodes of turning termed "pirouettes" (Pierce-Shimomura *et al* 1999 [46]) have been shown to mediate chemotaxis and thermotaxis behaviour. Through series of sharp turns (reversals and omega turns) between bouts of forward motion, random reorientations are induced in the absence of gradients (chemical or thermal), and biased random walks arise when a gradient is present [46–49]. Precise quantification of these behaviours (enabled by analysing nematode movement captured in video recordings) has lead to the identification of specific interneurons involved in different modes of *C. elegans* locomotion [50–52]. Further details and a more extensive literature review of *C. elegans* behaviour can be found in chapter 4 of this thesis. In addition to the omega turn, gentler disruptions to the propagating wave are observed in 'shallow turns' (analysed by Kim *et al* (2011) [53]), resulting in a relatively small change in orientation, and maintaining a sinusoidal pattern. The ability to turn and manoeuvre is important to survival.

In the context of robotics, optimal undulatory turning gait was studied by Kohannim and Iwasaki (2012) [54] by considering a mechanical rectifier model describing the the locomotion of a link-chain system. Formulating the optimal control problem, they minimise a quadratic cost function comprised of the control input and joint angles, subject to constraints in the average tangential and rotational velocities. The control input is restricted to the class of sinusoidal signals, with periodic shapes restricted to planar waves. This study extended upon in Kohannim and Iwasaki (2014) [55] and Kohannim and Iwasaki (2017) [56] to investigate optimal turning gaits for mechanical rectifier systems for three dimensional motion. They consider a multi-body system consisting of two rigid bodies connected arbitrarily – a system that can be viewed as a mechanical model for biological motions such as flying birds or swimming batoids (eg stingrays). Though pertaining to the macroscale, these studies provide insight on how parallels to animal locomotion can be drawn from mechanical models, as the dynamics that

convert periodic body movements to a positive average thrust result in a steady locomotion velocity.

Developing a mathematical framework to describe optimal undulatory turning for low Reynolds number organisms is one of the main focuses of this thesis. When investigating optimal micro-undulator locomotion, Lighthill responded to his famous saw-tooth result saying "it is noted that in reality some minimum achievable radius of curvature of bending would prevent this saw-tooth waveform from actualising for an undulatory mover" [9]. This saw-tooth result is surprising and unintuitive, and is indicative of how results from mathematical models cannot be interpreted too literally. Real-world observations are almost inevitably more complicated than empirical models would suggest. Solutions to the problem of optimal undulatory turning could be equally surprising and unintuitive.

In this chapter we expand on and adapt the framework presented previously in chapter 2 for straight-path forwards movement, to investigate optimal undulatory turning gaits in this low Reynolds number hydrodynamical context.

Structure of this chapter

Section 3.1.1 describes how the framework presented in the previous chapter of this thesis is adapted from considering straight path forwards locomotion to instead modelling optimal undulatory turning. Following this, we present an analytical result in section 3.1.1 that demonstrates the importance of curvature constraints in the optimisation problem. Specifically, we find that as the bending cost A_B approaches zero, there exists an optimal radius of curvature R for the optimal gait that minimises the mechanical cost of locomotion. This optimal radius of curvature also tends to zero, and this analytical result is verified numerically.

Following this, we present results for optimal undulatory turns in the low Reynolds number regime. These are defined as the waveform that minimises the mechani-

cal cost of locomotion (our objective function) given that a turn of a certain size is achieved. Results are obtained for several different shape spaces: Fourier travelling waves, Chebyshev waves, and travelling waves of constant curvature. The results from these different parameterisations of the shape space are compared, analysed and discussed.

3.1.1 Adapting the straight-path model

Objective function and rotational constraint

Recall that in chapter 2 the optimal waveform for straight-path forwards locomotion was determined by maximising the efficiency, subject to constraints of zero net force and torque (required by the resistive force model), as well as the rotational constraint that $\theta(T) = \theta(0)$, where $\theta(t)$ is the angle the body centreline is to the x-axis, and $T = 1/k$ the period of the waveform (k is the wavenumber). This constraint ensured that the body does not rotate in circles over many periods.

For the case of determining the optimal turning gait, instead of a measure of efficiency which rewards higher mean speeds or increased net displacement, our objective function to be optimised captures only the mechanical cost of the movement:

$$F = (1 - A_B)\Phi + A_B \mathcal{P}_{\text{Bending}}. \tag{3.1}$$

This ensures there is no requirement for the optimal turn to be performed whilst achieving a maximum swimming speed, or maximum translation — we neither reward nor assume any explicit displacement or mean velocity. The objective function F is the denominator of the generalised swimming efficiency from Spagnolie and Lauga (2010) [12] which was used in the previous chapter, and incorporates both the rate of mechanical work Φ and the elastic energy stored in the bending of the body $\mathcal{P}_{\text{Bending}}$. Again, A_B is a dimensionless parameter that takes a value between 0 and 1, that is fixed prior to optimisation and allows control of the relative

importance of mechanical work versus bending cost in the objective function.

In the previous chapter we sought to maximise the efficiency, whereas in the context of turning we opt to minimise only the mechanical cost of motion so as not to require the undulator to achieve a certain speed or net displacement. It would not make sense to use the same objective function for turning as we did in chapter 2 (where the objective was to maximise the efficiency for the case of straight-path forwards motion), as the question posed in this chapter seeks to determine the optimal in-place reorientation strategy for the undulator.

To obtain the optimal turning gait, we adapt the rotational constraint included in the numerical optimisation routine for straight-path locomotion to require that the body achieves a given turning angle by the time $t = T$:

$$\theta(T) = \theta(0) + \theta^* \tag{3.2}$$

where θ^* is the size of the turn to be performed. Imposing this constraint with $\theta^* \in [-\pi, \pi]$ in the optimisation routine enables the investigation of the optimal turning gaits, and is what allows us to model optimal turning. The parameter θ^* is fixed prior to optimisation, and dictates the angle that the undulator is required to reorientate itself by the end of the fundamental period of the waveform. Here the numerical formulation is separate from the statement of the problem, as it is in chapter 2. Again as in chapter 2, this constraint is imposed via MATLAB's nonlinear constraint function in the optimisation toolbox. Explicitly, we are considering the problem of minimising the mechanical cost of moving for an undulatory microswimmer, subject to the constraint that it achieves a reorientation of size θ^* after one period. No assumption on a given speed or net motion achieved by the undulator is imposed: we do not require the swimmer move from point A to B in space, we simply consider a given reorientation, independent of how fast or how much distance is travelled in the process. The problem posed in this chapter is not a path optimisation, but instead a reorientation optimisation.

The kinematics and resistive force model which describe the fluid–body interactions are identical to that laid out in section 2.3. Again, the optimal gait is determined by decomposing the shape of the body onto a finite number of modes describing the tangent angle $\psi(s,t)$.

The optimal undulatory turn is defined as the waveform which minimises the cost function F over the modes which describe ψ, subject to the resistive force model (section 2.3.2), and also that the orientation of the body after one period be equal to that at the start plus some turning angle θ^*:

$$\begin{aligned} \min_{\psi(s,t)} F \quad \text{subject to:} \quad & \text{eqs. (2.25) to (2.40)}, \\ & \theta(T) = \theta(0) + \theta^*. \end{aligned} \tag{3.3}$$

For straight-path forwards locomotion, the hydrodynamic efficiency is the ratio of the rate of mechanical work required to achieve a given swimming speed to the rate of working required by an external force to drag the undulator through the fluid at that speed with its body stretched out behind it. An alternative way of thinking about hydrodynamic efficiency for straight path forwards locomotion is to consider imposing a constraint on how far the body needs to travel, requiring a fixed displacement, and then minimising the cost associated with locomotion. That is, the problem posed in chapter 2 could be considered as: fixing the swimming speed U, and finding the minimum mechanical cost F such that the efficiency η is maximised.

By that analogy, in this chapter (where we have adapted the objective function to address a related yet separate and alternative question from the previous) we are determining the optimal turning gait by fixing the size of the turn required, and minimising the cost associated with that motion. Hence the turning constraint $\theta(T) = \theta(0) + \theta^*$ is crucial for determining the optimal turn. Minimising the cost function F without imposing this constraint would result in the undulator simply doing nothing, as not moving at all naturally incurs no locomotory cost.

The turning constraint forces the undulator to do something, rather than nothing.

Conceptually, one could devise a measure of hydrodynamic efficiency for the case of turning. By similar analogy as above, it could be possible to consider the ratio of mechanical work required by the undulator to achieve turning angle θ^* to the rate of working required by an external torque to rotate the swimmer by that amount. This ratio would yield a hydrodynamic efficiency for the specific case of turning. Whilst not considered in this thesis, this would provide an alternative objective function for which we could optimise over in order to determine the optimal undulatory turn.

The objective function minimised in the optimisation problem in this chapter captures only the mechanical cost associated with the undulatory turning strategy. The reorientation of the body given by θ^* achieved after one period of the wave does not impose or require any distance travelled across the space. The formulated problem applies to in-place turning (ie imagine a person turning around whilst their feet stay in the same spot), rather that traversing a curved path of a given radius (such as a person walking around the edge of the Colosseum). More precisely, there are no restrictions on motion: the formulation of the problem does allow for translation, and the constraint only specifies that the body must reorient itself. Hence although the body may translate, in one period it won't get very far. This formulation captures the real-animal behaviour of undulators turning to head in a different direction locally: an in-place reorientation whilst not attaining any significant net displacement over one period. For the example of *C. elegans*, the magnitude of the reorientation (how large θ^* is) captures the spectrum of behaviours from shallow turns to omega turns. Large θ^* can be associated with omega turning since the change of direction is prominent. For the commonly observed behaviour of gradual reorientation (eg to move up or down some gradient), a series of small θ^* turns would capture this gait. For example, four $\theta^* = \pi/32$ turns become a turn of $\pi/8$ after four periods. The problem being investigated in this chapter — the (gradual or sizeable) reorientations and consid-

eration of optimal in-place turning strategies — lies within the broader problem of answering the question "what is the most efficient way of getting from point A to B under given circumstances?".

Model parameters

As in chapter 2, some parameters in the model need to be fixed prior to numerical optimisation. We again set the parameter $A_B \in [0,1]$ to control the penalty for bending, and also $r_k = K_T/K_N$ the ratio of tangential to normal resistance, which for swimming micro-undulators is $1/2$. This value is applicable for flagella and organisms such as spermatozoa, but we note here that this ratio is different for micro-undulators such as nematodes (as these are not even approximately infinitely slender). We choose $r_k = 1/2$ in this chapter for consistency with chapter 2. We also set the turning angle θ^* which via the rotational constraint dictates the net path curvature and the size of the turn to be performed.

When optimising for straight-path forwards locomotion, the wavenumber k was included with the modes that describe the tangent angle in the set of control parameters, the values of which are determined by the optimisation routine such that the efficiency is maximised. However, for optimal undulatory turning instead of maximising the efficiency we are minimising the cost. As a result, including the wavenumber as a control parameter results in $k \to 0$. This clearly minimises F, as $T \to \infty$ allowing the undulator infinite time to perform the turn. We therefore fix the value of k prior to optimisation.

The parameters to be fixed prior to numerical optimisation are therefore: i) A_B, the relative importance of mechanical work versus bending, ii) r_k, the drag anisotropy, iii) θ^*, the turning angle, and iv) k, the wavenumber.

Overlapping

For the case of straight-path forwards locomotion, non-self-intersecting optimal shapes are readily found, and it is easy to find optimal shapes where overlapping does not occur. However, for investigating optimal turning gaits, overlapping is potentially unavoidable and it is intuitive to think that for the resulting body postures, it may be optimal to perform the turn by assuming high-curvature shapes that would induce the undulator to cross over itself.

Here we interpret self-intersection as the body crossing over itself, with the undulator coming out of the plane. No additional penalty is incurred for any kind of overlapping by the body. We note that the validity of resistive force theory for the extreme scenario of self-intersection is brought into question, since this framework neglects nonlocal forces which arise (the actual forces experienced by a point along the body length is also influenced by the motion of the other points). Alternative frameworks such as slender body theory could be used to investigate such interactions, at the expense of high computational cost.

3.2 Reducing the radius of curvature

In this section we demonstrate that for the case of optimal undulatory turning, a definitive way to minimise the objective function F is for the undulator to reduce its radius of curvature, and shrink to a tightly-coiled shape.

Here we present an analytical result which shows that for a slender body moving along a circle of radius R, that is propagating a travelling wave of magnitude ϵ, as A_B approaches 0, there exists an optimal value of R such that the cost function F is minimised.

For the purposes of this result, we introduce an alternative basis from the one used previously, whereby analysis and integration is performed with respect to the

origin. This alternative parametrisation simplifies the derivation of the analytical result. This result is also established in the instantaneous case. This allows for and simplifies assumptions (for example, of zero net translation) which yield the result. A schematic summarising this basis is shown in fig. 3.1.

The derivation of this result in the instantaneous scenario enables and simplifies the proceeding analysis. In the optimal control problem, there is a limit to how many unknowns can be solved for. In the optimisation, we need to determine $\boldsymbol{x}(t)$ and $\theta(t)$. Therefore, in the derivation of this analytical result, we take $\dot{\boldsymbol{x}}_0(t) = 0$ (translational velocity is zero), and thus the zero net force constraint disappears. The constraint of zero net torque remains.

3.2.1 Analytical result

The position (ie shape) of the undulator along the arc-length φ at time t is now given by

$$\boldsymbol{x}(\varphi, t) = \boldsymbol{R}(\theta(t))(R[1 + \epsilon f(\varphi - ct)]\hat{\boldsymbol{r}}(\varphi)) \tag{3.4}$$

where $\boldsymbol{R}$ is the rotation matrix, R the radius of curvature, f a travelling wave perturbation to the radius of size ϵ, and

$$\hat{\boldsymbol{\varphi}} = [-\sin(\varphi), \cos(\varphi)], \qquad \hat{\boldsymbol{r}} = [\cos(\varphi), \sin(\varphi)]. \tag{3.5}$$

The perturbation ϵ refers to the perturbation from the radius of curvature R. They are related as: taking $R \to 0$ also results in the amplitude of the wave going to zero. The amplitude of the travelling wave is ϵR. Thus, ϵ is the amplitude relative to the radius.

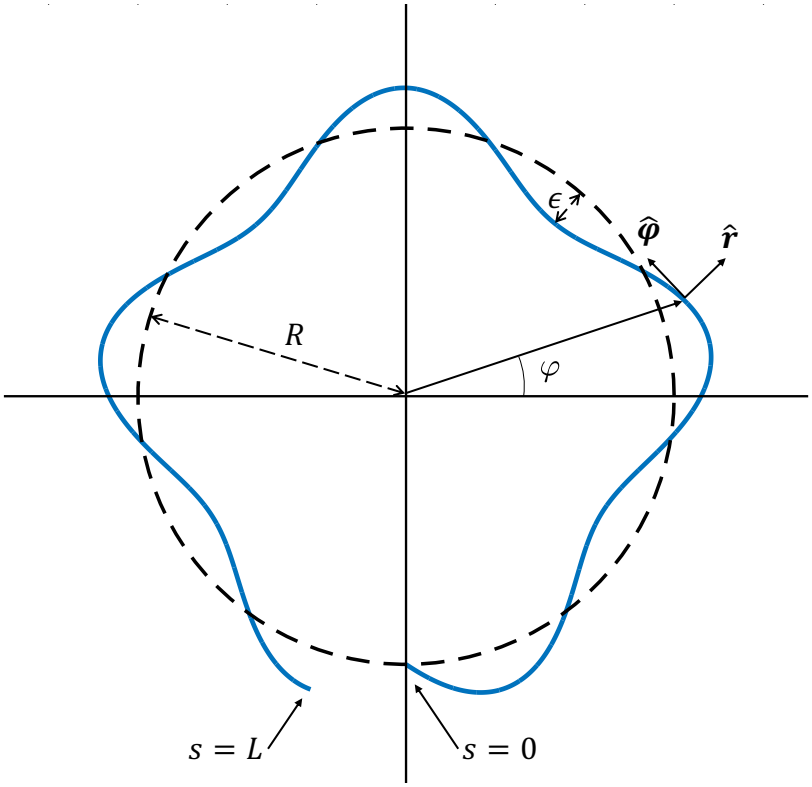

Figure 3.1: A schematic illustrating the basis for our analytical result. For $f(\varphi - ct)$ which prescribes the shape of the undulator via $\boldsymbol{x}(\varphi, t) = \boldsymbol{R}(\theta)\{R[1 + \epsilon f(\varphi - ct)]\hat{\boldsymbol{r}}(\varphi)\}$ where $\hat{\boldsymbol{r}}(\varphi) = [\cos(\varphi), \sin(\varphi)]$, we show analytically that, in the instantaneous case, the viscous dissipation Φ relates to the radius of curvature of the body R via $\Phi = \epsilon^2 c^2 R^2 K_N \int_0^L f'^2 \mathrm{d}s$ with K_N the normal resistance coefficient, and $f' = \partial f / \partial \varphi$. This result is derived under the assumption that translational velocity is zero. Furthermore, it is shown that for a given A_B, there exists an optimal radius of curvature R that minimises the cost of locomotion, which approaches zero as A_B does.

Differentiating eq. (3.4) with respect to t, we obtain the velocity

$$\boldsymbol{u} = \dot{\theta} \frac{\mathrm{d}\boldsymbol{R}}{\mathrm{d}\theta}(R[1 + \epsilon f]\hat{\boldsymbol{r}}) + \boldsymbol{R}(\epsilon R \frac{\partial f}{\partial t}\hat{\boldsymbol{r}}) \tag{3.6}$$

$$= \dot{\theta} \frac{\mathrm{d}\boldsymbol{R}}{\mathrm{d}\theta}(R[1 + \epsilon f]\hat{\boldsymbol{r}}) + \boldsymbol{R}(-\epsilon c R f' \hat{\boldsymbol{r}}) \tag{3.7}$$

where f' denotes $\partial f / \partial \varphi$. Explicitly, here we have used the fact that, since f is a function of $\varphi - ct$ (ie a travelling wave), it is the case that $\mathrm{d}f/\mathrm{d}t = -c(\mathrm{d}f/\mathrm{d}\varphi)$.

Since $(\mathrm{d}\boldsymbol{R}/\mathrm{d}\theta)\hat{\boldsymbol{r}} = \boldsymbol{R}\hat{\boldsymbol{\varphi}}$, equation (3.6) becomes

$$\boldsymbol{u} = \dot{\theta}\boldsymbol{R}(R[1+\epsilon f\,]\hat{\boldsymbol{\varphi}}) + \boldsymbol{R}(-\epsilon c R f'\hat{\boldsymbol{r}}). \tag{3.8}$$

The unit tangent vector along the body is given by

$$\hat{\boldsymbol{t}} = \frac{\partial \boldsymbol{x}/\partial\varphi}{|\partial \mathbf{x}/\partial\varphi|}. \tag{3.9}$$

Computing the numerator and denominator of $\hat{\boldsymbol{t}}$, we obtain

$$\frac{\partial \boldsymbol{x}}{\partial\varphi} = \boldsymbol{R}[\ \epsilon R f'\hat{\boldsymbol{r}} + R(1+\epsilon f)\hat{\boldsymbol{\varphi}}\,] \tag{3.10}$$

and

$$\left|\frac{\partial \boldsymbol{x}}{\partial\varphi}\right|^2 = R^2[(1+\epsilon)^2 + \epsilon^2 f'^2]. \tag{3.11}$$

Denoting $|\partial\boldsymbol{x}/\partial\varphi| = a$ to simplify notation, we obtain

$$\hat{\boldsymbol{t}} = \boldsymbol{R}\Big[\epsilon\frac{R}{a}f'\hat{\boldsymbol{r}} + \frac{R}{a}(1+\epsilon f)\hat{\boldsymbol{\varphi}}\,\Big]. \tag{3.12}$$

To determine the force per unit length $\boldsymbol{f}$, which by the resistive force model is given by

$$\boldsymbol{f} = (K_T - K_N)(\boldsymbol{u}\cdot\hat{\boldsymbol{t}})\hat{\boldsymbol{t}} + K_N\boldsymbol{u}, \tag{3.13}$$

we require an expression for $\boldsymbol{u}\cdot\hat{\boldsymbol{t}}$. In the instantaneous case, we take $\theta = 0$ such that $\boldsymbol{R} = \boldsymbol{I}$. It follows that

$$\boldsymbol{u}\cdot\hat{\boldsymbol{t}} = \dot{\theta}\frac{R^2}{a}(1+\epsilon f)^2 - \epsilon^2\frac{R^2}{a}cf'^2. \tag{3.14}$$

For $\epsilon \ll 1$, we have to leading order

$$a = R + O(\epsilon). \tag{3.15}$$

Thus, we have that

$$\boldsymbol{u}\cdot\hat{\boldsymbol{t}} = \dot{\theta}R - \epsilon^2 Rcf'^2. \tag{3.16}$$

Similarly,

$$\hat{\boldsymbol{t}} = \hat{\boldsymbol{\varphi}} + \epsilon f'\hat{\boldsymbol{r}}\,, \tag{3.17}$$

$$\boldsymbol{u} = R\dot{\theta}\varphi - \epsilon cRf'\hat{\boldsymbol{r}}. \tag{3.18}$$

Thus,

$$\boldsymbol{f} = (K_T - K_N)[\dot{\theta}R - \epsilon^2 Rcf'^2](\hat{\boldsymbol{\varphi}} + \epsilon f'\hat{\boldsymbol{r}}) + K_N(R\dot{\theta}\hat{\boldsymbol{\varphi}} - \epsilon cRf'\hat{\boldsymbol{r}}). \tag{3.19}$$

Recall that the viscous dissipation Φ is given by

$$\Phi = \int_0^L \boldsymbol{f}\cdot\boldsymbol{u}\,\mathrm{d}s \tag{3.20}$$

$$= \int_0^L \left[(K_T - K_N)(\boldsymbol{u}\cdot\hat{\boldsymbol{t}})^2 + K_N\boldsymbol{u}^2\right]\mathrm{d}s. \tag{3.21}$$

Hence, evaluating this integral with our expressions for $\boldsymbol{u}$ and $\boldsymbol{f}$ given by eq. (3.18) and eq. (3.19) respectively, the analytical expression for the viscous dissipation is given by

$$\check{\Phi} = \int_0^L (K_T - K_N)[\dot{\theta}R - \epsilon^2 cR^2 f'^2]^2\mathrm{d}s + K_N\int_0^L \left[R^2\dot{\theta}^2 + \epsilon^2 c^2 R^2 f'^2\right]\mathrm{d}s. \tag{3.22}$$

Recall also that to ensure no external forcing, the dynamics of the resistive force model are set by conditions ensuring zero net force and zero net torque. Imposing the latter of these constraints, we require that

$$\int_0^L \hat{\boldsymbol{z}}\cdot(\boldsymbol{x}\times\boldsymbol{f})\,\mathrm{d}s = 0. \tag{3.23}$$

This yields

$$K_T \int_0^L \dot{\theta} R^2 \, ds - (K_T - K_N)\epsilon^2 R^2 c \int_0^L f'^2 \, \mathrm{d}s = 0. \tag{3.24}$$

Hence

$$\dot{\theta} = (1 - \frac{K_N}{K_T})\frac{\epsilon^2 c}{L} \int_0^L f' \, \mathrm{d}s. \tag{3.25}$$

Therefore, to leading order in ϵ, the analytically determined viscous dissipation is given by

$$\check{\Phi} = \epsilon^2 c^2 R^2 K_N \int_0^L f'^2 \mathrm{d}s. \tag{3.26}$$

Recall our objective function which describes the cost of the undulatory gait is

$$F = (1 - A_B)\Phi + A_B \mathcal{P}_{\text{Bending}} \tag{3.27}$$

where

$$\mathcal{P}_{\text{Bending}} = \int_0^L \left(\frac{\partial \psi}{\partial s} \right)^2 \mathrm{d}s \tag{3.28}$$

which is derived from the elastic energy stored in the bending of the body, where $\partial\psi/\partial s$ denotes the curvature. In this parametrisation, to leading order in ϵ the curvature is $1/R$. This is can be seen clearly by construction of this basis, that the curvature is due to the radius of the circle along which the undulator is travelling (for more detail, an in-depth derivation of how $\psi(s,t)$ is related to $f(\varphi,t)$ is given in appendix section A.2). Hence, the analytical expression for the bending term is given by

$$\check{\mathcal{P}}_{\text{Bending}} = \frac{L}{R^2}. \tag{3.29}$$

Thus we obtain, to leading order:

$$F = (1 - A_B)\epsilon^2 c^2 R^2 K_N \int_0^L f'^2 \mathrm{d}s + A_B \frac{L}{R^2}. \tag{3.30}$$

Recall that the perturbation ϵ is the amplitude of the undulation relative to the radius of curvature R. That is, the perturbation of the body away from the circle of radius R is equal to ϵR. As we are in the limit $\epsilon \ll 1$, a factor of ϵ does not appear in the approximation of the bending energy. What we observe from the form of eq. (3.30) is that the bending cost is related to the overall radius of curvature of the body, and the hydrodynamic cost (the viscous dissipation) is a function of the undulating wave propagating along the body length.

To find the optimal (ie minimum) cost as a function of the radius of curvature, it is necessary to compute $\mathrm{d}F/\mathrm{d}R = 0$. Evaluating this derivative, we solve for R in terms of A_B to find the following relationship between the optimal radius of curvature R and A_B:

$$\frac{\mathrm{d}F}{\mathrm{d}R} = 0 \quad \Longrightarrow \quad R^4 = \frac{A_B L}{(1-A_B)\epsilon^2 c^2 K_N \int_0^L f'^2 \,\mathrm{d}s}. \tag{3.31}$$

Hence, as we reduce the importance of bending in the cost function, as we decrease the penalty for bending in the body, taking $A_B \to 0$, there exists some optimal radius of curvature R that minimises our cost function F, and this R also tends towards 0. This optimal radius of curvature scales relative to A_B according to

$$A_B \sim R^4. \tag{3.32}$$

The result illustrates that the mechanical cost can be minimised by shrinking and reducing in size, which is not a surprising outcome. The bending cost was determined to be a function of the overall radius of curvature (R). The hydrodynamic cost is a function of the undulatory wave (ϵ and f). When the importance of bending cost is reduced, the undulator can assume increasingly tightly-coiled shapes. Through the derivation of this result we have quantitatively established that in order for the optimisation not to predict shapes of increasing curvature, we need to place some restriction on the shape space. This is a useful conclusion, and our

principal interpretation of this result is applicable in guiding the optimisation.

3.2.2 Numerical confirmation of analytical result

We can confirm this analytical result numerically by specifying the shape using this basis with respect to the origin. As the result is obtained in the instantaneous case, we simply prescribe

$$f(\varphi) = \sin(k\varphi) \tag{3.33}$$

and choose wavenumber $k = 4\pi$, and $\varphi \in (0, 6\pi)$. This choice of f here is made as it is a simple sine wave of size ϵ propagating along the length of the body, that itself has an overall radius of curvature R. We expect the approximation to hold for any f provided that $1/k$ is not too small. Furthermore, the derivative of f with respect to φ should remain small relative to R^{-2}, such that there is no breakdown in the asymptotic structure..

The results of this numerical confirmation are shown in fig. 3.2. The analytical viscous dissipation can in fact be computed without any assumptions on ϵ. Comparing the numerically determined dissipation Φ with that given by the expression obtained analytically $\check{\Phi}$, dividing by the factor of $\epsilon^2 R^2$ for both, we see that as $\epsilon \to 0$, the numerical and analytical result agree increasingly. Similarly, for the bending term, the numerically determined $\mathcal{P}_{\text{Bending}}$ agrees with the analytical expression $\check{\mathcal{P}}_{\text{Bending}}$ increasingly as $R \to 0$. The range of R for which the two agree expands to greater radii of curvature as we take $\epsilon \to 0$.

For a fixed value of ϵ we can perform a parameter sweep over a range of A_B and R values, and evaluate the cost function F for a given A_B and R. For a given A_B, the optimal radius of curvature R can be found by seeking the point in the landscape where F is minimised. To demonstrate the derived result that this optimal radius of curvature relates to the bending importance according to $R^4 \sim A_B$, the slope of the optimal R is determined using the MATLAB `polyfit` function, by fitting a

polynomial of degree 1 to the points. The slope of the line fitted for both example cases shown here ($\epsilon = 10^{-3}$ and 10^{-5}) is approximately 4, which confirms our derived result.

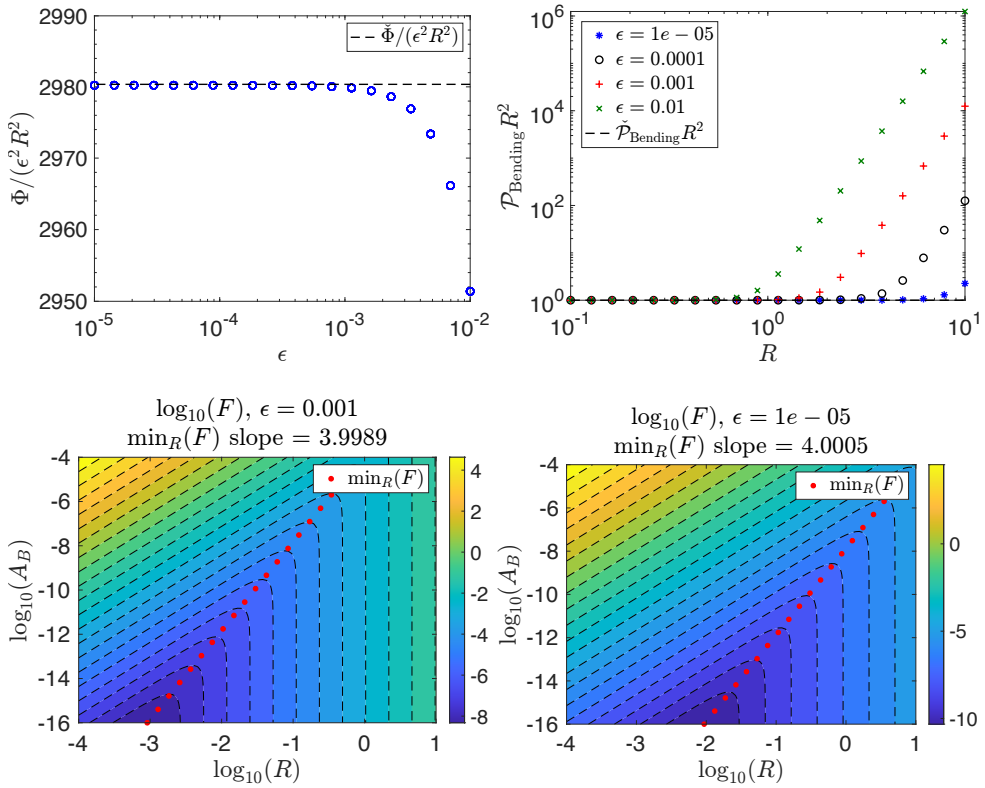

Figure 3.2: Numerical confirmation of analytical result which shows that reducing the radius of curvature yields the optimal undulatory turn. The numerically determined viscous dissipation Φ agrees increasingly with the analytical result $\breve{\Phi}$ as $\epsilon \to 0$, independent of R. For the bending term, the numerical $\mathcal{P}_{\text{Bending}}$ and analytical $\breve{\mathcal{P}}_{\text{Bending}}$ agree increasingly as both R and ϵ decrease. To demonstrate the result that the optimal $R^4 \sim A_B$, we show two examples: $\epsilon = 10^{-3}$ and 10^{-5}. Fitting a polynomial of degree 1 to the optimal radii of curvature across a range of A_B values yields slopes of 3.9989 and 4.0005 respectively, confirming with our analytical result.

3.2.3 Optimisation

The principal takeaway from the analytical result is that, in the numerical optimisation problem, when optimising reorientation (as opposed to path-optimisation), we need to choose the shape space such that there is some limitation on the curvatures of the shapes. We now consider the question of how the optimisation controls changing the travelling wave shape versus the overall radius of curvature. Given that the optimal gait is established by decomposing the tangent angle onto a finite number of modes, we seek to determine how exactly does the optimisation routine balance tuning modes which parametrise the travelling wave with those which control the overall radius of curvature.

We now consider the case of running the optimisation routine, solving the optimisation problem for a shape space relevant to our analytical result, for a more general set of shapes. The set of parameters to be optimised yields a shape with constant curvature, plus a travelling wave propagating along it. This is a more general shape space compared with that prescribed for the analytical result.

By allowing the shape of the travelling wave to change, as well as the swimmer radius of curvature, we can observe how the optimisation routine decides what is optimal. Specifically, we can determine if there is a preference in changing the travelling wave shape versus changing the overall radius of curvature in order to achieve the optimal gait.

We prescribe the tangent angle — for arc length $s \in [0, L]$ (ie point along the body from head to tail) and $t \in [0, T]$ where $T = 1/k$ is one fundamental period of the waveform — as

$$\psi(s,t) = cs + \sum_{n=1}^{n^*} a_n \cos(2\pi n(s-t)) + b_n \sin(2\pi n(s-t)) \tag{3.34}$$

where a_n, b_n for $n = 1$ to n^* (as in chapter 2) are Fourier modes parametrising the travelling wave shape, to be determined in the optimisation such that F is

minimised. Additionally, the parameter $c \in \mathbb{R}$ is also included in the set of control parameters to be determined by the optimisation. This parameter allows the body shape to assume an overall constant curvature via the cs term in the expression. Changes to c imply changes in the overall radius of curvature. This parametrisation of $\psi(s,t)$ is equivalent to that used in chapter 2 to determine the optimal straight-path forwards gait with $k = 1$, plus the constant curvature term cs.

The model parameters that are set prior to optimisation are A_B, r_k and θ^*. We select two fixed values of A_B: 10^{-2} and 10^{-4}, which were chosen to distinguish qualitative differences in the results when the cost function is mostly bending versus mostly hydrodynamics. These choices of A_B are based on results from chapter 2. For $A_B = 10^{-2}$ the optimal straight path gait was in the sinusoidal regime. For $A_B = 10^{-4}$ and lower, an interesting transition occurred where optimal gaits became increasingly sawtooth, and optimal wavenumbers jumped discontinuously, exhibiting bias towards half-integer values. Thus, choosing $A_B = 10^{-2}$ and 10^{-4} will highlight categorical differences in optimal turning behaviour, between bending cost contributing significantly, and dissipation dominating the mechanical cost. Recall that for lower values of A_B, bending is penalised less in our objective function F. For the two values of A_B, and setting $r_k = 1/2$, we run the optimisation routine, fixing the parameter θ^* for increasingly sharp turning angles from $\pi/32$ to π. The results are shown in fig. 3.3.

Examining the cost function F as a function of θ^*, we see that the higher the turning angle, the higher the cost. We also observe that as θ^* increases, the magnitude of the optimal value of c also increases. This shows that, for a larger turning angle, it is optimal to increase the radius of curvature, for both values of A_B tested. Note that this observation is not by construction. The turning angle θ^* is not built into the mechanical cost objective function. That is, the objective function does not depend on θ^*, and only is linked to the dissipation and the bending cost. Our motivation for investigating this particular optimisation problem is to observe how the routine balances changing the overall radius of curvature, versus changing the

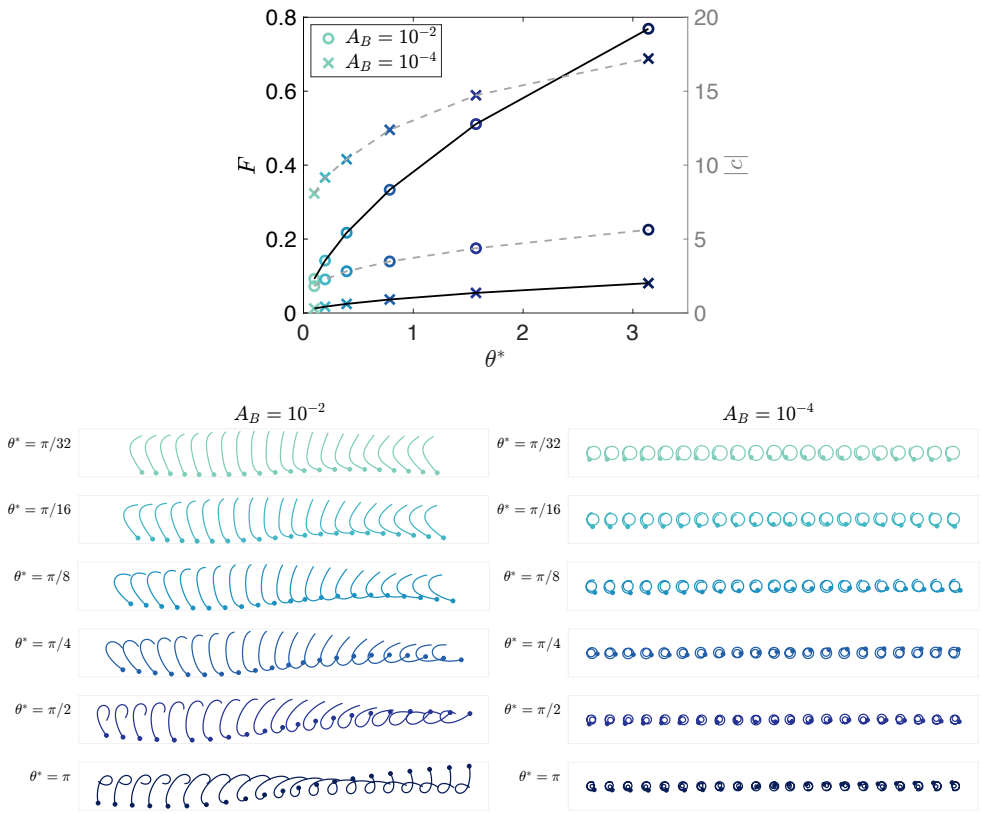

Figure 3.3: Results for the optimal turns for prescribing the tangent angle $\psi(s,t)$ via (3.34). For increasing θ^*, both the cost F (solid black line, left axis) and optimal radius of curvature c (dashed grey line, right axis) also increase, for both values of A_B. Reducing A_B results in reducing the radius of curvature, as confirmed with the previous analytical and numerical result. Dots in the optimal turning gaits here and henceforth indicate the point $s = 0$ (the 'head' of the slender body) and are for purely indicative purposes.

shape of the propagating wave. In this scenario, we have relaxed the assumptions made in our analytically derived result above, and more simply investigate what happens if this reduction in the radius of curvature occurs in a more general setting, without the assumptions of the analytical framework. We have determined that having a high bending cost does regularise the problem somewhat. For high A_B, realistic gaits can be obtained without extreme control on the shape space.

We can observe this trend by looking at the turns themselves, noticing the change in gait as the turning angle increases. Distinctively, we see that for the lower A_B (the case where bending is penalised less, and the cost function is mostly viscous

dissipation) the radius of curvature is significantly higher. The shapes for $A_B = 10^{-4}$ are visibly more curled-up than those for $A_B = 10^{-2}$. This further emphasises our analytical result, that for lower A_B it is more optimal to curl up more tightly.

3.2.4 Prescribing the shape space for modelling optimal undulatory turning

With the results presented in this section we have demonstrated that as $A_B \to 0$ the optimal gait is achieved by curling up tightly, reducing the radius of curvature and shrinking to a dot. Whilst this is an interesting mathematical result, much like Lighthill's saw-tooth, in the biological context organisms are limited in their capacity to assume such shapes. The extreme cases of our results are not physically possible for many undulatory microorganisms. Lighthill remarked that, in the context of straight-path forwards locomotion "real flagella possess some minimum achievable radius of curvature of bending, which would prevent the from achieving the saw-tooth waveform" [9]. The same can be said of these tiny radius of curvature shapes.

Therefore, in order to prevent our optimisation routine simply taking all our turns to curl up tightly, we must choose our shape space carefully such that there is some inherent constraint on the curvature, either explicitly written as a constraint in the optimisation, or fundamentally required by the shape space. For instance, we can require the body to start and end in a straight zero-curvature configuration, or that the curvature in the body must integrate to zero over one period. Thus, the constraints in the optimisation and/or the expression chosen for $\psi(s,t)$ must take this into account.

3.3 Results

Before we analyse the results and effects of prescribing different shape spaces, we first describe the model parameters that are to be set prior to running the numerical optimisation routine.

Setting parameter values prior to optimisation

We obtain optimal turning gait results for two different values of A_B: $A_B = 10^{-2}$ and 10^{-4}, which were chosen to investigate qualitative differences when bending is penalised more or less. For $A_B = 10^{-2}$, the emphasis is on minimising curvature cost. This contrasts with $A_B = 10^{-4}$, where the emphasis is on minimising environmental cost.

The turning angle θ^* is also fixed prior to optimisation, for a series of increasingly sharp turns: $\theta^* = \pi/32$, $\pi/16$, $\pi/8$, $\pi/4$, $\pi/2$, π. When running the numerical optimisation, the initial position in the routine is taken to be the optimal found for the immediate prior turning amount. Explicitly, starting with $\theta^* = \pi/32$, the starting values of the modes describing the tangent angle $\psi(s,t)$ are taken as normally-distributed random numbers, generated using MATLAB's `randn` function. Then for $\theta^* = \pi/16$, the initial position is taken to be the optimal waveform found for $\theta^* = \pi/32$. And so on, for $\theta^* = \pi/8$ the initial position is the optimal found for $\theta^* = \pi/16$, etc. This continuation in the initial position for the optimisation was successful in ensuring convergence to the optimal solution, as opposed to using a random initial position for each case.

The drag anisotropy r_k is fixed at $1/2$, to model swimming micro-undulators.

3.3.1 Fourier travelling waves

From our analytical result we established that the shape space needs to be carefully chosen such that there is some constraint on the curvature that the body can assume, either via the expression for ψ or including additional constraints in the optimisation.

Our initial approach to constraining the curvature in the body does not require an additional constraint to be explicitly included. Rather, the shape space that $\psi(s,t)$ occupies is limited to that of travelling waves. Prescribing the tangent angle as

$$\psi(s,t) = \sum_{n=1}^{n^*} a_n \cos(2\pi nk(s-t)) + b_n \sin(2\pi nk(s-t)), \tag{3.35}$$

which is the expression used in chapter 2 , and is also equivalent to the expression used in section 3.2.3 without the constant curvature term. As a result of removing the radius of curvature term, the wave-averaged curvature is zero:

$$\int_0^{1/k} \frac{\partial \psi}{\partial s}\, \mathrm{d}s = 0. \tag{3.36}$$

The Fourier modes a_n, b_n for $n = 1, ..., n^*$ are the control parameters to be determined by the optimisation routine. This expression for $\psi(s,t)$, which is a travelling wave and a finite sum over n^* Fourier modes, we refer to as 'Fourier ψ'.

In addition to setting A_B, θ^* and r_k prior to optimisation, we also want to investigate the effect of changing the period and wavenumber of the travelling wave propagating along the body length. In this shape space the wavenumber k also needs to be fixed prior to optimisation, due to the fact that our objective is to minimise the cost function. We therefore test several fixed values of k in our model: $k = 1.5, 1, 0.5, 0.25$ and 0.1, and determine the optimal turn for each case.

Results for $A_B = 10^{-2}$

Setting the value of $A_B = 10^{-2}$, an overview of the resulting optimal turning gaits is shown in fig. 3.4. The results show that the cost of turning decreases monotonically with both decreasing k and decreasing θ^* (fig. 3.4i). Hence, it is consistently more costly to perform a larger turn, for a higher wavenumber.

The resulting costs as a function of k can be understood by examining the shapes themselves. For example, for a given turning angle — here isolating $\theta^* = \pi/4$ — we observe that the body curvatures decrease as k decreases (fig. 3.4ii). This is as expected — for $A_B = 10^{-2}$ the cost function F depends mostly on $\mathcal{P}_{\text{Bending}}$, and we see the radius of curvature decrease as k decreases. The most optimal turns, for all values of θ^*, result from when k is minimised, ie when the period of the waveform is extended.

Examining the optimal turns for low wavenumber ($k = 0.1$) we see that for increasing turning angle θ^*, the larger turns require higher curvatures (fig. 3.4iii). This is shown in the waveforms and also quantitatively in fig. 3.4iv, where we can examine $\partial\psi/\partial s$ as a function of s/k, as well as the maximum value of $|\partial\psi/\partial s|$ in the wave over the period of the turn. Not only is the magnitude of the maximum curvature increasing as the turning angle increases, but the near constant curvature assumed by the undulator for the initial portion of the wave is also greater as the turning angle increases — the y-intercept in fig. 3.4iv increases as θ^* increases. This is an effect of the form of our expression for ψ, and that the curvature integrates to zero over one period. If the maximum curvature must increase in order to perform a larger turn, the curvature in the body at its initial configuration balances this out.

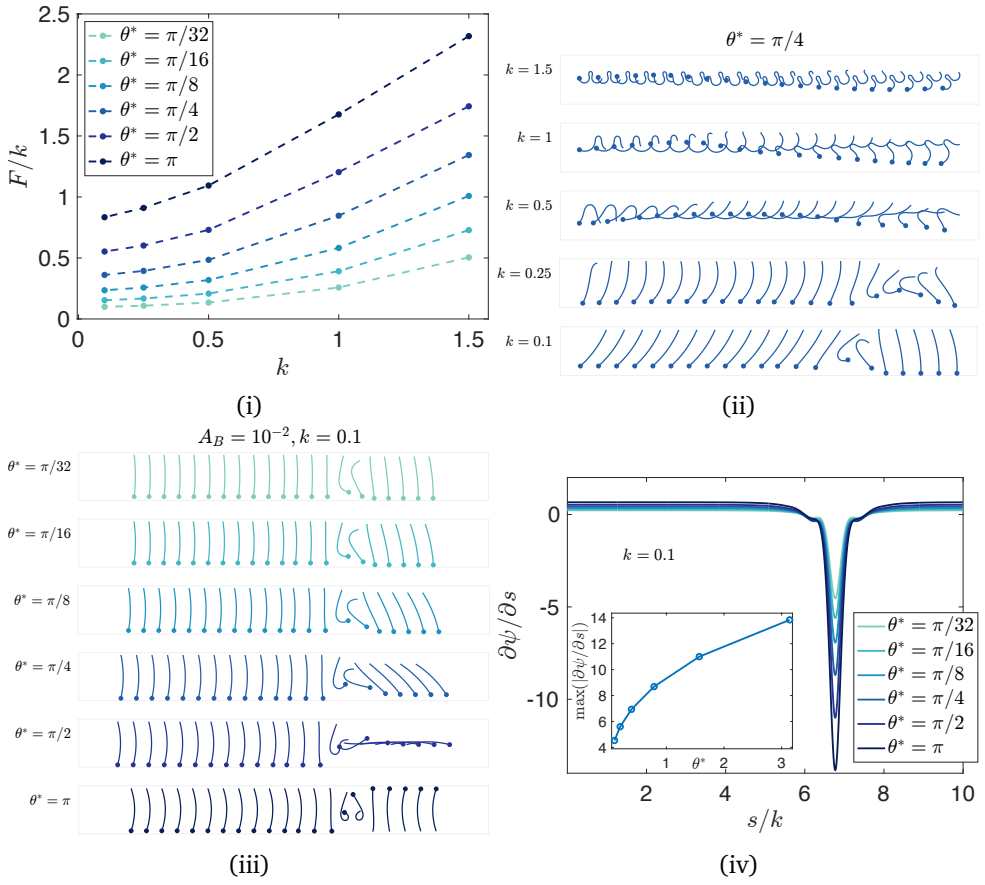

Figure 3.4: Optimal turning results for $A_B = 10^{-2}$ for Fourier ψ. 3.4i: The total cost F/k as a function of wavenumber k increases monotonically with both wavenumber and turning angle θ^*. 3.4ii: Isolating $\theta^* = \pi/4$, we can observe the change in optimal turning behaviour as the wavenumber decreases. 3.4iii: Fixing $k = 0.1$ for which we find the optimal turns with the lowest cost, we can observe the change in turning behaviour as the turning angle θ^* increases. 3.4iv: The curvature of the optimal turning waveforms in s over a period for $k = 0.1$. The maximum curvature magnitude increases as θ^* increases.

Results for $A_B = 10^{-4}$

We now consider the case of setting $A_B = 10^{-4}$. With this smaller value of A_B, we have reduced the importance of bending in the cost function, so F now depends mostly on hydrodynamics, and high-curvature shapes incur a lower penalty. An overview of the results for this lower value of A_B is shown in fig. 3.5.

Overall, the total cost of turning for the $A_B = 10^{-4}$ cases are lower than for the 10^{-2} case, as indicated by the vertical axis in fig. 3.5i. However, there are several more prominent differences between these results and those for $A_B = 10^{-2}$. Firstly, we see here that F is no longer monotonically increasing with θ^* when k is 1 or greater. For example, when $k = 1$ it is more costly to perform of $\pi/2$ than it is to perform a turn of π. The highest total cost incurred is for wavenumber $k = 0.25$, performing a turn of π.

These results can be investigated further by again isolating a single turning angle ($\theta^* = \pi/4$) and examining the changes in waveform as the wavenumber changes. Similarly to the $A_B = 10^{-2}$ case, we see a qualitative decrease in curvature as k decreases (fig. 3.5ii). Why then is the total cost higher for $k = 1$ compared with $k = 1.5$? As the wavenumber becomes greater than 1, the body assumes multiple wavelengths when performing the turn. Between $k = 1$ and $k = 1.5$, the 'peak' of the waveform does not change significantly — the magnitude of the curvature in the body grows increasingly up to a sharp peak, before sloping back down. The terms in our cost function F are time-averaged over a single period of the wave, and for a higher value of k, this period is lower. Hence, for a similar shape over one wavelength, for the total cost F/k (the total cost of turning over one period), this value is lower for $k = 1.5$ versus $k = 1$. This explanation also applies to $\theta^* = \pi/2$ and π, for k increasing from 0.1 to 1.5.

For $\theta^* = \pi/4$, the peak of the wave (the point of highest-magnitude curvature) becomes increasingly smooth as k gets smaller. Considering the implication of k

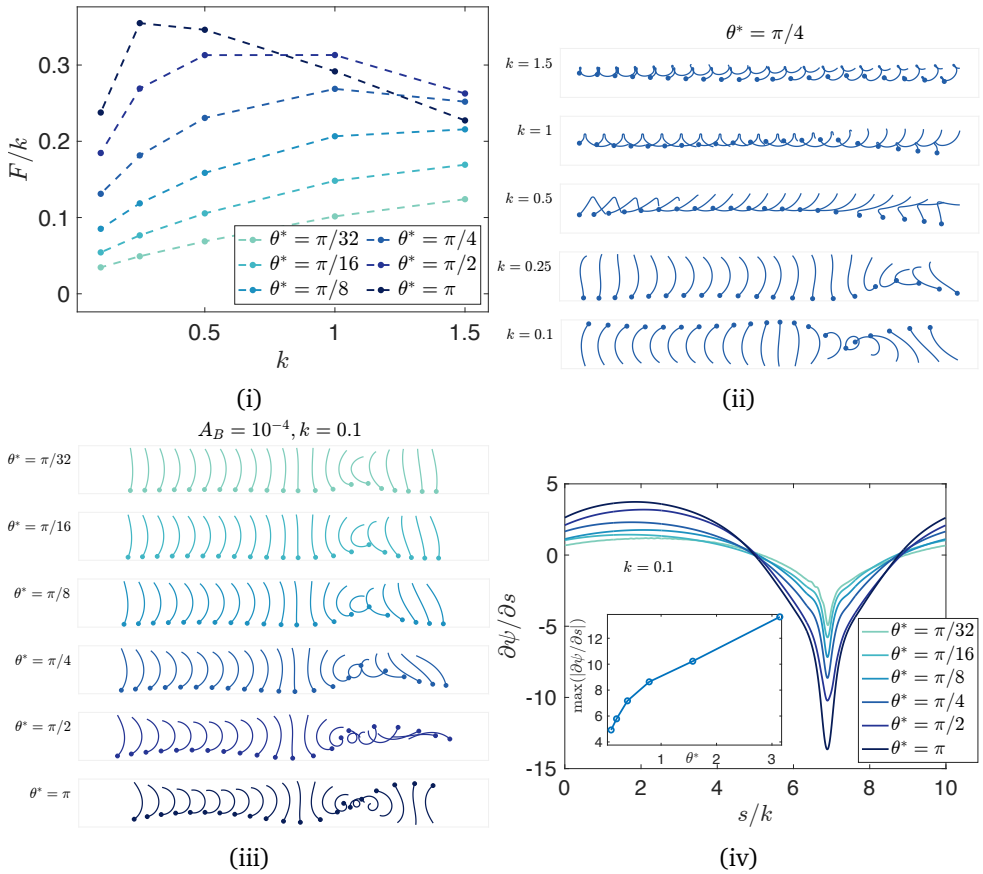

Figure 3.5: Optimal turning results for $A_B = 10^{-4}$ for Fourier ψ. 3.5i: The monotonic relationship observed for $A_B = 10^{-2}$ is not seen here. The total cost F/k as a function of wavenumber k increases monotonically in θ^* for $k < 1$. 3.5ii: Isolating $\theta^* = \pi/4$, we can observe the change in optimal turning behaviour as the wavenumber decreases. 3.5iii: Fixing $k = 0.1$ for which we find the optimal turns with the lowest cost, we can observe the change in turning behaviour as the turning angle θ^* increases. 3.5iv: The curvature of the optimal turning waveforms in s over a period for $k = 0.1$. The maximum curvature magnitude increases as θ^* increases.

in our expression for ψ, in that, for example, the $n = 20$ Fourier mode for $k = 0.1$ is the equivalent 'wiggle' to the $n = 2$ mode for $k = 1$, this explains how, for lower wavenumbers, the transition from switching sign in $\partial\psi/\partial s$ is smoother. For smaller k, the modes which parametrise the shape are prescribing more 'wiggles' at the lower frequency end.

This smoothness can be seen by, again, isolating the optimal turns for $k = 0.1$. For this low value of k, looking at the turns we can see an increase overall in

the curvature of the body compared with $A_B = 10^{-2}$ (fig. 3.5iii). Especially for the larger values of θ^*, the body assumes a distinctly more curled initially posture, before bending and coiling in the opposite direction in order to perform the turn. This can be examined quantitatively again in the s/k against $\partial\psi/\partial s$ plot (fig. 3.5iv), and again follows from the fact that for this expression of ψ the curvature integrates to zero over one period. However, this is notably different from the analogous figure for $A_B = 10^{-2}$, as instead of maintaining a near-constant curvature before and after turning, $\partial\psi/\partial s$ increases significantly, before switching signs in order to perform the turn. Furthermore, this transition from positive to negative curvature happens much less abruptly than for the $A_B = 10^{-2}$ case, and overall the transition is smoother. Whilst the maximum curvatures between the two A_B values for θ^* are very similar, this optimal turning strategy was not realised in the $A_B = 10^{-2}$ case as this increase in curvature would have incurred unnecessary cost in the objective function.

Expanding the shape space

As we observed in section 3.2.3, we see that for lower A_B, it is optimal to decrease the overall radius of curvature of the body. The results for this Fourier ψ highlight the qualitative difference in optimal turning strategy for these two different values of A_B. This parametrisation of the tangle angle prescribes that shape of the waveform as a travelling wave. In the context of optimal straight-path forwards locomotion, Pironneau and Katz (1974) [17] derived that travelling waves are hydrodynamically optimal by solving the optimisation problem, imposing a constraint on net linear velocity over one period. More recently, Lauga (2020) [22] obtained the result that travelling waves are hydrodynamically optimal for long-wavelength flagella.

There is a lot of evidence that travelling waves are optimal for the straight-path forwards motion problem. But how optimal are travelling waves for undulatory

turning strategies? We investigate this question now by expanding the shape space to beyond only travelling waves, decoupling space and time and reducing the limitations on the variety of shapes that can be assumed in the shape space.

3.3.2 Chebyshev waves

The Fourier results assumed a travelling-wave shape for the optimal turning gaits. In this section we relax this assumption and expand the shape space, taking inspiration from Alben (2013) [57], which considers the problem of optimising snake locomotion in the plane. In this study the tangent angle is prescribed using Chebyshev polynomials in s, decoupling space and time so that ψ is no longer a function of $s-t$. The shapes that this parametrisation allows can therefore change in time in a more general way.

We now prescribe the shape of the body via parametrising the curvature as

$$\kappa(s,t) = \sum_{m=0}^{m^*-1} \sum_{n=0}^{n^*-1} (\alpha_{mn} \cos(2\pi m t) + \beta_{mn} \sin(2\pi m t)) T_n(s) \tag{3.37}$$

where T_n is the nth Chebyshev polynomial in s:

$$T_n(s) = \cos(n \cos^{-1}(s)). \tag{3.38}$$

The prescribed curvature is periodic in time with the same period T a previously:

$$\kappa(s,t) = \kappa(s,t+T), \tag{3.39}$$

and the tangent angle is recovered by integration:

$$\psi(s,t) = \int_0^s \kappa(s',t)\,\mathrm{d}s'. \tag{3.40}$$

Without loss of generality, $\psi(0) = 0$. This expression for the tangent angle is

referred to as 'Chebyshev ψ'. The control parameters α_{mn}, β_{mn} for $m = 1, ..., m^*$ and $n = 1, ..., n^*$ are now the modes to be determined by the optimisation routine. The parameters fixed prior to optimisation are i) A_B, which again we fix at 10^{-2} and 10^{-4}, ii) r_k, which remains fixed at $1/2$, and iii) θ^*, we again we fix at $\pi/32, \pi/16, ..., \pi/2, \pi$. In alignment with Alben (2013) [57], we choose $n^* = m^* = 5$.

We are thus generalising the shape space such that the waveform is not necessarily periodic in s. Time-periodicity is however still incorporated in this parametrisation of the shape. The terms in $\kappa(s,t)$ with coefficients β_{0n} are zero by construction, so the objective function F is thus minimised in 45-dimensional space ($(2m^* - 1)n^*$ dimensions). This number of control parameters is small enough to enable convergence to the minima, whilst not considerably slowing said convergence and sufficiently characterising biologically relevant curvatures [57].

The shapes that this parametrisation allows can change in time in a more general way, since s and t are decoupled, however the number of attainable shapes (in terms of the curvature) are limited by the value of n^* — the number of Chebyshev polynomials. There is therefore a trade-off with the travelling-wave case: here we can only reach a certain polynomial order that is much smaller than for the Fourier waves, but the shapes can change in a more general way.

Including an additional constraint

This generalised shape space of Chebyshev waves does not inherently constrain the curvature as our Fourier ψ does. Therefore we must include an additional constraint in the numerical optimisation routine requiring that that body start (and end, due to periodicity) in a straight posture:

$$\frac{\partial \psi}{\partial s}(s, t = 0) = 0. \tag{3.41}$$

This satisfies the required constraint on curvature in the body, the applicability of which is demonstrated by our analytical result (section 3.2.1). Furthermore, the choice of this constraint is motivated by what was observed for the low wavenumber $A_B = 10^{-2}$ case.

Results

An overview of the results for optimal turns for this Chebyshev shape space are shown in fig. 3.6. Between the two A_B values, the results for the optimal turning gaits upon first glance appear essentially identical. Examining these results more closely in fig. 3.7, for $A_B = 10^{-4}$ the maximum body curvature over time is marginally greater than for $A_B = 10^{-2}$. In particular, for the highest turning angle we considered, the body achieves a higher maximum curvature value along its length sooner in the period of the wave than for the lower A_B case.

There are also some low-magnitude waves present in the $A_B = 10^{-4}$ case (in particular these can be seen in the first few shapes for $\theta^* = \pi$). It is likely these are present due to not being eliminated in the optimisation routine from the random initial condition, as for this lower value of A_B they will contribute minimally to

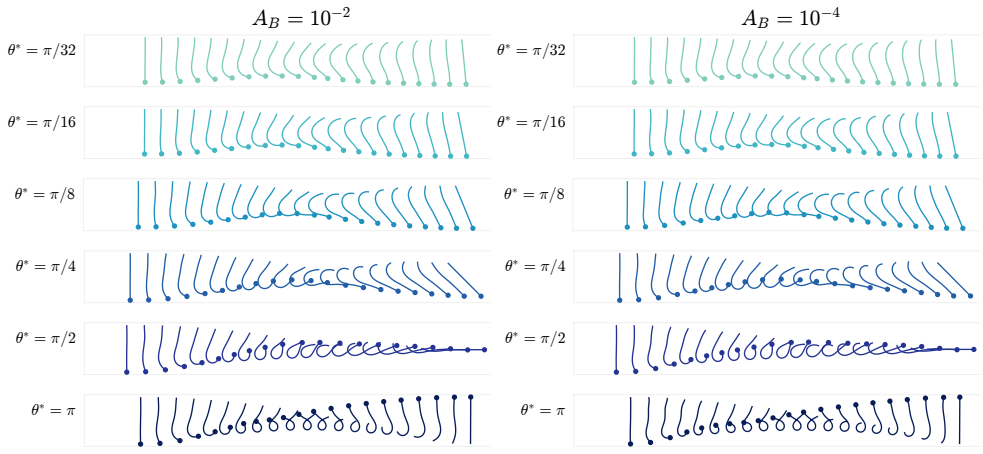

Figure 3.6: Optimal turn results for Chebyshev ψ. Between the two values $A_B = 10^{-2}$ and 10^{-4} there is no significant qualitative difference in behaviour for optimal turning. This is surprising as we would anticipate the $A_B = 10^{-4}$ to assume higher curvature shapes, as bending is penalised less in this scenario.

the objective function.

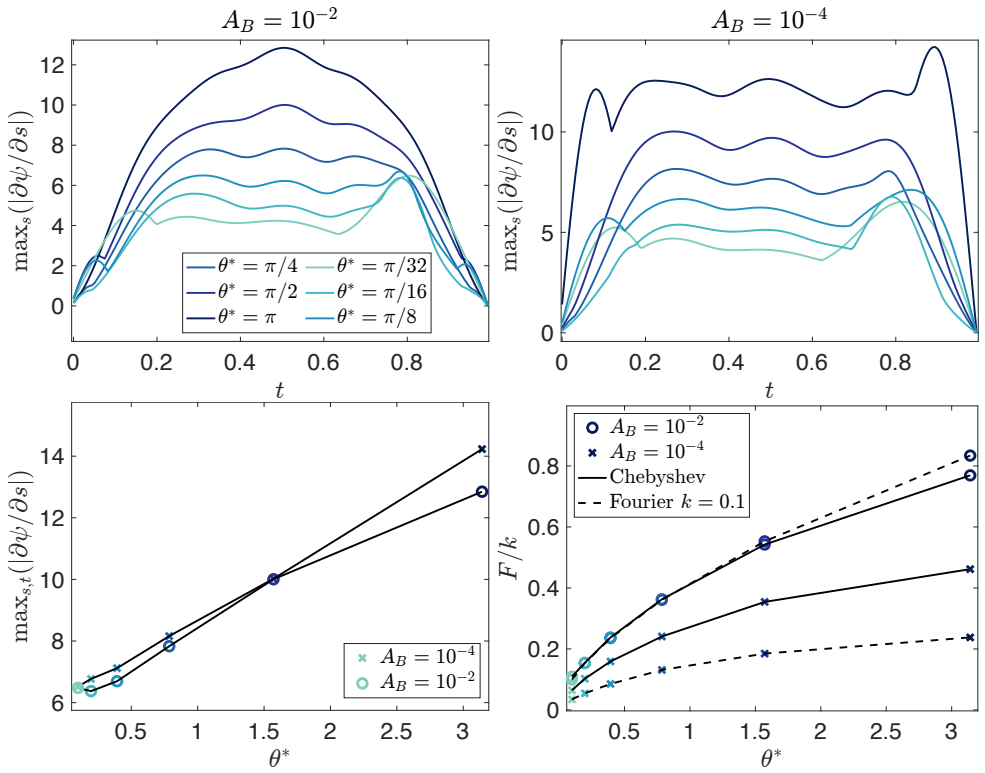

Figure 3.7: Analysis of results for optimal turns with Chebyshev ψ. For the two values of A_B, the maximum body curvature over time is largely similar. Comparing the optimal turns for this shape space with the least-costly optimal turns for the Fourier ψ: for $A_B = 10^{-2}$ the optimal turns for the Chebyshev shape space are marginally less costly, for 10^{-4} the Fourier $k = 0.1$ turns are more optimal, incurring overall a lower total cost.

Increasing the number of modes m^*, n^* had negligible effect on the optimal turn results, and we continued to find highly similar turning gaits between the two A_B values, across all turning angles θ^*. It is interesting and unintuitive that the optimal turns for $A_B = 10^{-2}$ and 10^{-4} are so similar in this case. We would expect, as we had seen previously, the 10^{-4} turns to assume a shape with higher curvature, as bending is penalised less in the objective function for this case. Because the constraint on curvature in this case is now explicitly included as $\partial\psi/\partial s(s, t_{end}) = 0$ in the optimisation routine, this is perhaps limiting the fundamental behaviour of the optimal turns in these results.

One possibility is that the numerical optimisation routine is just not computation-

ally capable of finding the globally optimal turning gait. The energy landscape maybe be very shallow and 'bumpy', with many local optima. We observed that as we remove the curvature cost (solving the optimisation with decreased A_B) the resulting optimal turns become more variable (see fig. 3.8). For different random initial conditions, the resulting optimal turning gait as determined by the numerical routine can vary significantly, in both shape and objective function value. The fact that the optimisation predicts identical shapes here for the two values of A_B requires further investigation.

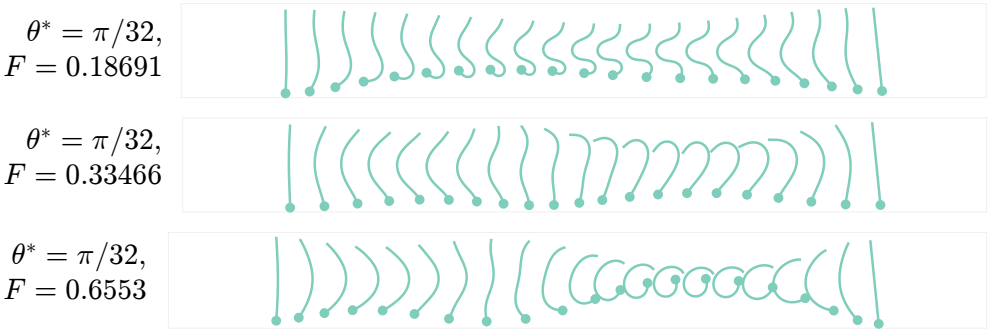

Figure 3.8: Turning results determined by the numerical optimisation routine for $\theta^* = \pi/32$ for the Chebyshev shape space, from three different random initial conditions in the solver. As the curvature cost is removed ($A_B = 10^{-4}$), the resulting optimal turns become more variable.

Chebyshev waves with non-zero curvature

In order to further investigate the results of this Chebyshev return-to-straight shape space for $A_B = 10^{-4}$, we can adapt the approach above to consider an alternative scenario. Suppose now that it is not the case that the body must be in a completely straight line initial configuration. We now adapt eq. (3.41) such that instead:

$$\frac{\partial \psi}{\partial s}(s, t = 0) = c^* \tag{3.42}$$

where $c^* \in \mathbb{R}$ (fixed and set prior to optimisation) is the curvature of the optimal gaits given by the Fourier $k = 0.1, A_B = 10^{-4}$ optimisation results. This adaptation

no longer requires that the body be in a completely straight line configuration, and is instead informed by the optimal starting configuration from the Fourier shape space. The motivation for this adaptation is to provide more insight into the $A_B = 10^{-4}$ results, in the regime where the objective function is dominated by hydrodynamic cost. We would expect the results of this optimisation problem to be less costly than those for the $\partial\psi/\partial s(s, t_{end}) = 0$, because the return-to-non-zero-curvature c^* is informed by the Fourier results, which were found to be more optimal (see fig. 3.7).

The resulting optimal gaits from this adaptation of the curvature constraint are shown in fig. 3.9. And the resulting mechanical cost of these optimal gaits in this shape space with the adapted curvature constraint are shown in fig. 3.10. Surprisingly, contrary to our expectation we find in fact that the $\partial\psi/\partial s(s, t_{end}) = c^*$ turns are less optimal than the previous $\partial\psi/\partial s(s, t_{end}) = 0$ case. This is likely due to the intermediate S-shaped posture assumed by the undulator between its initial and final configuration, which intuitively contributes highly to the cost function.

The results of this Chebyshev shape space that enable undulations in a more general way compared with the Fourier, as well as the possible approaches to adapting the curvature constraint, remain open to scrutiny.

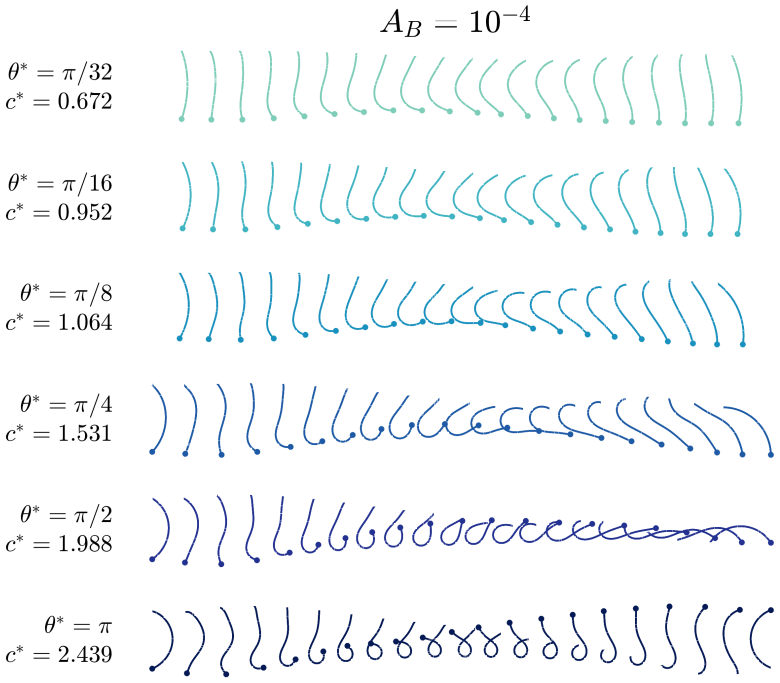

Figure 3.9: Optimal turn results for Chebyshev ($A_B = 10^{-4}$) with the constraint on the curvature now given by $\partial\psi/\partial s(s, t_{end}) = c^*$, where c^* is taken to be the curvature of the initial and final postures of the optimal Fourier $k = 0.1$ results.

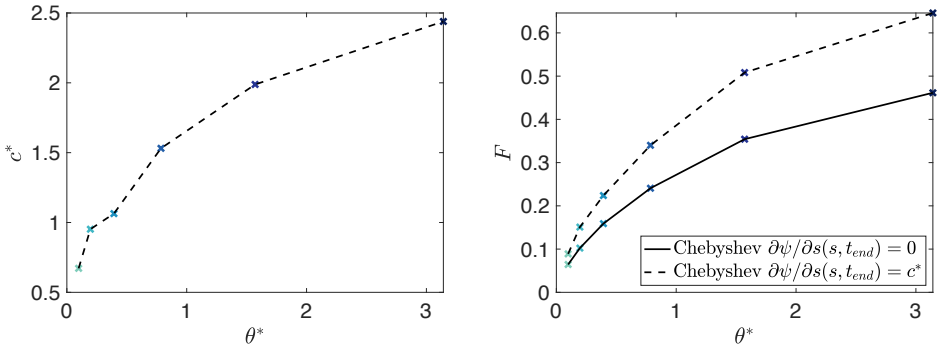

Figure 3.10: Chebyshev with $\partial\psi/\partial s(s, t_{end}) = c^*$: the constant-curvature to be returned to c^* as a function of θ^*, and the value of F for the optimal return-to-constant-curvature results. Surprisingly, these results incur a greater mechanical cost than the $\partial\psi/\partial s(s, t_{end}) = 0$ results, despite the fact that the high curvature Fourier $k = 0.1$ turns are more optimal than the Chebyshev shapes.

Approximation to travelling waves of constant curvature

The shape spaces of the optimal turning gaits so far have been high-dimensional, parametrised by a large number of modes and variables. Particularly for the Chebyshev waves, the control parameters in the optimisation routine are not easily interpretable. It would be useful to be able to investigate the qualitative behaviour of these optimal turns with easily-interpretable control parameters, or a simplified expression of ψ and a reduced shape space.

By examining the results for the optimal turns in this Chebyshev space (and also those for the $A_B = 10^{-2}$ Fourier case), we can see that there appears to be an almost travelling wave of constant curvature propagating along the length of the body from head to tail (fig. 3.11). This indicates that these optimal turns could in fact be approximated as precisely that: simply a travelling wave of constant curvature. We can reduce our shape space to exactly that, of shapes prescribed by a much smaller number of control parameters, that are also easy to interpret. This idea of using constant-curvature-travelling-wave approximations could also provide us with insight into the optimal turning results from the Fourier ψ.

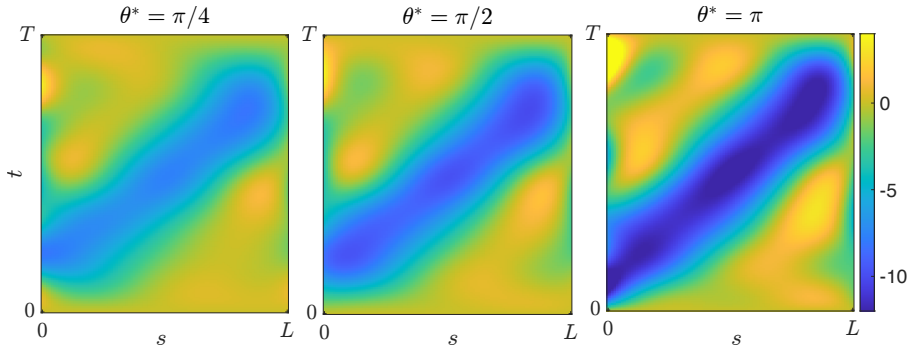

Figure 3.11: Curvature heatmaps of optimal Chebyshev turns for $A_B = 10^{-4}$, $\theta^* = \pi/8, \pi/2, \pi$. Observing the heatmap of the curvature for these three cases, there appears to be a near-constant travelling wave of curvature propagating along the body length in order to achieve the optimal turn.

3.3.3 Travelling waves of a single constant curvature

To further understand the results from the Fourier and Chebyshev shape space optimisations, we now substantially simplify our shape space to be only prescribed by a small number of parameters. In this section we investigate the cost of turning for simple travelling waves of constant curvature. These form a two-parameter family of wave shapes, and we can therefore easily visualise the entire energy landscape, to provide valuable insight into the resulting optimal turns.

We now consider prescribing the shape of the undulator via a travelling wave of constant curvature κ^* such that: at $t = 0$, $\partial\psi/\partial s(s, t = 0) = 0$, then as the waveform propagates from $s = 0$ down along the length of the body, a segment of length $l < L$ passes along the body, in which $\partial\psi/\partial s = \kappa^*$. Following this segment, the body returns to zero curvature, resuming a final straight position.

Let $\xi = s - t$ for $s \in (0, L), t \in (0, T)$, with $T = L + l_0$ where l_0 is the dimensionless lengthscale: $l = l_0/L$. Then the travelling wave of constant curvature is given by

$$\frac{\partial\psi}{\partial s}(\xi) = \begin{cases} \kappa^*, & \xi \in (-l_0, 0) \\ 0, & \text{otherwise} \end{cases} \tag{3.43}$$

Hence, the curvature prescribed is a periodic square wave, with period $T = L(1 + l)$. As an example, if $l = 0.5$, $\kappa^* = 10$, the resulting travelling wave of constant curvature yields a turning angle of $|\theta^*| \approx 9\pi/10$ (see fig. 3.12). The problem is now reduced to optimising over only these two parameters: l and κ^*. Explicitly, we again fix $r_k = 1/2$, and seek the optimal constant-curvature wave turns for the two values of A_B selected previously, and for the same set of θ^* as previous.

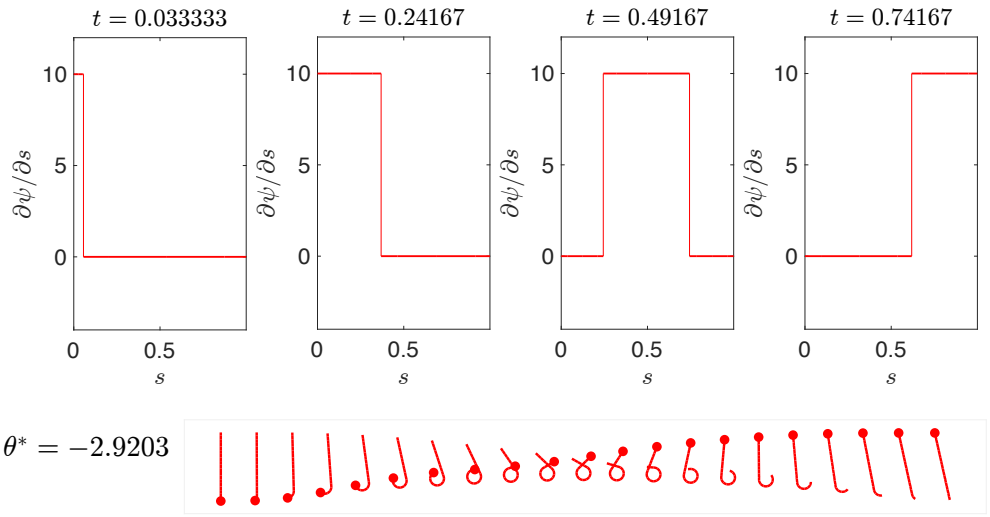

Figure 3.12: Example turning gait for constant curvature travelling wave, $l = 0.5$, $\kappa^* = 10$. A square wave prescribing the body curvature propagates down along the length of the body for $t \in (0, T)$.

Because we have now limited our shape space to that of only two parameters, we can perform a parameter sweep across both κ^* and l in order to visualise the complete energy landscape for the optimisation problem. For a range of κ^* and l, we can evaluate the cost function F, and simultaneously determine the resulting rotation achieved by each pair of parameter values, ie the turning angle θ^*. Obtaining the contours of constant turning angle in the landscape, for a given θ^* the optimal turn is the point along the contour at which F is minimised.

The optimal constant curvature wave turns are shown in fig. 3.13 ($A_B = 10^{-2}$) and fig. 3.14 ($A_B = 10^{-4}$). The results for $A_B = 10^{-2}$ qualitatively agree with the analogous results for the Chebyshev shape space. Moreover, the value of F also agrees fairly consistently as θ^* increases, though the Chebyshev results remain less costly, ie more optimal.

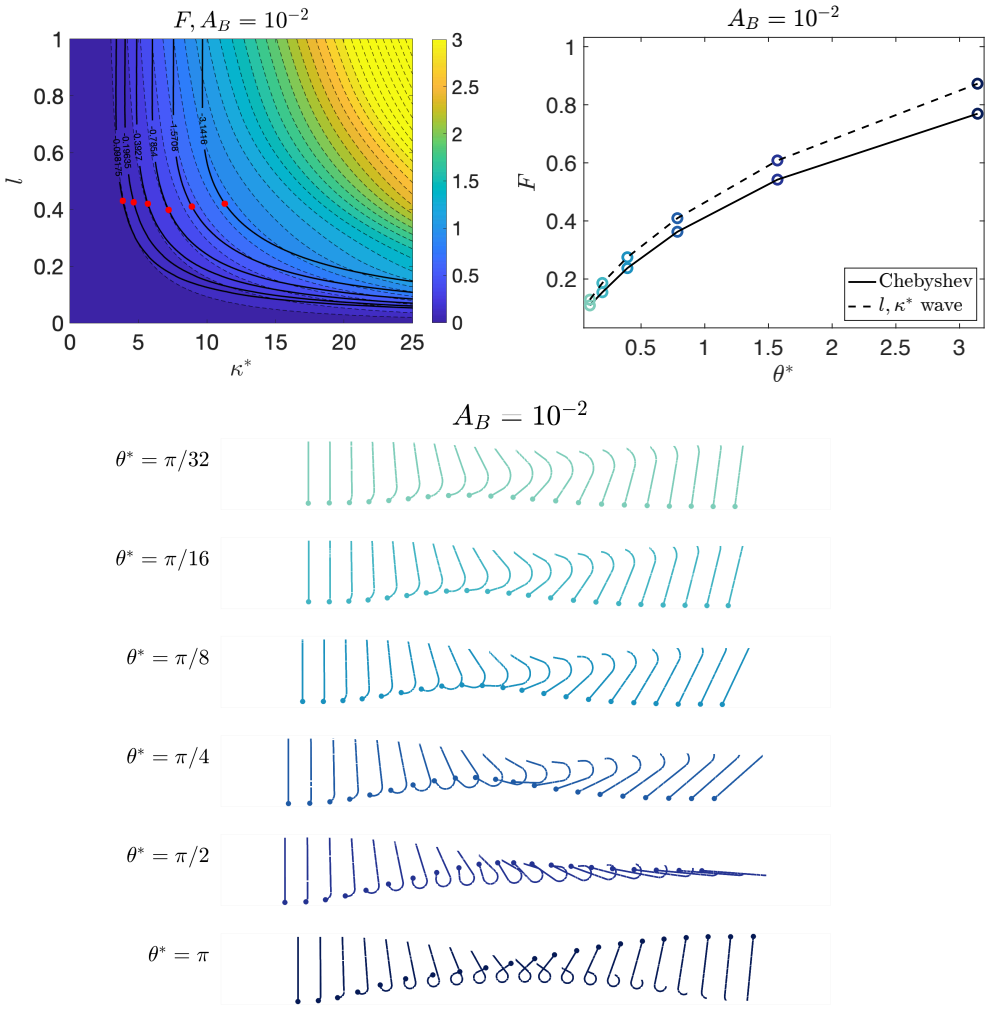

Figure 3.13: Optimal l, κ^* travelling waves of constant curvature turns for $A_B = 10^{-2}$. A parameter sweep over l, κ^* yields the optimal turn for a given θ^* as the point along the contour of constant turning angle that minimises F (red points). These turns closely approximate those for the Chebyshev shape space.

The results for $A_B = 10^{-4}$ yield a more interesting energy landscape from the parameter sweep. Here we observe some local optima for high values of κ^* at certain l. These wells of local optima in fact correspond to cases where the swimmer assumes a travelling wave of constant curvature shape that results in a perfect circle of exactly one circumferences propagating along its length, ie a perfect wheel rotational along the otherwise straight body. This configuration incurs a minimised rate of mechanical work compared with shapes of the same κ^* for different l, as there is hydrodynamical advantage to being completely straight if only for a wheel propagating along your length. Hence, these local optima arise for the $A_B = 10^{-4}$ case. These wells are not seen when $A_B = 10^{-2}$ as the bending costs dominate the cost due to viscous dissipation.

Furthermore, the optimal constant curvature wave turns for $A_B = 10^{-4}$ incur an interesting trend as θ^* increases. For higher turning angles, the optimal constant-curvature wave turn is achieved by assuming an increasingly high curvature, across an increasingly small length of the body. The points along the contours of constant turning angle for which F is minimised gravitate increasingly towards the lower right corner of the landscape. These turns also emerge as more optimal than those for the analogous Chebyshev case. This is an interesting result, as the Chebyshev shape space is much more general compared to this simple two-parameter family of shapes.

Plotting the values of the cost function F for a given κ^* as a function of l, and also for a given l as a function of κ^* (see fig. 3.15) we again see the local optima arise, in particular for high κ^* and high l. Below a certain threshold, the presence of such local optima ceases. For small enough l, a higher cost is always incurred as κ^* increases (F is monotonically increasing with κ^* when the length is small). The same is true for small enough κ^*. We observe that when $\kappa^* \leq 10$ (which is a regime applicable to real biological swimmers), the cost F is always increasing and l increases. The gradient of the function varies, and in particular for very small κ^*, the function becomes almost flat as $l \to 1$. This implies that there is little

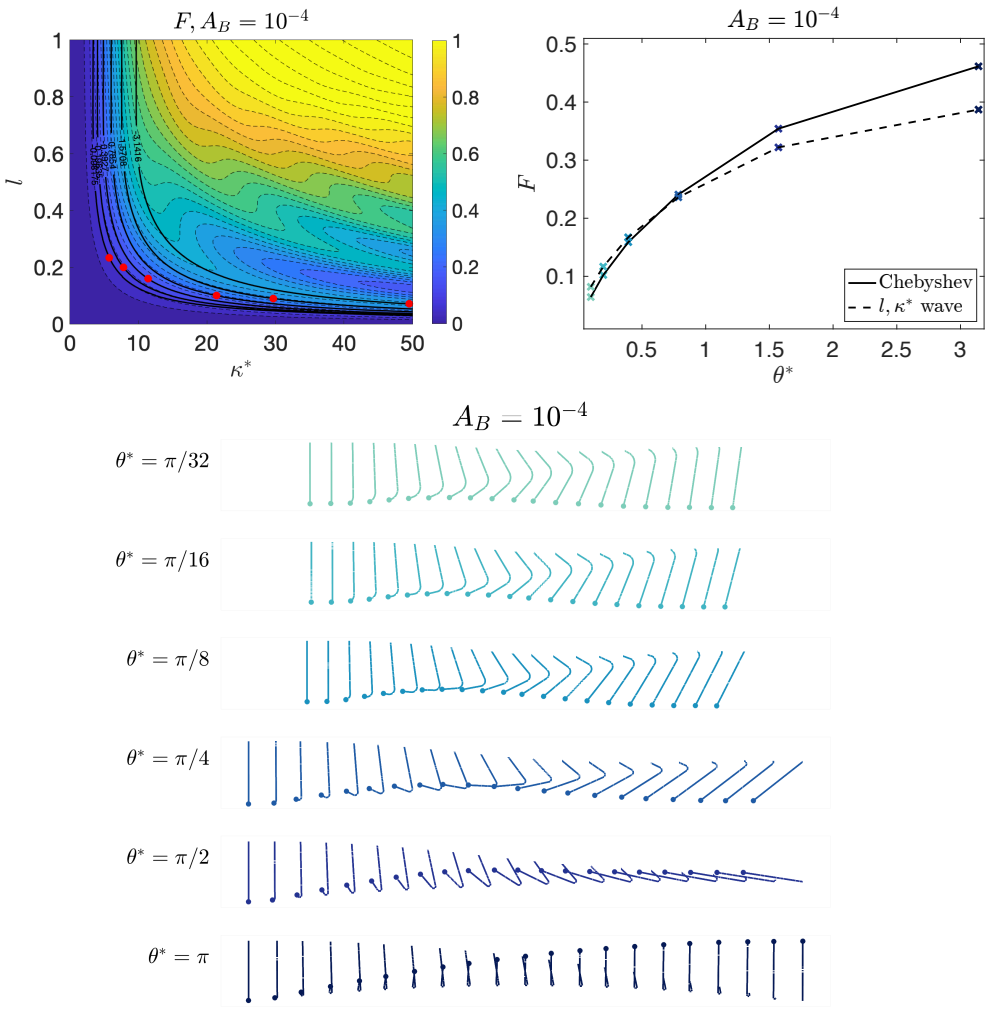

Figure 3.14: Optimal l–κ^* travelling waves of constant curvature turns for $A_B = 10^{-4}$. The resulting energy landscape that a parameter sweep over l, κ^* yields contains local optima in the bottom right, for low l and high κ^*. These local optima arise when the swimmer assumes a travelling wave of constant curvature shape that results in a perfect circle of exactly one circumference propagating along it's length. The results for these constant curvature turns for this A_B are more optimal than those for the analogous Chebyshev case.

difference in mechanical cost between curling up say only half of the bodylength and curling up completely (assuming uniform curvature over the entire length of the body). At least, in this low-curvature regime.

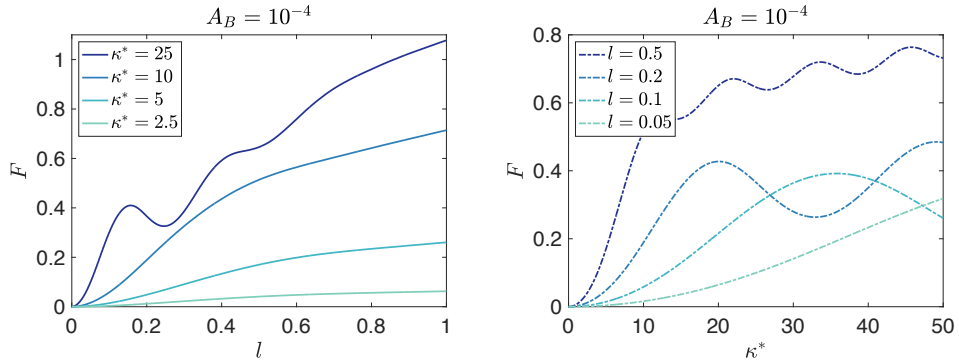

Figure 3.15: The cost function F as a function of l for a given κ^*, and as a function of κ^* for a given l. The presence of local optima ceases below a certain threshold.

Approximating constant curvature square waves with Chebyshev functions

For the l–κ^* waves, we have seen that when the cost is mostly bending ($A_B = 10^{-2}$) the optimal turns closely approximate those for the Chebyshev shape space, both visually and in terms of cost F. However, when the cost is mostly hydrodynamics ($A_B = 10^{-4}$), as θ^* increases the optimal turn is achieved by assuming increasingly higher curvature over a shorter section of the body. And for higher turning angles, the optimal constant-curvature wave turn is actually less costly than the equivalent Chebyshev wave turn, which is a much more general shape space.

We can investigate this interesting result by using an approximation to the constant curvature waves via Chebyshev expansions. The travelling waves of constant curvature that prescribe the shape space above are discontinuous Heaviside-like functions, which can be approximated by a truncated series of Chebyshev polynomials. We can therefore use the Chebfun software system [58] to obtain the Chebyshev polynomial approximation to these discontinuous, constant-curvature travelling waves. Furthermore, we can control the truncation of the series to investigate how the approximation of the square wave is affected by the degree of Chebyshev polynomial included. Of course, a better approximation is achieved when the series is truncated at a higher polynomial degree.

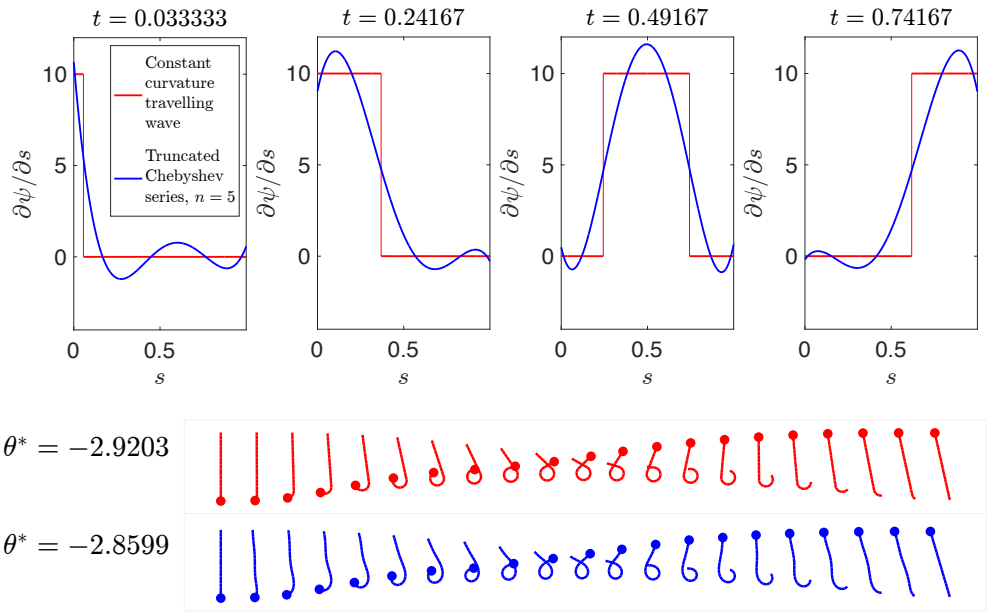

Figure 3.16: Truncated Chebyshev series ($n = 5$), which approximates the travelling wave of constant curvature given by $l = 0.5$, $\kappa^* = 10$. As t increases from 0, the travelling wave of constant curvature propagates from left to right: from $s = 0$ to L. At each t, the Chebyshev series approximation (truncated at $n = 5$ polynomials) attempts to best fit the square wave by adapting the coefficients of the polynomials.

With our l–κ^* wave example shown previously, for $l = 0.5$, $\kappa^* = 10$ the Chebyshev series approximating the travelling wave of constant curvature is shown in fig. 3.16, truncated at the $n = 5$ polynomial. The Chebyshev approximation reasonably captures the travelling square wave, and the resulting turning gait as prescribed by this Chebyshev approximation qualitatively matches that of the constant curvature turn. The most notable difference is, of course, the increased 'wiggly-ness' in the Chebyshev approximation turn, due to the variation in body curvature.

Similarly, applying the Chebfun approximation to the optimal constant curvature wave for $A_B = 10^{-2}, \theta^* = \pi$ (for which the optimal parameter values are $l = 0.4235, \kappa^* = 11.2502$), the Chebyshev series and resulting turning gait fairly closely align with the travelling constant curvature wave and associated turn (see fig. 3.17). Furthermore, the costs associated with the constant-curvature turn and

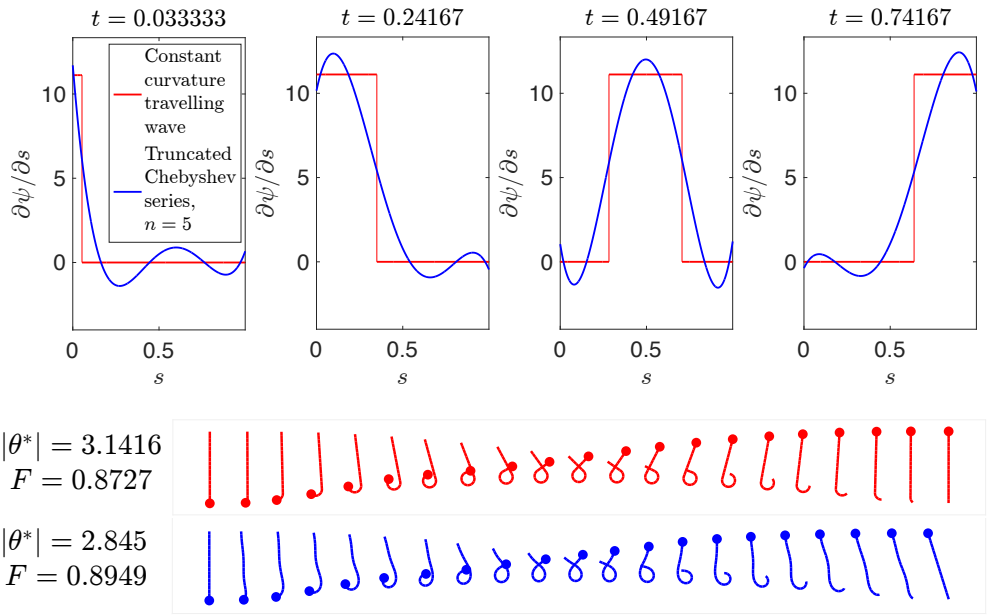

Figure 3.17: Truncated Chebyshev series approximate (at the $n = 5$th polynomial) for the optimal l–κ^* turn with $A_B = 10^{-2}, \theta^* = \pi$. The series approximation reasonably captures the constant curvature travelling wave, with comparable costs F, but does not quite yield a turn of π.

the Chebfun approximation are also similar: 0.8727 and 0.89485 respectively. That being said, the approximation does not actually achieve a turning angle of $\theta^* = \pi$, whilst incurring a marginally greater cost.

Applying the Chebfun approximation to the optimal constant curvature turn for $A_B = 10^{-4}, \theta^* = \pi$ is a different story. From fig. 3.18 we can see that, the 5th degree Chebyshev polynomial expansion cannot actually capture the high-constant-curvature across the small-lengthscale shape. The peak of the travelling square wave is so sharp that the Chebyshev series cannot recreate this turning behaviour, both qualitatively and quantitatively – we see that the turning angle achieved by this 5th degree approximation to the π turn is not much more than $\pi/2$.

However, if the Chebyshev series expansion were truncated at a higher n to include higher degrees of polynomials, the approximation can in fact appropriately capture the sharp-peaked square travelling wave, as we see in fig. 3.19. Increasing the expansion to include Chebyshev polynomials up to degree $n = 50$ results

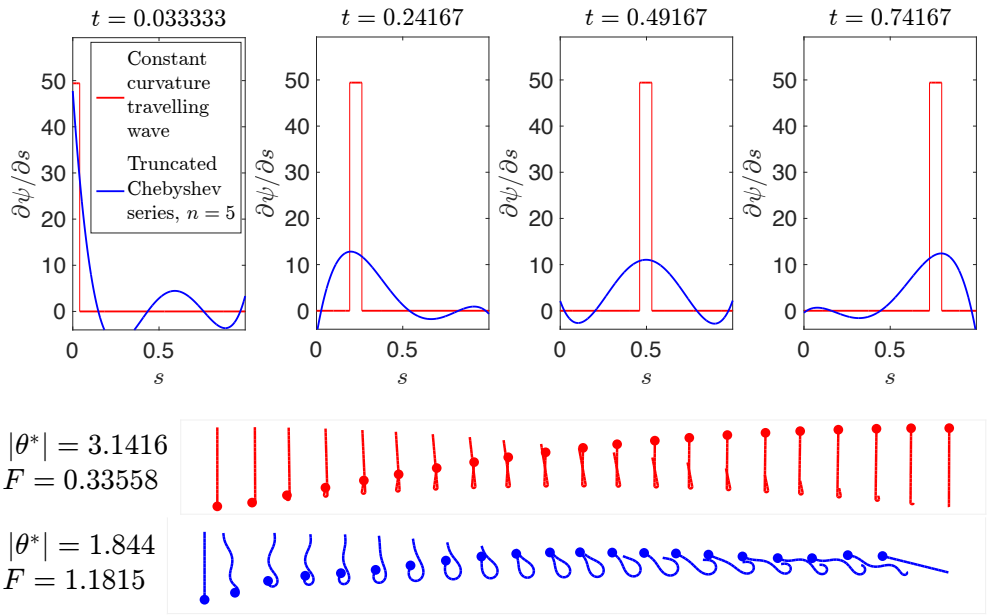

Figure 3.18: Truncated Chebyshev series approximate (at the $n = 5$th polynomial) for the optimal l–κ^* turn with $A_B = 10^{-4}, \theta^* = \pi$. For this case, the series is truncated at too few polynomials to sufficiently capture the sharpness of the travelling square wave.

in the series approximation closely capturing the high curvature shape, with resulting $\theta^* = 3.1575$ — significantly closer to the π turn we are approximating.

Recall that from our results for the Chebyshev wave turns (section 3.3.2), we prescribe the shape of the body with a finite double-sum over m^* modes in t and n^* modes in s, which are nth degree Chebyshev polynomials. In our finite sum, we set the number of polynomials $n^* = 5$.

The fact that for this Chebyshev series approximation (to the l–κ^* wave) truncated at $n = 5$ closely approximates our constant curvature wave when $A_B = 10^{-2}$ — which itself is close to the Chebyshev wave that it was devised to approximate — but does not closely approximate the constant curvature wave for $A_B = 10^{-4}$ gives us key insight as to why the Chebyshev waves look near identical between the two different values of A_B tested.

For $A_B = 10^{-2}$, because bending is penalised significantly in the cost function, high curvature shapes are avoided. Hence, high-degree Chebyshev polynomials

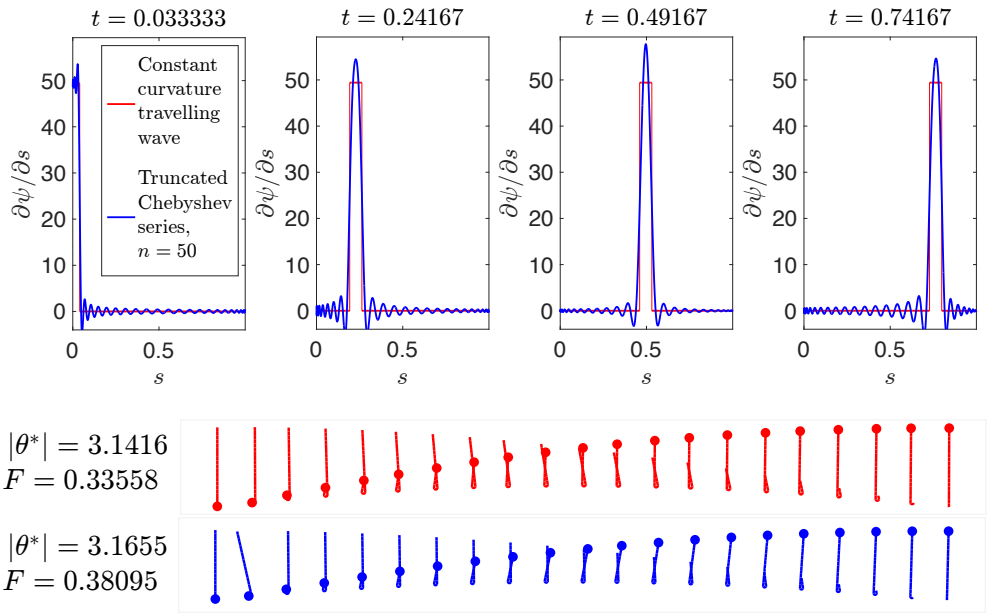

Figure 3.19: Truncated Chebyshev series approximate (at the $n = 50$th polynomial) for the optimal l–κ^* turn with $A_B = 10^{-4}, \theta^* = \pi$.

are not needed, and so $n^* = 5$ is sufficient for this bending cost. However, when $A_B = 10^{-4}$, we are allowing for higher curvature shapes, and in fact (given the constant-curvature wave analysis) we have found that when bending isn't penalised it is optimal to assume a very high curvature over a short segment of the body in order to perform the turn. The $n = 50$th degree Chebyshev polynomial series approximation does effectively capture this very sharp travelling square wave, and the resulting turning gait closely matches the constant-curvature turn. This suggests that significantly increasing n^* in our Chebyshev waves turns would result in the $A_B = 10^{-4}$ actually looking different from the 10^{-2} ones, adopting the higher-curvature shapes that the increased number of polynomials would allow. However, increasing n^* so drastically would have computational implications and the number of control parameters would significantly slow the numerical optimisation routine.

3.3.4 Travelling waves of two constant curvatures

Whilst useful in providing insight into the Chebyshev optimal turn results, the previous travelling-waves-of-constant-curvature turns clearly do not integrate to zero-curvature over one period. Recall that at the beginning of this chapter it was discussed that it is important to have constraints on the curvature in the context of optimal turning. The Chebyshev turns, and the previous travelling waves of constant curvature incorporate this constraint by enforcing (by construction or otherwise imposed in the optimisation) that the body start and end in a straight posture.

The Fourier waves did not have to start and end in a straight posture, as the constraint was included via the fact that the body curvature integrated to zero over one period of the wave:

$$\int_0^{1/k} \frac{\partial \psi}{\partial s} \, \mathrm{d}t = 0. \tag{3.44}$$

We now investigate the case of imposing this constraint on the curvature in the context of travelling constant-curvature waves. In particular, this approach could provide us with insight into the Fourier low wavenumber ($k = 0.1$) optimal turns, which were found to be the least costly.

The integrating to zero-curvature over one period is not going to be satisfied for a single constant curvature over some portion of the bodylength, with zero curvature otherwise (ie the l, κ^* waves). The second curvature would have to be non-zero to cancel out the total curvature contribution from the first.

Hence, we now construct a travelling wave of constant curvature with two curvatures κ_1, κ_2 over lengths l_1, l_2 respectively. For $\xi = s - t$, the shape of the wave is

prescribed via the curvature as

$$\frac{\partial \psi}{\partial s}(\xi) = \begin{cases} \kappa_1, & 0 < \xi < l_1 \\ \kappa_2, & -l_2 < \xi < 0 \\ \kappa_1, & \xi < -l_2 \end{cases} \tag{3.45}$$

and to preserve symmetry, l_1 is bounded by the length of the body: $l_1 \geq L$. If $l_1 < L$, this would result in initial and final cane-like body shapes.

To ensure zero-curvature over one period $T = 1/k$, we require that:

$$l_1 + l_2 = \frac{1}{k}, \tag{3.46}$$

$$\kappa_1 l_1 + \kappa_2 l_2 = 0. \tag{3.47}$$

Hence

$$\int_0^T \frac{\partial \psi}{\partial s} \mathrm{d}t = \int_0^{l_1} \frac{\partial \psi}{\partial s} \mathrm{d}t + \int_{l_1}^{1/k} \frac{\partial \psi}{\partial s} \mathrm{d}t \tag{3.48}$$

$$= \kappa_1 l_1 + \kappa_2 l_2 \tag{3.49}$$

$$= 0, \tag{3.50}$$

thus the requirement that the curvature integrates to zero is satisfied by eqs. (3.46) and (3.47). Furthermore, from these equations we see that we can prescribe only l_1 and κ_1, and determine l_2 and κ_2 by simple rearrangement:

$$l_2 = \frac{1}{k} - l_1, \tag{3.51}$$

$$\kappa_2 = \frac{l_1 \kappa_1}{l_1 - 1/k}. \tag{3.52}$$

Hence, this parameterisation also forms a 2-parameter family of shapes. Again, we may perform a parameter sweep over these two values l_1, κ_1 to fully visualise the energy landscape.

$k = 0.1,$
$l_1 = 4, \kappa_1 = 5$
$\theta^* = -0.361$

$k = 0.1,$
$l_1 = 6, \kappa_1 = -10/3$
$\theta^* = -0.361$

Figure 3.20: Example l_1, κ_1 constant curvature waves. The symmetry in this shape space is demonstrated here by the two different pairs of values the result in the same turn being prescribed.

To investigate the $k = 0.1$ Fourier results, we test this parametrisation of the shape space with the same fixed value of k. There is, by construction of this shape space, some symmetry. If the values of l_1, κ_1 are interchanged with the symmetric values for l_2, κ_2, the same constant curvature wave would be propagated for the same period, there would simply be an offset in the square wave. For example for $k = 0.1$, $l_1 = 6, \kappa_1 = -10/3$ is the same wave as $l_1 = 4, \kappa_1 = 5$ (see fig. 3.20). Due to this symmetry, it is therefore only required to perform a parameter sweep for $l_1 \in [1/2k, 1/k]$.

We perform a sweep over the energy landscape which prescribes this two-parameter family of constant curvature waves. The optimal turn is found by seeking the point along the contour of constant θ^* which has the minimal cost F. The results are shown in fig. 3.21 and fig. 3.22 for $A_B = 10^{-2}$ and 10^{-4} respectively.

For $A_B = 10^{-2}$ (fig. 3.21), the contours of constant turning angle θ^* incur the lowest undulatory cost F when l_1 is high (close to $1/k$), and κ_1 is small. Zooming in on the part of the energy landscape, we can see in fig. 3.21 that for increasing turning angle, the optimal κ_1 steadily increases with θ^*, whilst l_1 remains relatively constant — approximately 9.4–9.6. Comparing these results with those of the Fourier $k = 0.1$ waves, visually they appear extremely similar. It is therefore unsurprising that they incur the same trend and comparable costs F over the different turning angles.

For $A_B = 10^{-4}$ (fig. 3.22), in the energy landscape of this parameter sweep we can

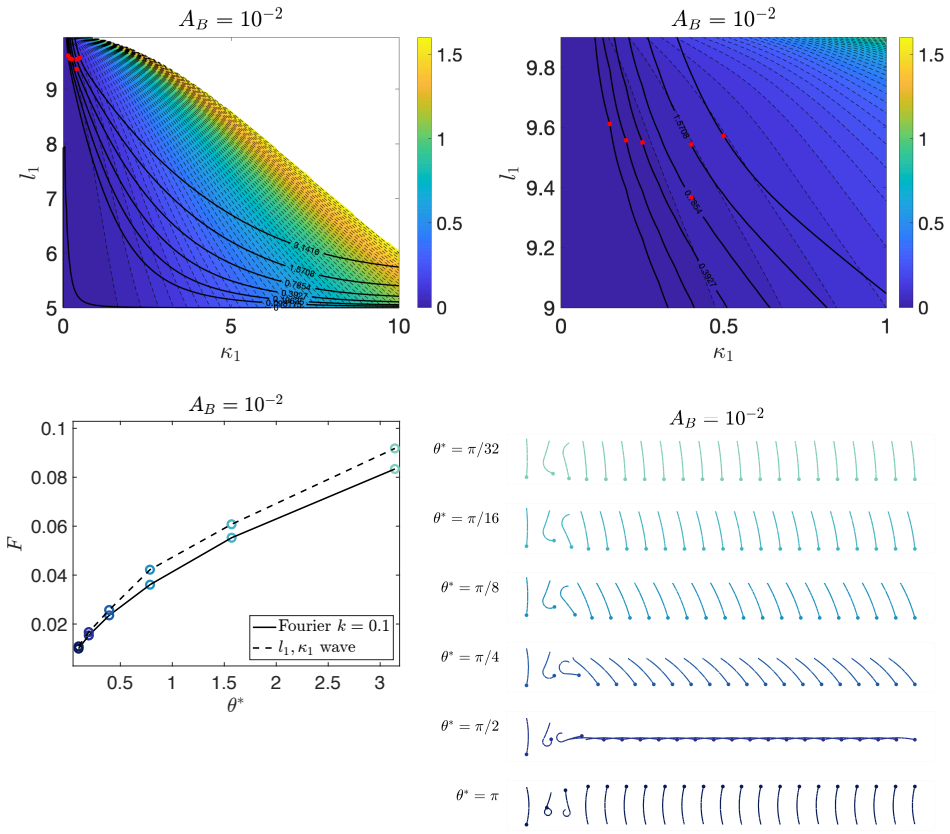

Figure 3.21: Optimal l_1, κ_1 travelling waves of constant curvature turns for wavenumber $k = 0.1$, and $A_B = 10^{-2}$. A parameter sweep over l_1, κ_1 yields the optimal turn for a given θ^* as the point along the contour of constant turning angle that minimises F (red points). Zooming in on the upper left corner of the landscape, we observe that for increasing θ^*, the optimal κ_1 increases whilst l_1 remains relatively consistent. These constant curvature waves qualitatively appear similar to the Fourier $k = 0.1$, and have comparable (though marginally higher) turning cost F.

observe, as we did for the l–κ^* waves, the existence of local optima due to the perfect-wheels-rotating-along-a-straight-body shapes that these combinations of l_1, κ_1 values prescribe, that are hydrodynamically less costly. As for $A_B = 10^{-2}$, the optimal turn is again achieved with high l_1 and low κ_1, in the upper left region of the landscape. Again, for increasing θ^* the optimal l_1 remains relatively constant (approximately 9.4), and κ_1 steadily increasing as the turning angle increases. Except from, notably, $\theta^* = \pi$, which does not follow the trend of increasing κ_1, and instead maintains a similar curvature as for the $\pi/4$ turn but for a larger

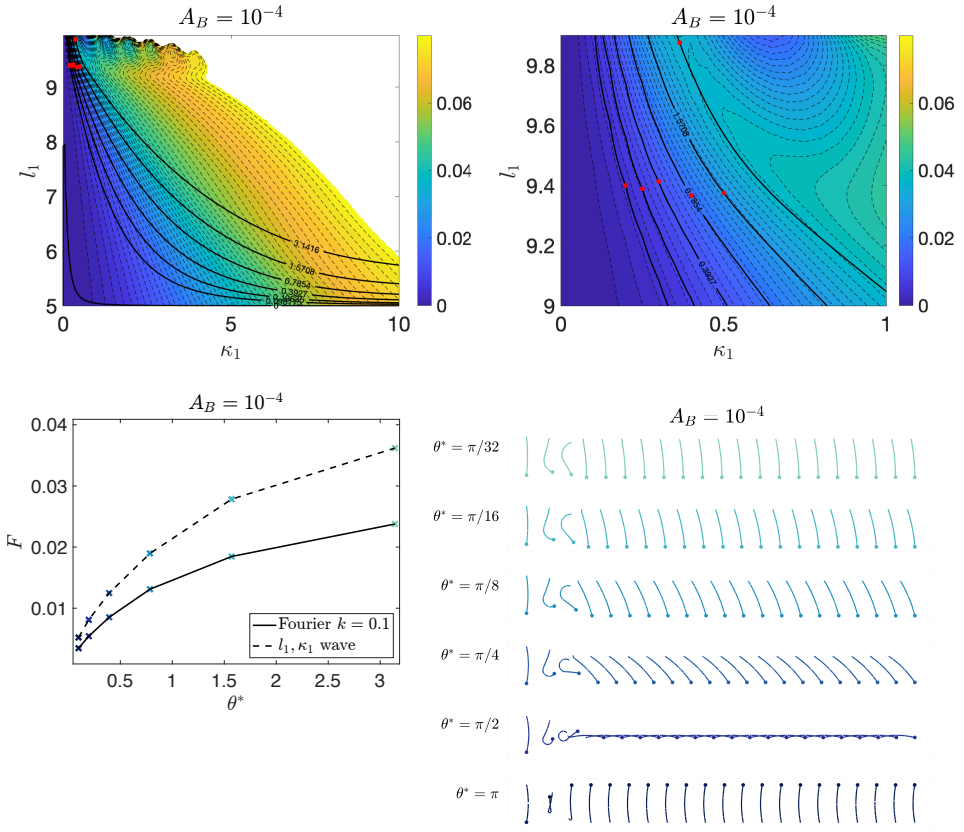

Figure 3.22: Optimal l_1, κ_1 travelling waves of constant curvature turns for wavenumber $k = 0.1$, and $A_B = 10^{-4}$. A parameter sweep over l_1, κ_1 yields the optimal turn for a given θ^* as the point along the contour of constant turning angle that minimises F (red points). Zooming in on the upper left corner of the landscape, we observe that the contours of constant θ^* appear parallel as l_1 approaches $1/k$. These constant curvature waves are less optimal (have higher cost F) than the Fourier waves of the same k.

segment, with l_1 notably increased. We can see by the contours of the landscape that the minimum F along the constant $\theta^* = \pi$ contour is approaching one of the aforementioned local optima. The incidence of these wells of locally low cost are certainly what appears to be influencing this shift in trend for the optimal π turn for this shape space.

As θ^* increases, the constant curvature wave turns here becoming decreasingly visually similar to the analogous Fourier $k = 0.1$ turns. Recall that the Fourier turns assumed much higher initial and ending curvatures along the body length.

It is therefore interesting to see that the Fourier $k = 0.1$ significantly outperform these constant curvature waves for $A_B = 10^{-4}$, in that they incur much lower cost.

To try and recreate the result for the Fourier $k = 0.1$, $\theta^* = \pi$ turn for $A_B = 10^{-4}$ with this parameter space, we can move down along the contour of $\theta^* = \pi$ in the landscape, to a pair of l_1, κ_1 that yield a visibly similar result to that of the Fourier wave. For example, fig. 3.23 shows the constant curvature turn for $l_1 = 8.1, \kappa_1 = 2.25$, which in initial and final position looks much more alike the Fourier turn in question (see fig. 3.5). This constant-curvature turn however incurs almost twice as high a cost F. This two-curvature shape in this wave obviously incurs a higher hydrodynamic cost than that of the actually optimal constant curvature wave (that has higher l_1, and lower κ_1). The s-shaped posture of the body for this wave contributes significantly to the dissipation cost. We can conclude, in this shape space at least, that it is optimal to reduce the curvature and increase the length scale.

These two-constant-curvature wave results (with κ_1, κ_2 over l_1, l_2 respectively) appear visually notably similar to the singular-constant-curvature wave results (κ^* over l, otherwise 0). From this we can conclude that, with such restrictions on the curvature in the body, it is optimal to assume almost (or entirely) straight postures for most of the period of the propagating wave, in order to minimise the cost function.

The restriction of only two constant curvatures is clearly an extremely minimal shape space. Such a shape space does not yield the Fourier travelling wave shape that is found to be optimal for the low wavenumber, low bending cost case.

$\theta^* = 3.1416$ 

Figure 3.23: Turning gait prescribed by $l_1 = 8.1, \kappa_1 = 2.25$. Visually, this shape aligns more closely with the Fourier $k = 0.1$ optimal turn for $\theta^* = \pi$, with initial and final posture, but is not the optimal in this shape space.

3.4 Conclusion

3.4.1 Summary

We have revisited the problem of optimal undulatory locomotion, in the context of low Reynolds number hydrodynamics, and extended previous approaches to consider rotations and manoeuvrability, in order to determine optimal undulatory turning gaits. The framework presented in chapter 2 was adapted from the case of straight-path forwards locomotion, to introduce path curvature for modelling turning. In our turning model framework, we construct the optimisation problem by choosing to impose the rotational constraint $\theta(T) = \theta(0) + \theta^*$ which requires the body to have performed a turn of size θ^* in one period of the waveform T, and minimise the cost (ie the objective function) associated with the motion.

We determined, with an analytical result and numerical confirmation, that the theoretically optimal way for an undulatory microswimmer to perform a turn – that minimises $F = (1 - A_B)\Phi + A_B\mathcal{P}_{\text{Bending}}$ — as the importance of bending cost is reduced ($A_B \to 0$), it is optimal to also reduce the radius of curvature R and assume a tightly-coiled high-curvature shape. Furthermore, the dependence of the optimal radius of curvature scales with the given relative importance in the cost function according to $A_B \sim R^4$. As a result, for small A_B the parametrisation of the shape space can be chosen to include some constraint on the curvature of the shapes. Otherwise, a constraint on the curvature must be explicitly imposed in the optimisation problem, along with the constraints required by the resistive force model, and of course the rotational constraint which is what allows us to model optimal turning.

Performing numerical optimisation, to investigate optimal undulatory turning gaits we chose to isolate two values of A_B to highlight categorical differences in optimal turning strategies when the cost function is mostly bending ($A_B = 10^{-2}$) versus mostly environmental ($A_B = 10^{-4}$). In order to determine the optimal turning

gait, the tangent angle $\psi(s,t)$ is decomposed onto a finite sum of a number of modes, the values of which are determined by the optimisation.

Our initial parametrisation of the shape space for $\psi(s,t)$ — the Fourier travelling waves — imposed the constraint on the curvature by construction: for this parametrisation the curvature integrates to zero over one period of the waveform. We then generalised the shape space to no longer limit the turns to only travelling waves. Decoupling space and time, our Chebyshev shape space — which parametrised the shape of the body via nth degree Chebyshev polynomials — required an additional constraint that $\partial\psi/\partial s(t=0)=0$ which, due to periodicity, ensured that the undulator start and end the turn in a straight posture.

In order to gain further insight into the results from the Fourier and Chebyshev parametrisations, we investigated approximations to the turns by prescribing the shape using only two parameters — some constant curvature κ^* over some length $l < L$. A benefit of this simple shape space is that the parameters are easily-interpretable, compared with the high-dimensional shape spaces of the Fourier and Chebyshev waves. The l–κ^* optimal turns captured similar turning behaviour as the Chebyshev waves (for the $A_B = 10^{-2}$ case), and using approximations to these square constant curvature waves of truncated Chebyshev polynomials series provided insight as to why the Chebyshev turns for the two different values of A_B we chose did not differ significantly. For $n^* = 5$ Chebyshev polynomials, the series approximation could not sufficiently capture the sharpness of the square wave that is optimal in the l–κ^* shape space for $A_B = 10^{-4}$. Significantly increasing the number of polynomials (eg $n^* = 50$) did lead to a close approximation of the constant curvature wave, indicating that increasing n^* in the optimisation may yield differences between the 10^{-2} and 10^{-4} optimal turns. Overall, the results from the Chebyshev shape space would benefit from further investigation.

Turning back to the Fourier results, for which it was optimal to reduce the wavenumber k (ie extend the period $T = 1/k$ of the waveform), we sought to approximate

these with constant-curvature waves via a travelling wave of two constant curvatures κ_1, κ_2 over two length scales l_1, l_2, with the imposition that this shape space satisfied the same constraint on the curvature as the Fourier space — that it integrates to zero over one period. With $k = 0.1$, we obtained these optimal constant curvature turns in this second low-dimensional shape space, finding that the results did not vary drastically from those of the l–κ^* turns.

Overall, we found that the nature of the optimal turning gait for the low Reynolds number undulatory swimmer depends fundamentally on the relative importance of bending versus hydrodynamical cost in the objective function. When the cost function is mostly bending ($A_B = 10^{-2}$), the Chebyshev waves yielded the most optimal turns out of the parametrisations we considered. These Chebyshev turns are however closely approximated as travelling waves of constant curvature (as seen in (fig. 3.13)). When the cost function is mostly hydrodynamics ($A_B = 10^{-4}$), from the parametrisations we have considered the least costly turn is given by the Fourier travelling waves when the wavenumber k is minimised, and the nature of these optimal turns was not captured by either constant-curvature wave approximation.

3.4.2 Further considerations

There are many further considerations that could be made to extend our approaches and analysis carried out here to continue the investigation of optimal undulatory turning gaits. The optimal turning gait results presented here are from the basis of theoretical and analytical results from low Reynolds number hydrodynamics. Scientific models predominantly are used to understand, define, or quantify particular parts or features of the world. They are constructed to attempt to describe observable phenomena. To this point, it would be valuable to inform our model with biological data, and apply our framework to microscopic undulatory turns observed in nature, to further our understanding of this particular

mode of motion of these kinds of organisms.

Possible extensions or adaptations to our presented model include: imposing a penalty for overlapping and self-intersection (since in reality there are non-trivial mechanical forces associated with the undulator's body crossing over itself), devising an expression of hydrodynamic efficiency for turning by considering the ratio of mechanical work required for the undulator to turn θ^* to the rate of working required by an external force to rotate the undulator by θ^* (as discussed in section 3.1.1), and hence changing the objective function and posing an alternative optimisation problem which maximises hydrodynamic efficiency for turning, as opposed to minimising the associated cost for performing a turn.

It is not intuitive as to how the turning angle would inform the optimal gait if this approach were considered. The result of this hypothetical optimisation problem may point to an optimal turning angle which is the preferred angle of reorientation for these undulatory microorganisms. However, there is of course no globally preferred angle of reorientation — the desired turning amount is context-specific, and depends on, for example, if an organism is simply exploring its surroundings (in which case shallow, small θ^* turns may be preferred) versus escaping an averse stimulus (we hypothesise that, when encountering a predator, a turn of $\theta^* = \pi$ is the most optimal). The mathematical analysis for the question of maximising a hydrodynamic efficiency for turning in particular requires further consideration.

Regarding the results presented in this chapter, further quantitative analysis of how the number of Chebyshev polynomials included in the shape space affects the nature of the resulting optimal turns could provide more insight into these results. Whilst it may be beneficial to drastically increase n^* to test if high curvature shapes are optimal in this parametrisation for low bending cost, the computational limits of the numerical optimisation routine in its current form do not allow for such a large number of control parameters to be included without compromising algorithm performance.

Of course, the advantage of prescribing the shape space as a function of only two variables, as was done for the constant-curvature waves, obviously yields a very small set of control parameters in the optimisation routine. Hence, computationally the limits of exploring this shape space are minimal. Given this, it could provide further insight to investigate these kinds of shape spaces further. In particular, using the second type of constant curvature waves considered (with two curvatures κ_1, κ_2 over two lengths l_1, l_2) to investigate the Fourier wave results for other values of the wavenumber k could yield quantitatively interesting analysis and provide further insight.

Furthermore, recall that Lighthill (1975) [9] postulated, after deriving his sawtooth result, that the true biologically optimum shape (for the straight-path context) would be to alternate between diagonal straight segments and rounded corners of circular arcs — the radius of which would be subject to the individual's achievable radius of curvature. This supposition was realised by Spagnolie and Lauga (2010) [12], when obtaining the optimal gaits for multiple values of $A_B \in [10^{-7}, 1]$. Hence, this determined optimal straight-path undulatory gait is in fact almost a travelling wave of constant curvature. The straight segments have zero-curvature, and the 'rounded corners' are circular arcs also with constant curvature. The parallel that, by our findings, the optimal undulatory turn is achieved by approximately assuming a travelling wave of constant curvature (for the $A_B = 10^{-2}$ case) echoes the straight-path results from the literature, and further investigation could lend more insight into optimal undulatory gaits as a whole.

End of Part I

Part II

Chapter 4

C. elegans locomotion optimality

4.1 Introduction

In this chapter we lay out the framework for developing efficiency as a phenotyping lens in order to quantify *C. elegans* gait optimality. We begin with a brief introduction to the organism *Caenorhabditis elegans*, in particular its status as a model organism for small-scale undulatory locomotion, and discuss previous studies on how and why it moves the way it does. The answers to these questions lie in the realms of biomechanics, hydrodynamical models, studies of its neural circuitry, and genetic factors. Beyond these, further important factors that may affect *C. elegans* movement include its ecology, development, biochemistry, and ethology. There are considerations across many branches of biology that can be made to address this complicated question. Whilst the scope of this question spans many avenues of biological research, in this thesis we focus specifically on *C. elegans*' gait efficiency.

The experimental and computational methods for applying efficiency as a phenotyping tool in *C. elegans* behavioural screening are described. Specifically, we address the question "can efficiency as a *C. elegans* phenotype yield quantitative

differences between individuals in a behavioural screening?" for the particular context of rare human genetic disease models. For a number of *C. elegans* mutant strains, each with a rare human genetic disease association, we determine the efficiency of its locomotion along with other behavioural features, and analyse the results.

Rare genetic diseases in humans can be modelled in *C. elegans* with disease-associated genetic variants of conserved genes. Such disease models exhibit locomotion changes compared with wildtype 'healthy' worms, and these changes are often quantified in behavioural phenotypic screens. Expanding the set of current quantitative phenotypes to include more orthogonal behavioural features is valuable to pursue, so that more movement defects can be detected.

In this chapter we examine if gait efficiency as a phenotype may be useful for distinguishing mutant strains from wildtype. This can be tested by looking at strong genetic perturbations, and genes where disruption causes severe disease in humans might be expected to be strong perturbations. We therefore consider such human genetic disease model strains, testing efficiency as a phenotyping lens. Furthermore, efficiency is not completely defined by speed: two different gaits that have equal speeds could have different efficiencies. It could therefore be the case that efficiency contains different or independent information from other motility measures alone.

Structure and contributions of this chapter

This chapter explores the development and application of gait efficiency as a phenotyping tool for *C. elegans* behavioural screens. We begin with a review of related studies and results from the literature before describing the approach taken (employing tools from low Reynolds number hydrodynamics) for developing efficiency as a quantitative behavioural phenotype. The phenotyping lens is applied to *C. elegans* rare human genetic disease models — a recently-obtained dataset

in the Behavioural Phenomics lab (unpublished at the time of submission of this thesis). This data was collected using advanced imaging systems, with arrays of high resolution cameras so that many worms can be recorded in parallel. Experimental (wet lab) work was carried out by Ida Barlow and Tom O'Brien. Video data processing of the mutant *C. elegans* strains was performed using the using the Tierpsy Tracker software [10, 11]. Per-well feature extraction and gait optimality features were obtained with computational pipelines constructed by Madeleine Hall in the MATLAB programming platform.

This chapter, whilst related to chapter 3 through the themes of low Reynolds number hydrodynamics and optimality, addresses an entirely separate question and comprises an entirely separate set of results. Whilst still exploring the general question of optimal micro-undulatory locomotion, this chapter has no specific focus on turning strategies, as this is a more complicated problem than general *C. elegans* locomotion. It would be a worthwhile future extension to consider different movement strategies, separating turning from other modes of locomotion, to extend the phenotyping tool. The work in this chapter is a first step in developing this specific phenotyping lens of efficiency, and we thus consider overall displacement, and not simply isolating just worm turns.

The results of applying the efficiency phenotyping lens in the rare human genetic disease models context are discussed and analysed. In the results section we explore the applicability of efficiency as a tool for detecting *C. elegans* behavioural differences. We find that efficiency, whilst related to other behavioural features and summary metrics, complements and contributes to the pre-existing set. Efficiency provides not only a quantitative measure of behaviour but also an interpretable one. It possesses intuitive meaning, and is not simply captured by for example only speed or curvature, but encompasses a combination of these quantities amongst others. The overarching motivation behind this chapter is that we are striving to find new interpretable features that are distinct from pre-existing ones and contribute to the broader understanding of *C. elegans* behaviour.

4.2 Background and context

The animal *Caenorhabditis elegans* is so named from the Greek *caeno-* (recent), *rhabditis-* (rod-like), and the Latin *elegans* (elegant). It is a microscopic worm (an adult typically measures approximately 1mm in length), and is in the phylum nematoda. Since its use first pioneered by Sydney Brenner in the 1960s [59], it has become a popular model organism used to study a wide range of phenomena across a breadth of scientific disciplines. It was the first multicellular organism to have its entire genome completely sequenced [60], and through forward and reverse genetics, many key genes in developmental and cell biology have been identified. This organism offers a valuable opportunity to connect studies on the physics of behaviour with genetics and neuroscience.

Since its popularisation, this small but mighty model organism has provided a platform for performing cutting-edge scientific research across many branches of biology. To name just a few examples: for everything from studying age-associated mitochondrial damage (Shen *et al*, 2014 [61]), to cell-specific proteomics (Yuet *et al*, 2015 [62]), to frontiers in embryogenesis (Packer *et al*, 2019 [63]). Specifically pertaining to the study of behaviour and genetics in neuroscience, in recent years the contribution of *C. elegans* neurogenetics research has included furthering the understanding of many neurodegenerative diseases, including but not limited to ALS, Alzheimer's Disease, Parkinson's Disease, and Huntington's Disease (Liang *et al*, 2020 [64]). The global community of worm researchers is empowered by extensive and continually-maintained databases and tools, such as WormBase (the central repository for the genetics and genomics of the nematode, Davis *et al*, 2022 [65]), OrthoList (a compendium of *C. elegans*-human orthologs, Kim *et al*, 2018 [66]), and WormAtlas (a database featuring behavioural and structural anatomy, Altun *et al*, 2021 [67]).

4.2.1 Modelling *C. elegans* undulatory locomotion

C. elegans provides a popular platform for studying undulatory locomotion. They are microscopic and thus can be kept in the lab on agar plates, where inertia is negligible for their locomotion, which simplifies mathematical analysis. Furthermore, their anatomical simplicity and their namesake elegant sinusoidal movement pattern inherently lends itself to mathematical analysis. Developing mathematical frameworks to describe this type of movement in a variety of contexts is an active area of research, and many models have been devised to further understanding of how these undulatory microorganisms traverse their surroundings.

The importance of external media

C. elegans moves by propagating undulatory waves along its body via alternating contraction and relaxation of dorsal and ventral body muscle. An early study of the locomotion of nematodes by Gray and Lissman (1964) observed that the form and frequency of the waves propagating down along the worms body depends on the nature of the external medium [15]. As well as *C. elegans*, other nematodes included in this study were *Panagrellus redivivus*, *Turbatrix aceti*, and *Haemonchus amtortus*. The nematodes were observed "gliding" or "creeping" (crawling): through a suspension of starch grains, on the surface of 1-2% agar or gelatine, and on a damp rigid surface. They also observed nematode swimming in aqueous media, which they determine to be a different mode of locomotion from the gliding (crawling) gait of the other media studied. They observe that the wavelength, frequency and wavespeed of the undulations propagating along the body are much less for creeping worms than for swimming, but that the ratio of amplitude to wavelength remains largely the same between creeping and swimming. Across the different media, the nematodes experience varying degrees of slip, which reportedly (and explained in Gray Hancock, 1955 [8]) depends on the ratio between the normal and tangential resistance coefficients. Since then,

numerous studies have been conducted to investigate the effects of external environments on *C. elegans* gaits [16, 32, 33, 68–77]. In the wild, *C. elegans* are commonly found living in rich soil or compost (where the species was originally isolated [78]), as well as on rotting fruits and stems [79]. The locomotion of *C. elegans* in soil-inspired media has been widely considered and investigated, and the question of the efficiency of its locomotion has been posed since early studies, as efficient locomotion is inherent to survival.

Early research by Wallace (1968) estimated the optimal soil particle diameter for maximum mobility (30–100 μm) — specifically that the optimal diameter increases with the worm length [16]. More recently, *C. elegans* locomotion has been studied in wet granular media [68], saturated particulate systems [69], as well as stuctured microfluidic environments [33, 70]. The presence of particles or obstacles is consistently found to significantly alter the worm's gait, often enabling locomotion of a greater distance per body undulation than in particle-free settings. This shows that stroke effectiveness is higher in some environments than others. As to whether nematodes are 'optimised' for certain modes of locomotion — there is likely a selective pressure on using the least possible amount of energy to achieve a locomotion goal, which will involve a combination of straight paths and curved paths (turns). The precise nature of the locomotion depends on many other things, which could range from information gathering, to robustness to perturbation, to predator avoidance.

These organisms are commonly studied in laboratory environments on surfaces very different from those of their natural habitat. *C. elegans* are frequently observed under the microscope crawling on agar gels or swimming in fluids, which respectively yield the adoption of visibly distinct gaits. Crawling gait is characterised by undulations with low frequency and short wavelength, whereas swimming gait is characterised by undulations with higher frequency and longer wavelength [32, 71]. Whilst *C. elegans* crawling versus swimming appears visibly very different, Berri *et al* (2009) found a smooth transition from swimming to crawling

gait in media with a tunable degree of viscoelasticity, establishing that forward locomotion is in fact achieved through modulation of a single gait [32]. Following this, Fang Yen *et al* (2010) [71] quantified internal viscoelastic properties of the worm, suggesting that its gait continuously adapts to external mechanical load in order to maintain propulsive thrust, which aligns with the single gait result from Berri *et al* (2009). In a related study, Snzitman *et al* (2010a) [72] also quantified internal properties of the nematode, finding that these properties are sensitive to changes in muscle functional properties. Later, Sznitman *et al* (2010b) [73] carried out detailed flow dynamics which found that *C. elegans* delivers propulsive thrusts on the order of a few nanonewtons, with results supported by values obtained using resistive force theory.

Further considerations of propulsion, and additional studies concerning viscoelastic media include Shen *et al* (2011) [75] who found that fluid elasticity hinders self-propulsion — reporting a 35% slower propulsion speed than for the compared Newtonian fluids. Following this, analysis of locomotion specifically on wet surfaces was carried out by Shen *et al* (2012) [74], using kinematic data and a hydrodynamic model based on lubrication theory. They calculated both the surface drag forces and the nematode's bending force while crawling on the surface of agar gels, finding that the normal and tangential surface drag coefficients during crawling are approximately 222 and 22 respectively, and the drag coefficient ratio is approximately 10 (the value applied later in the analysis and results of this chapter — see section 4.3.2). Beyond this, considerations of alternative scenarios and studying the effects of confinement on gait include studies by Lebois *et al* (2012) [76] and Bilbao *et al* (2013) [77]. Studies of the locomotion of this nematode have evidently spanned across a breadth of environments: from swimming in fluids (of varying degrees of viscosity or viscoelasticity), to crawling on wet surfaces or in granular media, to locomoting in confinement.

More recently, Cohen and Ranner (2017) [80] presented a biomechanical model of *C. elegans* locomotion alongside a novel finite element method that applies to

a range of environments. Their approach allows for the study of the dynamics of arbitrary undulation gaits and the link between the animal's material properties and its performance across a range of environments. Their model incorporates the collective passive viscoelasticity of the tissue, an active moment, and drag forces. The inclusion of these elements captures the interactions between the organism and its low Reynolds number environment. Many mathematical and computation models of *C. elegans* locomotion have been developed and studied over the years, some of which are discussed below.

Mathematical and computational models of *C. elegans* locomotion

As well as moving forwards, other locomotion modes *C. elegans* employs for navigation include reversing, turning and the well-known omega turn, in which the worm makes a sharp angle turn forming an Ω-shape with its body, as well as shallow turns, in which a gentler disruption of the forward locomotory gait is employed. Kim *et al* (2011) found that shallow turns are the most frequent reorientation strategy of *C. elegans* crawling on agar in the absence of food [53], and provide a theoretical model to extract a small set of parameters that characterised this motion. This specific model of *C. elegans* shallow turning is one of many theoretical and computational models of this organisms gait to have been developed in order to better understand its locomotion. Mathematical models of *C. elegans* general undulatory locomotion have been widely considered, frequently based on mechanics [81–84] — describing the frictional, hydrodynamical, elastic, and/or internal pressure forces — and often incorporating internal biophysical or neuronal components, such as mechanosensory feedback, muscle dynamics based on neural oscillations, and neuromuscular control systems [85–88].

Whilst some analysis has been performed specifically in three dimensions [89, 90], many of the proposed models of *C. elegans* locomotion capture only planar undulations. When swimming and crawling, *C. elegans* propels itself by planar

body undulations, and so models concerning the propagation of two-dimensional waves are effective in capturing many gaits exhibited by the organism. Gagnon and Montenegro-Johnson (2017) determine that neglecting out-of-plane effects during swimming through a shear-thinning fluid results in an overestimate of fluid viscosity, and therefore an overestimate of the power the swimming nematode expends [91]. However, overestimation of the power expended by assuming the two-dimensional (as opposed to the three-dimensional) shear-rate only lead to significant disagreements in fluids with effective viscosities higher than $\sim 10^2$ mPa s, which is higher than is relevant for *C. elegans* crawling on the surface of standard agar substrate. The *C. elegans* behavioural phenotypic screens carried out to obtain the data analysed in this chapter were done on 1.7% agar plates, which although non-Newtonian is essentially flow-independent at the relevant speeds, and which has a viscosity of approximately ~ 50 mPa s [92].

Resistive force theory models of *C. elegans* locomotion

In the particular case of modelling swimming worms, low Reynolds number hydrodynamical models are used for computing the flow of the surrounding fluid, and hence the computation of the worm's translation and velocity. The undulatory locomotion can be modelled by resistive force theory of Gray and Hancock (1955) [8]. This approach has been used widely and effectively for both modelling swimming locomotion as well as obtaining direct measurements of physical properties of the worms [71, 72, 93, 94]. Backholm *et al* (2015) directly measured the forces experienced by worms swimming in viscous fluids, by catching the nematode by its tail with a force-calibrated micropipette, and measuring the pipette deflection in two orthogonal directions [93]. They employ resistive force theory to determine the drag coefficients, as well as to calculate the viscous power output of the swimming worm, finding that this value is constant over the range of fluid viscosities tested. This invariance of power output was also observed by

Fang-Yen *et al* (2010) [71], and indicates that *C. elegans* actively changes its undulatory gait in order to maintain the same level of energy output across different environments.

Backholm *et al* (2015) found that the experimentally measured intrinsic normal drag coefficient surprisingly transitions between classical models of Lighthill at low viscosities (approximately 5–6) to models of Gray and Hancock at high viscosities (approximately 3). This transition was attributed to the gait modulation of the nematode, adapting from a swimming gait (large-amplitude motion), to a more conventional crawling gait (small-amplitude motion).

Adaptations of resistive force theory have been shown to effectively predict the dynamics and properties of crawling (as opposed to swimming) worms, despite only providing an empirical framework. Although the theory was originally developed for the context of swimming microscopic slender bodies, the drag anisotropy can be set to a value much smaller than $1/2$ due to the environment experienced by a worm crawling on agar having higher-friction and the worms experiencing less slippage. This approach has been shown to provide effective empirical models of crawling worms, and has been widely employed to study crawling gaits, kinematics and properties [27, 32, 81, 85, 95].

Resistive force models of crawling worms have also been constructed based on direct experimental measurements. Rabets *et al* (2014) directly measured the forces required to drag worms on the surface of agar in both the tangential and normal direction, finding that the forces depend on the surface viscoelasticity [34]. They found drag forces increased on gels with higher agar concentration, and did not scale linearly with velocity. This indicates that r_k may be non-constant in this context and thus a global drag anisotropy cannot be defined. However, an adaptation to resistive force theory in which the force–velocity mapping scales nonlinearly can capture the velocity dependence of the drag coefficients. Both linear and nonlinear resistive force theory models have been shown to accurately reproduce

and predict worm paths from the sequence of body postures [35]. Keaveny and Brown (2017) computationally determine the optimal drag anisotropy values at the level of individual worms, by minimising the difference between experimentally observed velocity, and the velocity reconstructed by the resistive force theory model [35]. For the linear model, the optimal drag anisotropy was found to be approximately $r_k = 1/60$. For the nonlinear model, the drag anisotropy scaled with the velocity according to:

$$r_k = \frac{\beta_T \boldsymbol{u}^{\gamma_T - 1}}{\beta_N \boldsymbol{u}^{\gamma_N - 1}} \tag{4.1}$$

where the parameters γ_T, γ_N govern the nonlinear nature of the model (when $\gamma_T = \gamma_N = 1$, parameters in the expression reduce to $\beta_T = K_T$ and $\beta_N = K_N$ and the linear resistive force theory model is recovered). In general, optimal values for these parameters were found to be $\beta_T \approx 0.37$, $\beta_N \approx 5.9$, $\gamma_T \approx 0.5$, $\gamma_N \approx 0.37$, so for average worm speeds (in the range of approximately $50-150\mu$m per second), the drag anisotropy was found to be $r_k \approx 1/10$.

A factor contributing to the discrepancy between experimentally measured and numerically optimal values of the drag anisotropy is the groove that is created by the worm when crawling across the agar. The profile of the groove (its width and depth) was found by Rabets *et al* to be dependent on the velocity of the worm and the stiffness of the substrate [34]. Worm sinking depths increased on softer gels, with a lower percentage of agar. Sauvage *et al* (2011) [82] developed a mechanical model of worms crawling on gel which included capiliarity (which pins the worm onto the substrate), and estimated the energy costs associated with motion along and perpendicular to the groove. They found decreasing efficiency as the ratio of viscous stress to elastic stress increased. Parida *et al* (2017) also studied the effects of grooves and substrate stiffness on *C. elegans* locomotion [96]. The stroke effectiveness of worm locomotion (defined as $\eta = v_c/v_w$ where v_c and v_w are the centroid and wave velocities respectively) was found to in fact decrease as

the substrate becomes stiffer. This result of higher effectiveness on softer surfaces was attributed to the groove height being higher on these substrates, yielding increased resistance from the side walls of the agar, resulting in less lateral slippage.

In this thesis, the data that is analysed is of worms crawling on an agar surface. The precise value of the resistance coefficients across a breadth of gaits and environments remains an open question, and an active area of research. This is due to the limitations of resistive force theory, as well as varying conditions resulting in the value of r_k not being known very accurately. Estimates of r_k for this environment in the literature range from over $1/5$ to less than $1/50$ [32, 34, 35, 74, 93]. Acknowledging this, in our analysis and results presented later in this chapter we fix r_k at the intermediary value of $1/10$. In our analysis, the important assumption is not the value of r_k itself, as the efficiency results scale linearly with this parameter. Rather, what is important is that we are assuming r_k is constant across all strains in the data.

Stroke effectiveness and efficiency of *C. elegans* locomotion

In Parida *et al* (2017), no direct relationship between effectiveness and centroid speed was observed. Furthermore, maximum centroid speed was not achieved when substrate slippage was minimised. In their study, maximum forward velocity was achieved when substrate elasticity was equal to 5.37 kPa (1% agar with 0.01% silica nanoparticles), yet maximum stroke effectiveness was achieved with the softest substrate tested with elasticity of 0.755 kPa (1% agar with 2% gelatin) [96]. As the groove height is higher on softer surfaces, the lateral resistance offered by the side walls of the groove increases. Estimating the drag anisotropy (by resistive force theory), and assessing gait efficiency (from Childress (1981) [23]) as

$$\eta = \frac{\alpha(K_N/K_T - 1)}{\alpha(K_N/K_T) + 1}$$

where $\alpha = 2\pi^2 A^2/\lambda^2$ for A the wave amplitude and λ the wavelength, they observed little variance in gait efficiency for substrates with elasticity in the range of $2.28 - 5.37$ kPa, indicating that there is no direct correlation between efficiency and drag anisotropy.

The measure of stroke effectiveness as the ratio of centroid velocity to velocity of propagating waves is commonly adopted to assess the optimality of *C. elegans* undulatory locomotion. Krajacic *et al* (2012) in describing *C. elegans* swim gait also define effectiveness as the ratio of body velocity to wavespeed, studying the effect of room temperature on the undulatory gait of wildtype N2 worms [94], observing a small decrease in effectiveness at 25°C compared with 20°C and 16°C. They also analysed the locomotion of several *C. elegans* mutant strains, specifically strains with mutations affecting neuromuscular structure and function. Whilst finding significant differences between N2s and mutant strains in some biomechanical phenotypes, visually apparent defects between N2s and mutants in motility gaits were generally not observed, and the stroke effectiveness showed little variation between strains. Phenotypes that did produce significantly different results from N2 included swimming speed, body curvature, and mechanical swimming power, and strains with mutations affecting similar biological processes exhibited similar patterns of biomechanical differences.

Karbowski *et al* (2006) [85] also analysed *Caenorhabditis* locomotion effectiveness across different mutant strains, as well as across different developmental stages and other nematode species, including *C. briggsae and C. japonica*. Again, the 'effectiveness coefficient' used in this study was defined as the ratio of propulsion velocity to wave velocity, but the experimental setup was for worms crawling on agar gels. The stroke effectiveness remained relatively constant across different developmental stages of wildtype *C. elegans*, and also exhibited little variability across the different nematode species analysed. Mutants affecting cuticle properties and muscle structure were observed to move more slowly than wild-types, and strains with significantly different stroke effectiveness from N2 included *cat-4*

and *sqt-1* and one strain of *unc-54*. This result was attributed to the fact that these worms move very slowly. They also tested different concentrations of agar in the substrate, finding little variation in the stroke effectiveness up to 6% agar concentration, and only a slight decrease at 8% (confirmed by Parida *et al* (2017) to a higher degree). It is reasonable to question how one can differentiate between worms not wanting to move, being sluggish and tired, versus worms not being able to move as effectively due to, for example, genetic factors. In this thesis, from a phenotyping perspective we look empirically at their viscous dissipation, whether by choice or defect. Such differentiation is not addressed here.

Majmudar *et al* (2012) [33] investigated the swimming of *C. elegans* through arrays of micropillars of different densities, varying the spacing between pillars (relative to the length of the worm). This was the chosen experimental parameter due to the fact that the number of pillars the worm comes into contact with depends on both the spacing between pillars and also its length. For the highest density (the smallest spacing) tested, worms were in constant contact with one or more pillars, and adopted higher curvature, shorter wavelength body postures. Worms generally travelled along the diagonals of the micropillar array with high velocity, between periods of swimming that were locally-concentrated. Increasing the spacing between the micropillars resulted in high-velocity diagonals again, as well as looped-trajectories. At the lowest pillar density tested, the wave amplitude of the worm swimming gait was approximately equal to the lattice spacing, so contact between the worm and pillars rarely occurred, resulting in mostly straight-line motion, with turns typically arising when the worm did come into contact with a pillar.

The stroke effectiveness of the worms was determined by scaling the worm velocity with undulation frequency and bodylength. Worm undulation frequency was found to be dependent on the lattice spacing, with higher frequencies occurring when pillars were further apart, which was when worms adopted visibly regular swim-like behaviour. The highest stroke effectiveness (and velocity) was found

for the intermediate density of micropillars — the pillar spacing corresponding to the case where the worm moves one diagonal lattice spacing in a single undulation. This result was also observed in simulations of their mechanical and hydrodynamical model of the worm, in which they also considered the hydrodynamic efficiency (average speed / average viscous dissipation) of model worms, measuring the speed of locomotion achieved for a fixed power output per stroke. Taking into account both the dissipative cost due to pushing against pillars as well as the fluid, the maximum hydrodynamic efficiency was attained at the point where the undulation frequency yields the highest speed for a given pillar spacing. This indicates that, for the simulated worm, maximum hydrodynamic efficiency is achieved by decreasing undulation frequency as pillar spacing increases. This was the opposite of what was observed in the experiments with real swimming worms in the micropillar arrays, in which frequency increased as pillar spacing increased. This suggested that *C. elegans* does not adjust its undulation frequency to maximise hydrodynamic efficiency, at least in this environment. It is possible that the worms in fact cannot adjust undulation frequency in the higher-spacing pillar environments, as they may not have a good way of responding to the structure when they are not in constant contact with it.

A similar result was presented by Bilbao *et al* (2013) [77], in a study which showed that confinement enhances the stroke effectiveness of *C. elegans* swimming due to the increased resistance coefficient ratio. This result was obtained in the context of a piecewise-harmonic curvature model, simulations of which showed that normalised swimming velocity (average velocity of the worm / propagation velocity of the curvature wave) is maximised for a wavelength shorter than is typically observed for *C. elegans* swimming in water. This study also observed the maximum normalised velocity was achieved by the simulated worms when the correct balance of space between obstacles and dimensions of the worm's body allowed for optimal frequency. Hence, undulation frequency and the speed of the propagating dorsal-ventral waves to generate motion, evidently influence the effectiveness of

C. elegans locomotion.

Berman *et al* (2013) [97] theoretically determined the most hydrodynamically efficient swimming gait for a low Reynolds number undulator, using both approximate resistive force theory and also particle-based numerical computations which captured internal hydrodynamics in the body (taking into account the intra-filament hydrodynamic interaction). The particle-based computationally optimal was found to diverge from the prediction from the resistive force model. They determined that there is an optimal combination of the dimensionless undulation amplitude and wavenumber that yields the furthest advancement per period of undulation. The particle-based model was applied to *C. elegans* swimming data, and whilst the model and data exhibited similar values of the optimal amplitude and wavenumber of undulations, the real swimming *C. elegans* actually out-performed the particle-based model in both displacement and hydrodynamic efficiency. Beyond quantitative out-performing, the trends between wavenumber and efficiency between the model and real worms revealed that the nematode is superior to the model swimmer in terms of both the swimming distance per stroke and also hydrodynamic efficiency as estimated from particle-based computations exploiting the nematode swimming gait extracted from experiments. This indicates the importance of the amplitude modulation in the waveform adopted by *C. elegans*, deviating considerably from a simple sine wave as in the model.

Variations between observations across the literature discussed above underline the importance of further investigation of *C. elegans* gait efficiency. To summarise for the case of stroke effectiveness, Parida *et al* found no direct relationship between centroid speed and stroke effectiveness, and Krajacic *et al* found little variation in effectiveness between different strains [94, 96]. Karbowski *et al* found some variation across mutant strains, and Majmudar *et al* found the highest stroke effectiveness at the pillar spacing corresponding to the scenario where the worm moves one diagonal lattice spacing per undulation [33, 85]. It is evident, both from theoretical and computational models, as well as widespread experimenta-

tion across a variety of contexts, that external environment influences *C. elegans* locomotion, and consequently, the optimality of its motion also varies. In addition, as evidenced by the study of Berman *et al*, wave amplitude along the body is also closely linked to optimality of locomotion [97]. These factors lie amongst multiple others (eg development, genetics, ecology) that may also be closely linked to gait optimality.

Neuronal control

In addition to external environment, a fundamental determinant of how and why *C. elegans* move the way they do is their neural circuitry. As well as being the first animal to have a fully-sequenced genome, *C. elegans* also boasts the first (and so far only) fully-mapped connectome of any animal[†] [4, 5]. This fully-mapped network of the 302 neurons comprising the *C. elegans* nervous system offers a valuable opportunity for connecting behaviour and neural circuitry.

Interactions between distinct classes of *C. elegans* neurons have been identified and associated with the different locomotion strategies of the organism. Specifically, the rich-club network (a network of hub nodes that are densely connected among themselves compared with nodes of a lower degree, enhancing communication and coordination between sub-circuits of neurons) of *C. elegans*' nervous system comprises eleven classes of neurons [98], of which nine are prominent in sensorimotor decisions and motor commands [99]. For example, one class of head neurons (DVA) are proprioceptive — sensing self-movement and the worms body position — and communicate with both forward and backward locomotion neuron classes, coordinating both accelerations and reversals [99]. Proprioceptive neurons have been found to clearly play a role in the propagation of *C. elegans* undulatory body postures for locomotion [88, 100, 101].

[†]Partial connectomes of the fruit fly, mouse, and of course, in our quintessential anthropocentricity, the human brain have also been successfully reconstructed. The larva of the marine annelid *Platynereis dumerilii* has also had its connectome fully mapped, and the *Drosophila* larval connectome is also nearing completion.

The neural circuitry of the organism is of course impacted by its genetic factors. Genes encode instructions for an organism's entire structure and function, and so mistakes in instructions can lead to diminished or complete loss of function. For example, Zheng *et al* (1999) observed that *C. elegans* that expressed a mutation in the gene *glr-1* which encodes for ionotropic glutamate receptors (a glutamate-activated receptor that functions by opening ion channels that enable specific ions to stream in and out of the cell) displayed rapid alternation between forward and backward locomotion [102]. Mutations in this gene are also associated with disrupted mechanosensation, and this hyperreversal phenotype observed in the *glr-1* mutants pointed to the role of sensory input in the gating of movement. More recently, the four fundamental eigenworm shapes that characterise crawling postures (Stephens *et al* (2008) [103]) were also found to capture mutant shapes [104]. Brown *et al* (2013) established a dictionary of behavioural motifs that revealed clusters of genes affecting *C. elegans* locomotion [104], by clustering mutants into related groups based on how well they performed the different behaviours in the dictionary. In terms of how well the eigenworms characterised the mutant body postures, *unc-4* and *unc-34* were among those worst-fit by the wildtype eigenworms. Mutations in these genes affect synaptic specificity, further underlining the importance of neuronal circuitry in gait expression.

A recent study by Deng *et al* (2021) demonstrated that in fact inhibition underlies fast undulatory locomotion [105]. *C. elegans* expressing mutations in the genes *unc-25*, *unc-46* and *unc-49* were found to decrease in undulation frequency when moving away from adverse stimuli (probing by a blunt glass rod). Mutations in these genes are associated with impaired GABA transmission (a principal inhibitory neurotransmitter for the neurons in question), hence pointing to the role of inhibition in fast body undulation, and further highlighting the role of genetic factors and neuronal control in efficient locomotion.

Efficiency of *C. elegans* across mutant strains

As evidenced by previous studies, *C. elegans* mutant strains often move visibly differently (and arguably less efficiently) than wildtype N2 worms, including but not limited to slower movements, uncoordination, or hyperactivity. In addition, some strains have been observed to exhibit coiling behaviours, and tendencies to move in a 'less straight' manner. Previous studies reporting quantitative differences between *C. elegans* gait efficiency often quantify efficiency as simply the ratio of body velocity to wave propagation speed, inherently penalising swimming gaits relative to crawling gaits, or are limited in the number of different strains of the organism. However, even between a small number of strains, quantifiable differences in efficiency compared with N2 can be detected.

For example, Karbowski *et al* (2006) found *cat-4* to have be significantly less wave efficiency than N2. By simply looking at the strain compared with N2, by eye we can see that this mutant is moving less efficiently compared to the wildtype healthy worm (comparison of fig. 4.1 and fig. 4.2). This strain of *C. elegans* expressing a mutation in the *cat-4* gene is in fact associated with dystonia in humans — a movement disorder in which muscles contract involuntarily. This is just one example of a *C. elegans* human disease model.

4.2.2 *C. elegans* as a human disease model organism

C. elegans are a popular model organism for investigating a range of biological phenomena. From an anthropocentric perspective, 60–80% of human genes have an ortholog (a gene that evolved from a common ancestor by speciation) in the *C. elegans* genome [106], and 40% of genes known to be associated with human diseases have clear orthologs in the *C. elegans* genome [107]. It is therefore a valuable and promising platform with which to perform disease model screens, to investigate genetic diseases in humans. *C. elegans* have an average pe-

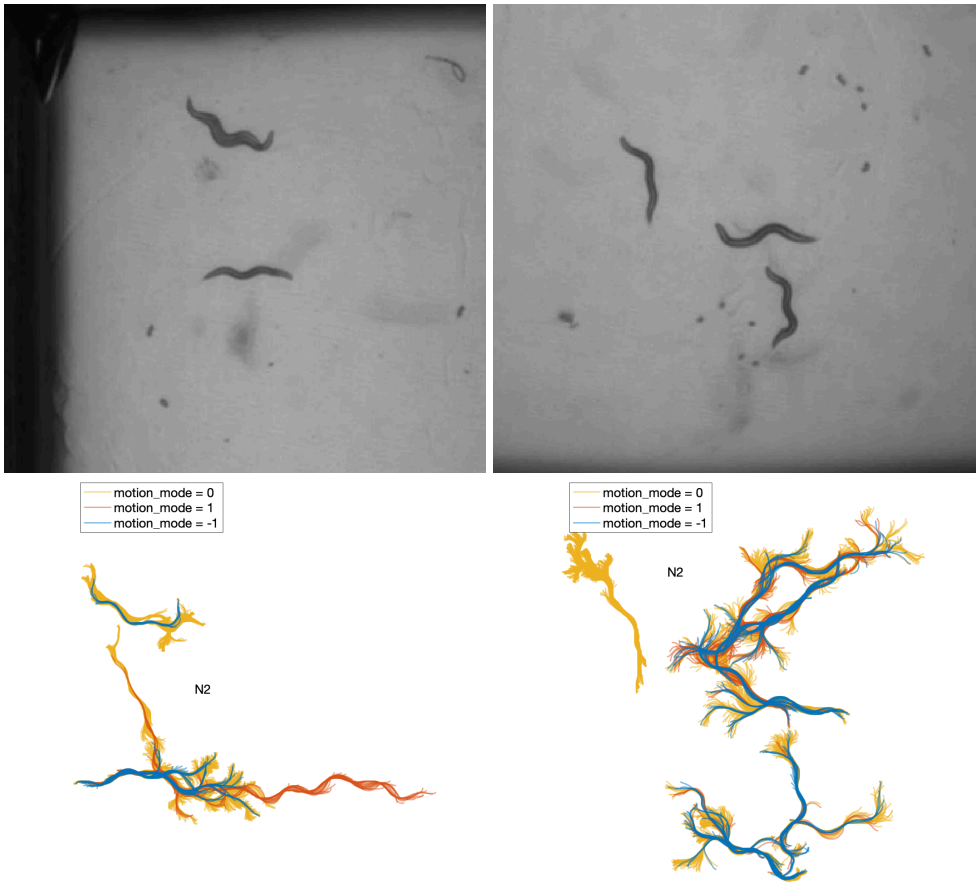

Figure 4.1: Example data from N2 worms from two different wells. Stills from the mp4 file and corresponding skeletons for the entire 6 minute video, seperated by motion mode corresponding to paused ($= 0$), forwards ($= 1$), or backwards ($= -1$). Skeletons extracted by Tierpsy tracker software. Data unpublished at time of submission of this thesis (May 2022).

riod of developmental completion (from hatching to adult) of 3.5 days, and high rate of reproduction, with individual worms existing primarily as self-fertilising hermaphrodites (with males occurring at a frequency of $< 0.2\%$). When hermaphrodites reproduce, almost 100% of the individual's genes are passed on to their (up to 300) progeny, so the offspring of a single worm are genetically nearly identical. This attribute combined with their short life cycle enables high throughput screens of this organism with an exceptional degree of genetic control.

Rare genetic diseases in humans manifest themselves in a range of symptoms with varying severity. The majority of rare genetic diseases in humans affect the central

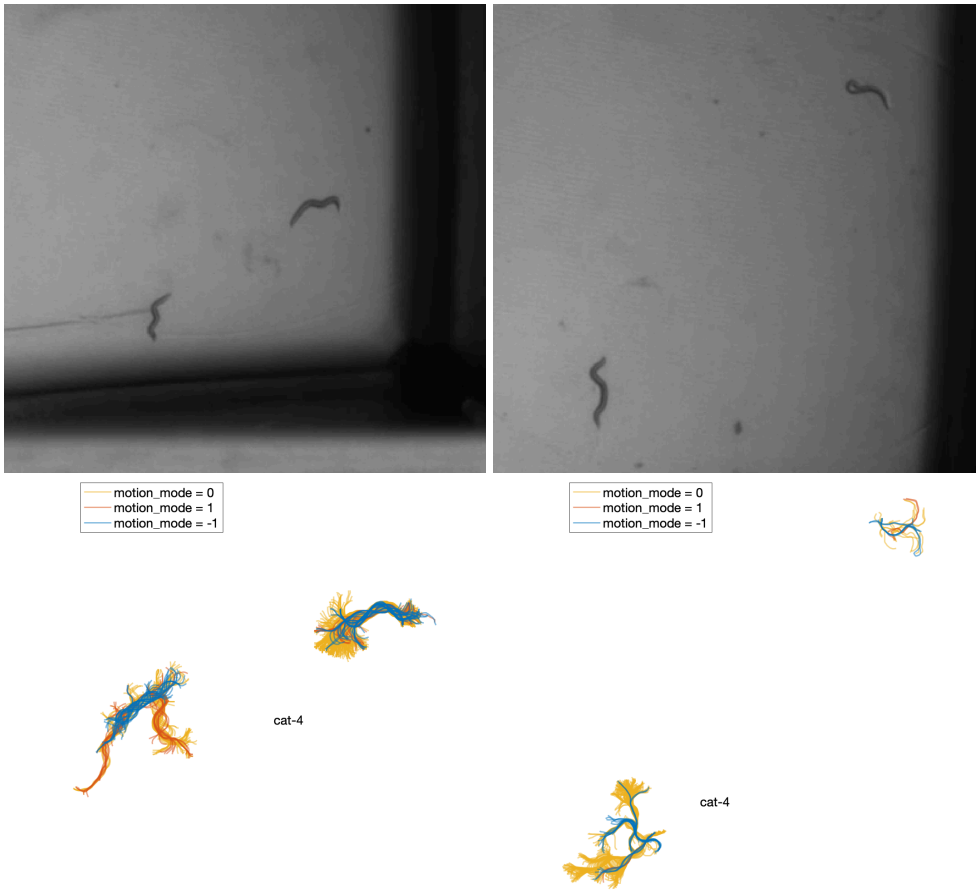

Figure 4.2: Example data from *cat-4* worms from two different wells. Over the course of the 6 minute video file, this strain is observably less active and moves less optimally than N2. Data unpublished at time of submission of this thesis (May 2022).

nervous system, resulting in neurodevelopmental, cognitive, behavioural and/or psychiatric symptoms [108]. Due to advances in genome sequencing technologies, in recent years the genetic causes of many such diseases have been identified [109]. In developing treatments for human genetic diseases, *C. elegans* provides a promising platform for identifying potential drug targets. The latest genome editing technologies enable precise required mutations to be made in the model organism which reflect the genotype of the genetic disease in humans. When these mutant strains exhibit visibly distinct behaviours and characteristics compared with the standard wild-type N2 'healthy' strain, this further increases the possibility of gaining insight into the genetic disease in humans.

Furthermore, if such characteristics (eg uncoordinated motion, hyperactivity, fainting, to name just a few examples of *C. elegans* phenotypes that have been widely-observed throughout the worm literature) can be reversed in drug treatment assays, this could lead to the identification of new or repurposed compounds to treat the associated genetic diseases in humans. A recent example of *C. elegans* drug screening illustrating the promise of such approaches is Patten *et al* (2017), which modelled ALS with disease-associated genetic variants of conserved genes in the nematode, leading to discovering the effectiveness of the antipsychotic pimozide in treating the disease [110]. A key component of this discovery was the presence of a distinct and quantifiable phenotype, which was able to be reversed by successful drug candidates. Tracking and quantitative phenotyping in *C. elegans* is fundamental to understanding the connection between genetics and behaviour. However, many phenotypes are difficult to observe by eye, so quantitative tools and lenses are necessary to asses such phenotypes.

Behavioural phenomics

To understand the connection between genetic variation and variation in physical characteristics (phenotypic variation), it is necessary to have good phenotypes that are both quantitative and well-defined. Measuring phenotypes is essential in many areas of biology, in particular in genetics where mutations in single genes can yield strong effects on physical and behavioural characteristics. Successful phenotypic measuring can give rise to extensive characterisations of a range of traits at the level of individual organisms. Such characterisations can be invaluable when linking genotypes and phenotypes, in particular when linking genetic differences with differences in movement behaviours.

High-throughput phenotypic screening technologies, such as Tierpsy [11], enable this invaluable measuring of quantitative behavioural phenotypes. Using computational ethology, a phenomic approach to behaviour analysis yields a high-

dimensional representation of animal behaviour, namely *C. elegans* and other nematodes. The behavioural features captured by Tierpsy are not only intuitive and interpretable — compared with features that may be detected by, for instance, black-box machine learning algorithms — but also powerful in that behavioural differences between mutant strains and wild-types are effectively detected [10].

4.2.3 Efficiency as a phenotyping lens in *C. elegans* models of human genetic disease

Is efficiency an interesting phenotype for *C. elegans* behaviour? Namely, does it yield quantitative differences between strains, in particular in the context of a human genetic disease model strain screening?

Developing gait optimality as a quantitative behavioural phenotype for *C. elegans* locomotion — or more generally, the locomotion of any organism — would enhance the current set of phenotyping tools. Currently, in order to measure a change in gait optimality, measurements would have to be taken across many different dimensions, such as curvature at different parts of the body, speed, reversal frequency, etc. It is not sufficient to simply consider speed when concerned with optimality — when comparing the walking gaits of two given people, it is not the case that the one that is walking faster is necessarily walking more efficiently. Multiple different dimensions would have to be monitored simultaneously, and there would be a lack of certainty that the correct combination of different dimensions and aspects of movement were being considered. Efficiency as a quantitative phenotype has the potential to serve as an interesting, integrative measure, that is applicable to any strain, capturing a complete picture of a given organism's mobility, and yielding a scalar, numerical value which informs us 'how optimal is this animal compared to the wild-type'.

This quantitative behavioural phenotyping approach could lead to opportunities to perform screenings for drugs that are potentially able to treat and reverse the

phenotypes of disease-model worms, and hence potentially treat the corresponding disease in humans. To this end, and to the objective of this thesis chapter, we want to be able to quantify the difference in gait optimality between wild-type worms and mutant strains, so we can use it as a phenotyping tool. In order to do that, we employ principles from low Reynolds number hydrodynamics and resistive force theory, which have been widely shown to effectively capture the nematodes undulatory gait previously, to measure how optimal a particular *C. elegans* gait is.

C. elegans gene	Human orthologue	Human disease association	Strain name
add-1	ADD3, ADD1	Cerebral palsy; Intellectual disability	PHX1598
avr-14	GLRA1, GLRB	Hyperekplexia	PHX1576
bbs-1	BBS1	Bardet-Biedl syndrome (ciliopathy)	PHX1588
bbs-2	BBS2	Bardet-Biedl syndrome (ciliopathy); Retinitos Pigmentosa	PHX1547
C43B7.2 (*figo-1*)	FIG4	ALS; Epilepsy with polymicrogyria	PHX1562
cat-2	GHC1	Segawa syndrome	PHX1542
cat-4	TH	Dystonia	PHX1591
dys-1	DMD	Muscular dystrophy (Duchenne and Becker type)	PHX1688
glc-2	GLRA1, GLRB	Hyperekplexia	PHX1557
glr-1	GRIA3, GRIK2	Intellectual disability	PHX1556
glr-4	GRIK2	Intellectual disability	PHX1518
gpb-2	GNB5	Intellectual disability; Retinal disease; Hypotonia; Seizures	PHX1577
kcc-2	SLC12A5, SLC12A6	Epilepsy	PHX2673
mpz-1	MPDZ	Hydrocephalus	PHX1522
nca-2	NALCN	Hypotonia	PHX1612
pink-1	PINK1	Early onset Parkinsons	PHX1546
snf-11	SLC6A1	Myoclonic atonic epilepsy	PHX2683
snn-1	SYN1, SYN2	Epilepsy; Schizophrenia	PHX2695
tmem-231	TMEM231	Joubert syndrome; Meckel syndrome	PHX1575
tub-1	TUB, TULP1	Retinal dystrophy	PHX1563
unc-25	GAD1	Cerebral palsy; Schizophrenia; Epileptic encephalopathy	PHX1651
unc-43	CAMK2A, CAMK2B	Epilepsy; Intellectual disability	PHX1688
unc-49	GLRA2	Epilepsy; Hyperekplexia	PHX2856
unc-77	NALCN	Hypotonia	PHX1548
unc-80	UNC80	Hypotonia	PHX1531

Table 4.1: The *C. elegans* disease screen strains, and the human disease associated with the strain. The strains selected are associated with neurological disorders in humans, and therefore are expected to exhibit behavioural differences from the wildtype. This is a recently-obtained dataset in the Behavioural Phenomics lab, MRC LMS. Data was collected and analysed with state-of-the-art imaging systems and computational ethology, yielding high-quality data valuable for analysis in this thesis. Strain selection and experimental (wet lab) methods were carried out by Ida Barlow and Tom O'Brien. In this thesis, the data is analysed in order to test the usefulness of gait efficiency as a phenotype. No assumptions or impositions of optimality are made. Data unpublished at time of submission of this thesis (May 2022).

4.3 Methods

Experimental methods (strain selection, worm and plate cultivation and preparation, and video acquisition) were carried out by Ida Barlow and Tom O'Brien in the Behavioural Phenomics lab, MRC LMS. Videos were processed using Tierpsy Tracker, and per-well feature extraction and gait optimality features were obtained with computational pipelines constructed by Madeleine Hall in the MATLAB programming platform.

4.3.1 Experimental methods

Disease model strain selection

A list of the disease model strains analysed in the behavioural phenotypic screen along with their associated human disease is given in Table 4.1. This is a recently-obtained dataset in the Behavioural Phenomics lab, MRC LMS, that was acquired for the purposes of a different project, unrelated to this thesis. This data (and project) are unpublished at the time of submission of this thesis. The benefit of analysing this data in this thesis chapter lies in its recentness of acquisition, high image quality, and availability within the lab. The genes were not selected for the particular study of gait efficiency. No assumptions of efficiency or optimality across any of the strains are imposed. A short summary of how the strains were selected (for the unrelated project) is provided below. Strain selection was performed by Ida Barlow, Tom O'Brien, and André Brown.

The strains were chosen using a combination of automated mining of databases and hand selection of interesting targets. The *C. elegans* genes were identified in Ortholist — a comprehensive dataset of *C. elegans*-human orthologs compiled in 2018 by comparative genomic analysis [111]. The genes were then filtered according to: 1) if more than 2 orthology programs agreed that the *C. elegans* gene

is a good ortholog for a human gene, and 2) the human ortholog of the *C. elegans* gene has a disease association. Furthermore, genes were eliminated unless: 1) the associated human diseases are neurological disorders, and therefore likely to affect behaviour, 2) the *C. elegans*/human gene encodes either a neurotransmitter or a neurotransmitter receptor, or 3) the *C. elegans* gene is associated with chemotaxis or feeding behaviours. Genes that are developmental or lethal when knocked out were rejected, and genes that may result in interesting behavioural phenotypes or that are likely to be good drug targets were accepted. Mutants were designed and made by SunyBiotech in their reference N2 strain background, using CRISPR/Cas9 gene editing technology.

Worm and plate preparation

As stated above, this data was acquired by the Behavioural Phenomics lab for a project that is unrelated to the analysis performed in this thesis. For your information, a summary of the experimental methods is provided below. Wet lab work was carried out by Ida Barlow and Tom O'Brien.

All strains were cultured on Nematode Growth Medium (NGM) at 20 degrees celsius and fed with *E. coli* strain OP50 following standard procedure [112]. *C. elegans* is usually grown in laboratories using OP50 as a food source. The growth of OP50 is limited on NGM, which is desirable as it allows for easier observation and better tracking of the worms.

Populations of young adult worms for imaging were obtained for each of the strains, by allowing newly-hatched L1s to develop for two and a half days (detailed protocol given in [113]). Several strains were developmentally delayed, and thus were given more time to develop: *cat-4*, *gpb-2*, *kcc-2*, and *unc-25* were allowed to develop for three and a half days and *dys-1*, and *pink-1* were allowed to develop for five and a half days.

On the day of imaging, young adults were prepared (detailed protocol given in [114]), and transferred to OP50-seeded 96-square well imaging plates (3 worms per well) using a COPAS 500 Flow Pilot (detailed protocol given in [115]), and returned to an incubator for 1.5 hours. Plates were then transferred onto the multi-camera tracker for another 30 minutes for habituation, prior to imaging (detailed protocol provided in [116]).

4.3.2 Computational methods

Image acquisition and processing

Video data of the worms was acquired and processed following the methods described in detail in [117]. Videos were recorded at 25 frames per second with a resolution of 12.4 μm per pixel. Three videos were taken sequentially: a 5 minute pre-stimulus video, a 6 minute blue-light recording with three 10 second blue-light pulses starting at 60, 160 and 260 seconds, and a 5 minute post-stimulus recording. Blue light is a noxious stimulus, and therefore upon stimulation the nematode will exhibit typical avoidance behaviours, such as acceleration and reversal. Blue light can elicit an escape response in worms, thus expanding the range of observable behaviours [118, 119].

Videos were segmented and tracked using Tierpsy Tracker [11]. After segmentation of worm skeletons, non-worm objects mistakenly tracked by the software were excluded from being classified as worms via a convolutional neural network classifier [117]. A manual threshold to filter skeletonised objects was also applied, to further filter skeletonised objects likely to be non-worms (eg well edges, agar cracks). Objects that were outwith the range 800–1400 μm in length were filtered out prior to analysis. As an additional quality control measure, Tierpsy Tracker's GUI viewer was used to mark wells with visible contamination, agar damage, or excess liquid as "bad", and exclude these wells from downstream analysis.

Feature extraction and gait optimality features

Following tracking, a set of behavioural features was extracted for each well [10]. The extraction of behavioural features was performed on a per-track basis and are then averaged across tracks to produce a single feature vector for each well. Features are classified as either time series features or event features.

Time series features (eg velocity, dissipation) are obtained frame-by-frame for each worm. Features that can be localised to a part of the body can be calculated separately for distinct segments along the worm (head, body, tail). Features can also be subdivided according to the state of motion of the worm (paused, forward, or backward). Time-averaged features were obtained by averaging over 1 second windows of features calculated on a frame-by-frame basis. The distributions of features are quantified by calculating the 10th, 50th, and 90th percentile values, as well as the interquartile range. This results in features such as *time_avg_head_viscous_dissipation_50th* which is the median 1 second time-averaged dissipation by the head of the worm. Event features such as *motion_mode_paused/forward/backward_fraction* describe the fraction out of the total number of recorded frames the worms spend in either paused, forward or backward motion mode for a given well.

The position of the worm at time t is given by $\boldsymbol{x}(s,t) = [x(s,t), y(s,t)]$ where $s \in [0, L]$ is the arc length, measured from head ($s = 0$) to tail ($s = L$) along the length of the body (see fig. 4.3). The features of normalised velocity, centroid speed, viscous dissipation, and hence efficiency were all obtained for normalised skeleton length. Worm skeletons at each frame are tracked at precisely $N_s = 49$ points along the body, from head tip to tail tip. Whilst worm length may vary between mutant strains, the aforementioned features were calculated for normalised worm length $L = 1$. Video data was obtained at 25 frames per second, and to mitigate noise in the tracking data a window of 10 frames was used to calculate velocity (non-overlapping, as opposed to a sliding window), ie $\Delta t = 0.4$ seconds.

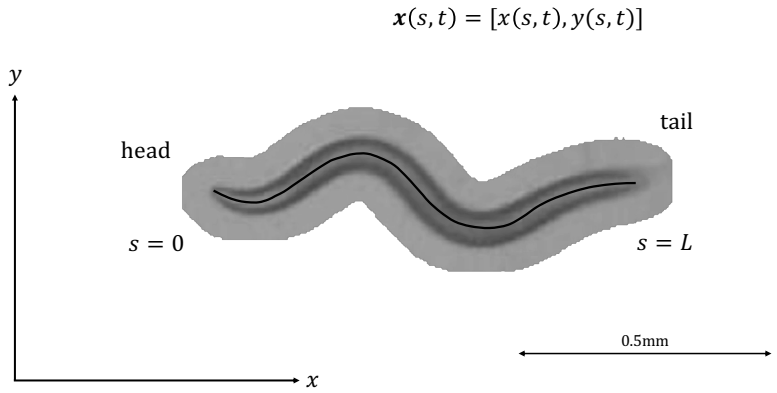

Figure 4.3: An image of *C. elegans* (adult N2) crawling on agar, with axes and annotations added. The body is parameterised by arc length $s \in [0, L]$, and its position at time t is given by $\boldsymbol{x}(s,t)$.

The worm centroid is defined as the mean point along the skeleton in the horizontal and vertical directions for a given frame:

$$\boldsymbol{x}_c(t) = \frac{1}{N_s}\sum_{s=0}^{L}[x(s,t), y(s,t)] \tag{4.2}$$

and hence may lie outside the worm body, for example for C-shaped postures. The normalised centroid speed is calculated according to

$$U_c(t) = \left|\frac{\boldsymbol{x}_c(t+\Delta t)-\boldsymbol{x}_c(t)}{\Delta t}\right| = \sqrt{\left(\frac{x_c(t+\Delta t)-x_c(t)}{\Delta t}\right)^2 + \left(\frac{y_c(t+\Delta t)-y_c(t)}{\Delta t}\right)^2}. \tag{4.3}$$

$U_c(t) > 0$ regardless of motion mode (ie if the worm is moving backward, centroid speed is still described at positive).

The velocity of the body is calculated via

$$\boldsymbol{u}(s,t) = \frac{\boldsymbol{x}(s,t+\Delta t)-\boldsymbol{x}(s,t)}{\Delta t} \tag{4.4}$$

and the force acting on the surroundings per unit length of the body, by resistive

force theory, is calculated as

$$\boldsymbol{f}(s,t) = (K_T - K_N)\hat{\boldsymbol{t}}(\hat{\boldsymbol{t}} \cdot \boldsymbol{u}) + K_N \boldsymbol{u}, \tag{4.5}$$

with $\hat{\boldsymbol{t}}(s,t)$ the unit tangent vector along the body in s at time t. The ratio of tangential to normal resistance coefficients (the drag anisotropy) $r_k = K_T/K_N$ is fixed at 1/10. The drag anisotropy is fixed at this value based on the studies by Shen *et al* (2012) [74], Rabets *et al* (2014) [34], and Keaveny and Brown (2017) [35], discussed in the introduction of this chapter.

The dissipation is calculated according to

$$\Phi(t) = \int_0^L \boldsymbol{f}(s,t) \cdot \boldsymbol{u}(s,t)\,\mathrm{d}s \tag{4.6}$$

$$\approx \Delta s \sum_{s=0}^{L} \boldsymbol{f}(s,t) \cdot \boldsymbol{u}(s,t). \tag{4.7}$$

where $\Delta s = 1/N_s \approx 0.02$. Features localised to a part of the body were calculated by segmenting the 49 points along the worms length into head region, body region, and tail region. For example, for head/body/tail dissipation:

$$\Phi_{\text{head}}(t) = \Delta s \sum_{s=0}^{8/49} \boldsymbol{f} \cdot \boldsymbol{u}\,\mathrm{d}s, \tag{4.8}$$

$$\Phi_{\text{body}}(t) = \Delta s \sum_{s=9/49}^{41/49} \boldsymbol{f} \cdot \boldsymbol{u}\,\mathrm{d}s, \tag{4.9}$$

$$\Phi_{\text{tail}}(t) = \Delta s \sum_{s=42/49}^{1} \boldsymbol{f} \cdot \boldsymbol{u}\,\mathrm{d}s. \tag{4.10}$$

$$\tag{4.11}$$

Time-averaged features are calculated over 1 second windows of continuous sequences of frames in the tracking data. The frame rate of the recorded videos was 25 frames per second. Time-averaged features were not calculated for frames that were not contained within a period of 25 consecutive continuous skeletons ie if

the tracked trajectory was less than 1 second long, this was discarded from the time-averaging features.

The efficiency was determined via

$$\eta_H = \frac{r_k \langle U_c \rangle^2}{\langle \Phi \rangle} \tag{4.12}$$

where $\langle U_c \rangle$, $\langle \Phi \rangle$ are the time-averaged centroid speed and time-averaged dissipation respectively (angular brackets denote time-averaging). This expression is equivalent to the hydrodynamic efficiency discussed in section 2.2.3. This feature is also, by construction, time-averaged over the 1 second windows of continuous tracking in the data.

Statistical analysis

Statistically significant differences in the behavioural feature sets extracted from each disease model strain compared to our N2 reference were calculated using a Mann–Whitney test, for testing whether samples originate from the same distribution. This is a non-parameteric test, and hence does not assume that the data is normally distributed. Each strain was compared independently with the N2 control group, and all p-values calculated for the different comparisons. Python (version 3.6.10) was used to perform the analysis. The p-values were corrected for multiple comparisons using the Benjamini–Yekutieli procedure to control the false discovery rate at 5%.

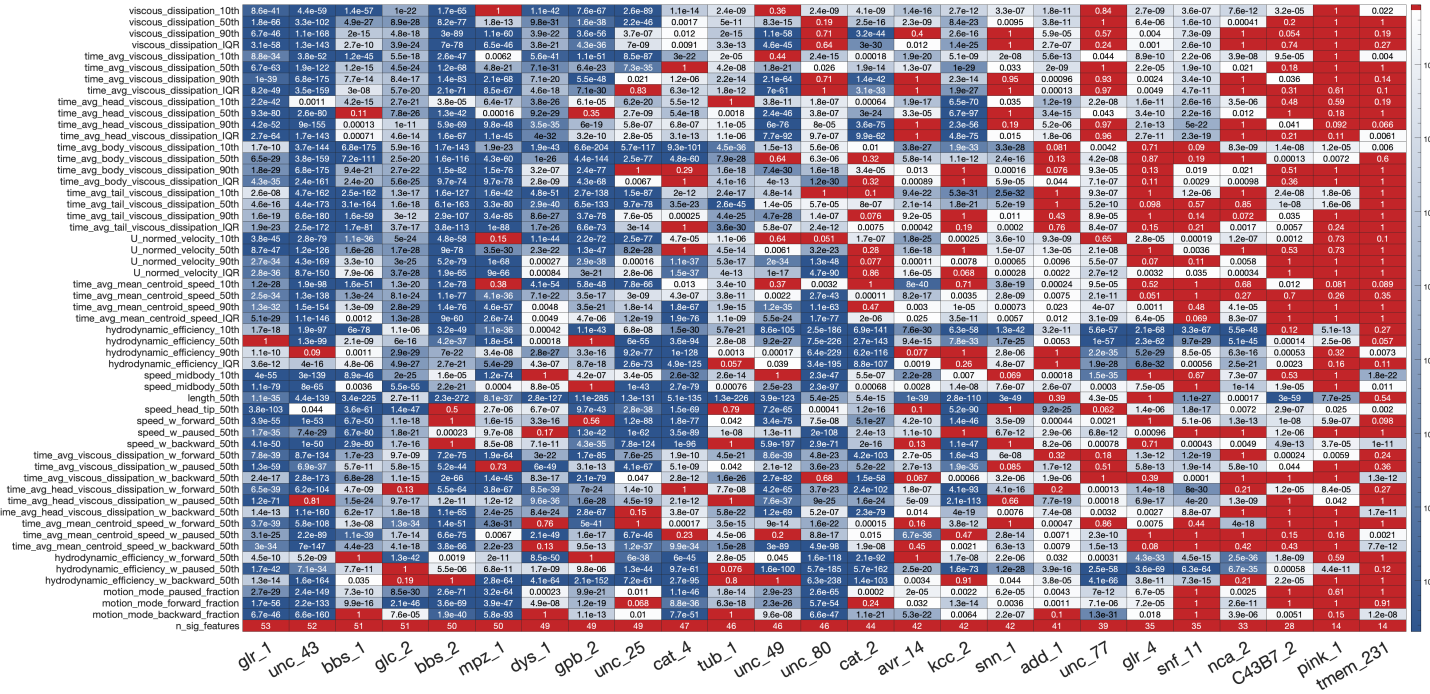

Figure 4.4: All p-values obtained from statistical analysis of the gait optimality features results. Values were calculated using the Mann–Whitney test, and corrected for multiple comparisons using the Benjamini–Yekutieli procedure, controlling the FDR at 5%. Strains are ordered from left to right by number of features significantly different from N2, the control group. Statistically significant features are distinguishable via the colour mapping: p-values less than the FDR (0.05) are coloured from white to dark blue according to how much smaller than the FDR the value is. All p-values greater than 0.05 are coloured red.

4.4 Results

An overview of the median efficiency across all strains in the disease model strain screening is shown in fig. 4.5. N2 (wildtype, 'healthy' worms) have a median hydrodynamic efficiency $\eta_H \approx 0.009$ (median 0.00899, quartiles $[0.00794, 0.0103]$). Out of 25 strains, 22 had median efficiency (*hydrodynamic_efficiency_50th*) significantly different from N2 ($p < 0.05$).

Although many of the disease model strains have lower efficiency than N2, some were found to have higher efficiency. The three strains that were found not to be siginificantly different from the N2 reference strain are *gpb-2, glr-1, tmem-231*. Of the other strains, 11 were found to have significantly lower median hydrodynamic efficiency than N2, and (coincidentally also) 11 were found to have significantly higher efficiency.

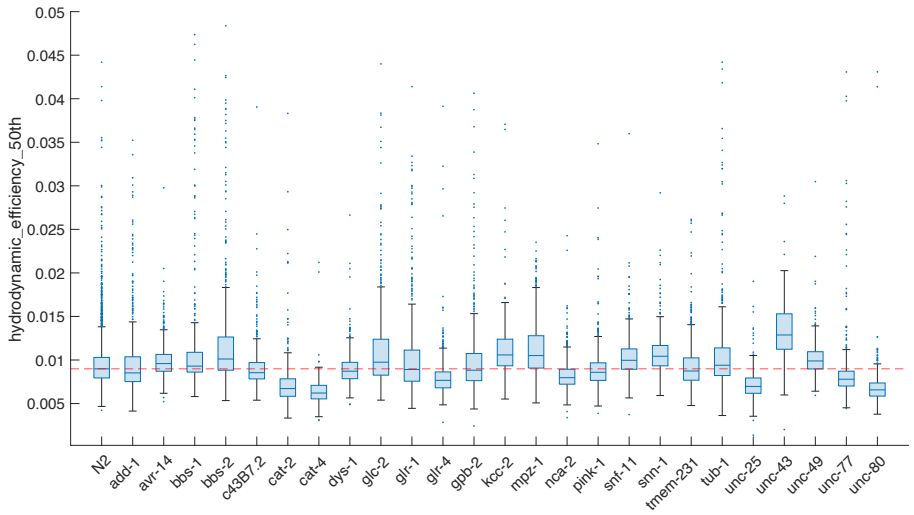

Figure 4.5: Median efficiency across all strains in the disease model strain screening. Dashed red line at N2 median for easier comparison of distributions relative to the control. All strains with the exception of *glr-1*, *gpb-2* and *tmem-231* are significantly different from N2 ($p < 0.05$).

The variation in efficiency across all of the strains can be investigated by inspecting correlations with the other behavioural features quantified and obtained in the phenotypic screen. The median efficiency correlates highly with *motion_mode_for-*

ward_fraction ($r = 0.783$), and also relatedly *motion_mode_paused_fraction* ($r = -0.755$), as well as median time-averaged normalised centroid speed — *time_avg_mean_centroid_speed_50th* ($r = 0.775$). Scatter plots of these features which correlate highly with efficiency are shown in fig. 4.6. An overview of these highly correlated features across all strains is shown in fig. 4.7.

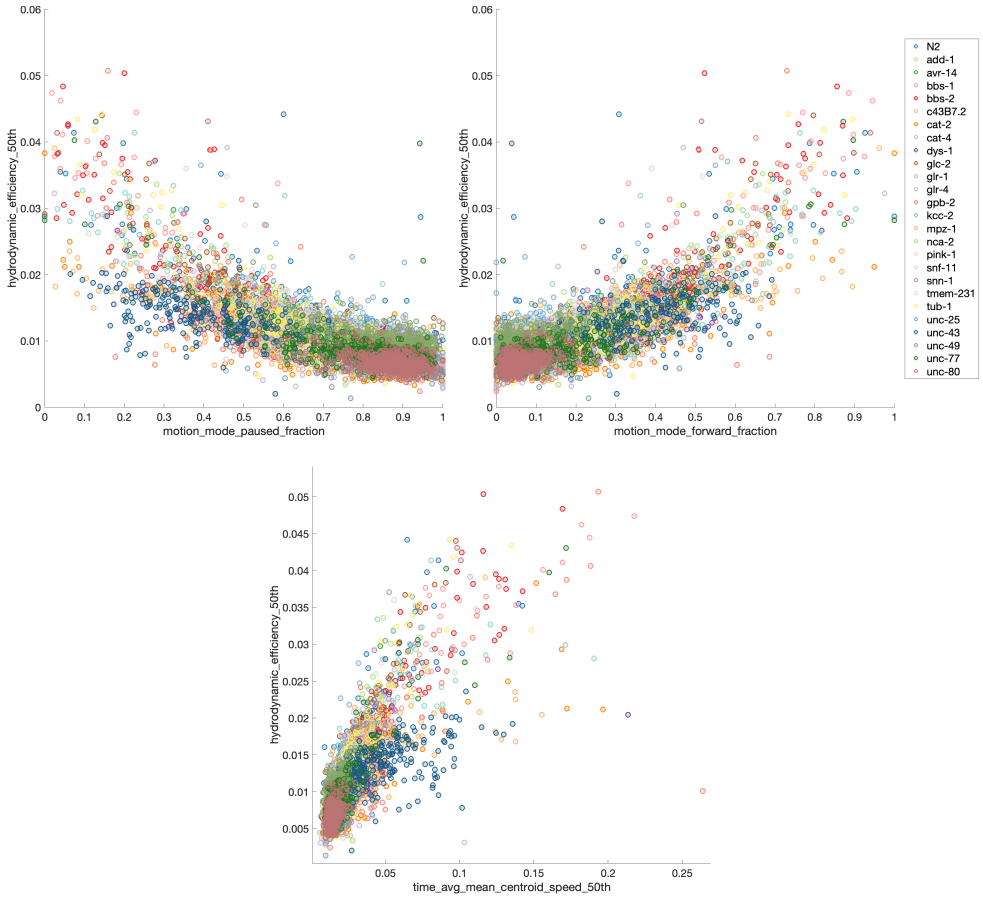

Figure 4.6: Scatter plots of median efficiency (*hydrodynamic_efficiency_50th*) against other features that are highly correlated. Each dot represents one well (ie each point corresponds to the well-averaged data). Median efficiency is strongly correlated with the fraction of time worms spend paused — *motion_mode_paused_fraction* ($r = -0.755$), as well as the fraction of time worms spend moving forward — *motion_mode_forward_fraction* ($r = 0.783$), and median time-averaged normalised centroid speed — *time_avg_mean_centroid_speed_50th* ($r = 0.775$).

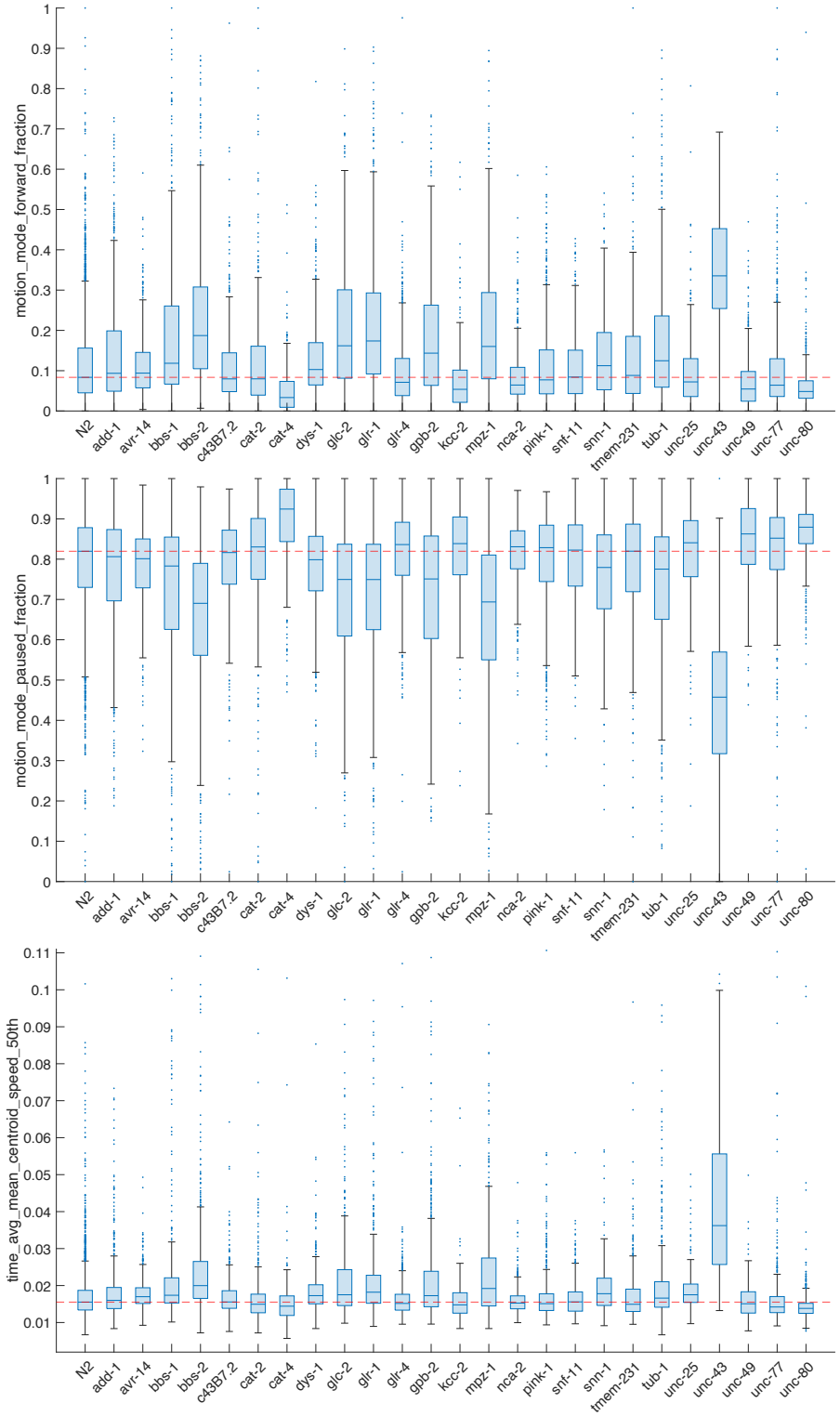

Figure 4.7: Boxplots of the features *motion_mode_foward_fraction*, *motion_mode_paused_fraction*, and *time_avg_mean_centroid_speed_50th* across the full disease model screening, which are all highly correlated with median efficiency measured.

Efficiency is lowest when worms are paused

To explain the overall efficiency results, we note that efficiency is lower when worms are paused compared with when they are moving forwards or backwards, as shown in fig. 4.8. When worms are moving, the measured efficiency is higher. Worms that spend more time paused (ie have relatively high *motion_mode_paused_fraction*) therefore spend more time incurring a lower efficiency, resulting in a lower efficiency overall.

For example, N2 and *bbs-2* have comparable distributions across the *hydrodynamic_efficiency_w_backward/forward/paused_50th* features (see fig. 4.9), but *bbs-2* has overall higher efficiency, due to having lower *motion_mode_paused_fraction* (and higher overall *motion_mode_forward_fraction*). We observe this effect evidently by looking at the worm skeletons themselves. Figure 4.10 shows the sequence of body postures of N2 worms and *bbs-2* worms, taken from six different wells on the same imaging plate. Paused efficiency is lower than not-paused efficiency across all wells. All of paused, forward, and backward efficiency respectively are comparable between the two strains.

So in general, lower *motion_mode_paused_fraction* implies higher efficiency — this is the case for *avr-14*, *bbs-1*, *bbs-2*, *glc-2*, *mpz-1*, *snn-1*, *tub-1*, *unc-43*. And vice versa, higher *motion_mode_paused_fraction* implies lower efficiency — see *cat-2*, *cat-4*, *glr-4*, *nca-2*, *pink-1*, *unc-25*, *unc-77*, *unc-80*.

There are however some exceptions to this trend: *kcc-2* and *unc-49* have higher *motion_mode_paused_fraction* but higher efficiency than N2. And *add-1*, *dys-1* and *snf-11* have lower *motion_mode_paused_fraction* but lower efficiency than N2.

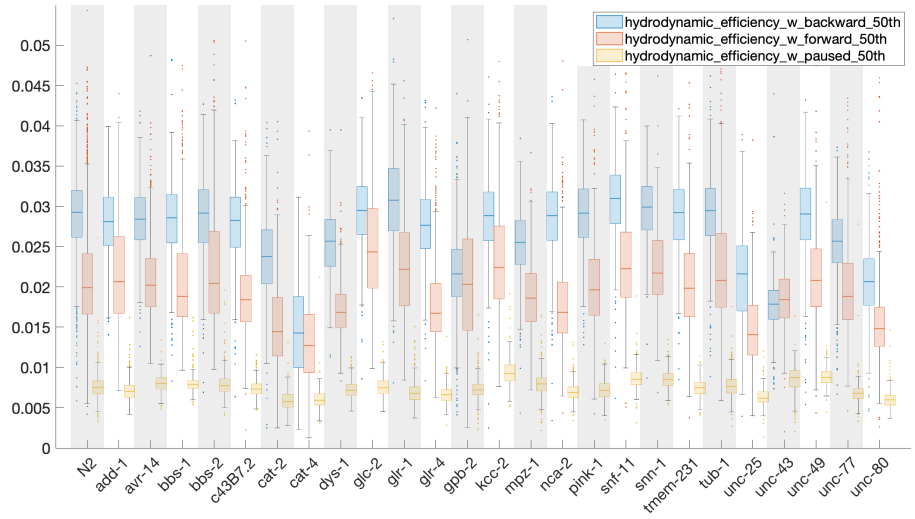

Figure 4.8: Boxplot of median efficiency across all strains separated by motion mode (backward, forward, paused). Efficiency is substantially lower when worms are paused compared with not. Efficiency for backwards locomotion is greater than for forwards, with the exception of *unc-43*.

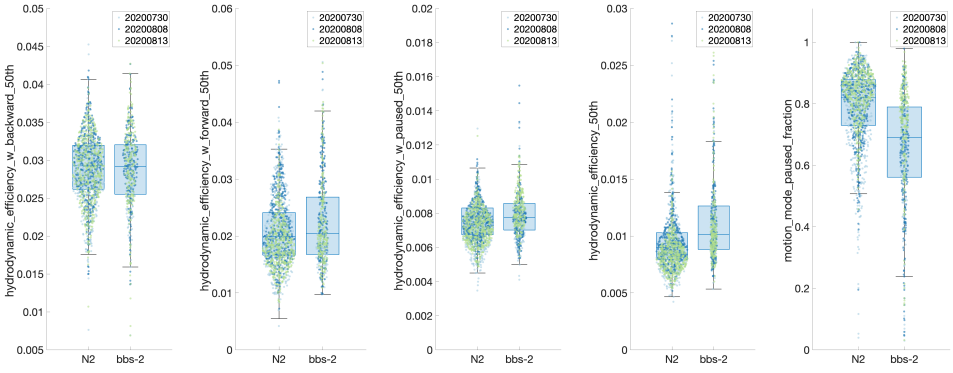

Figure 4.9: Boxplots: efficiency of *bbs-2* compared with N2, for median η_H overall, and separated by motion mode (backward, forward, paused). N2 and *bbs-2* have comparable distributions (similar median and quartile values) for the efficiency measures separated by motion mode. However, *bbs-2* has overall higher efficiency, as it spends less time paused compared with N2 (has lower *motion_mode_paused_fraction*).

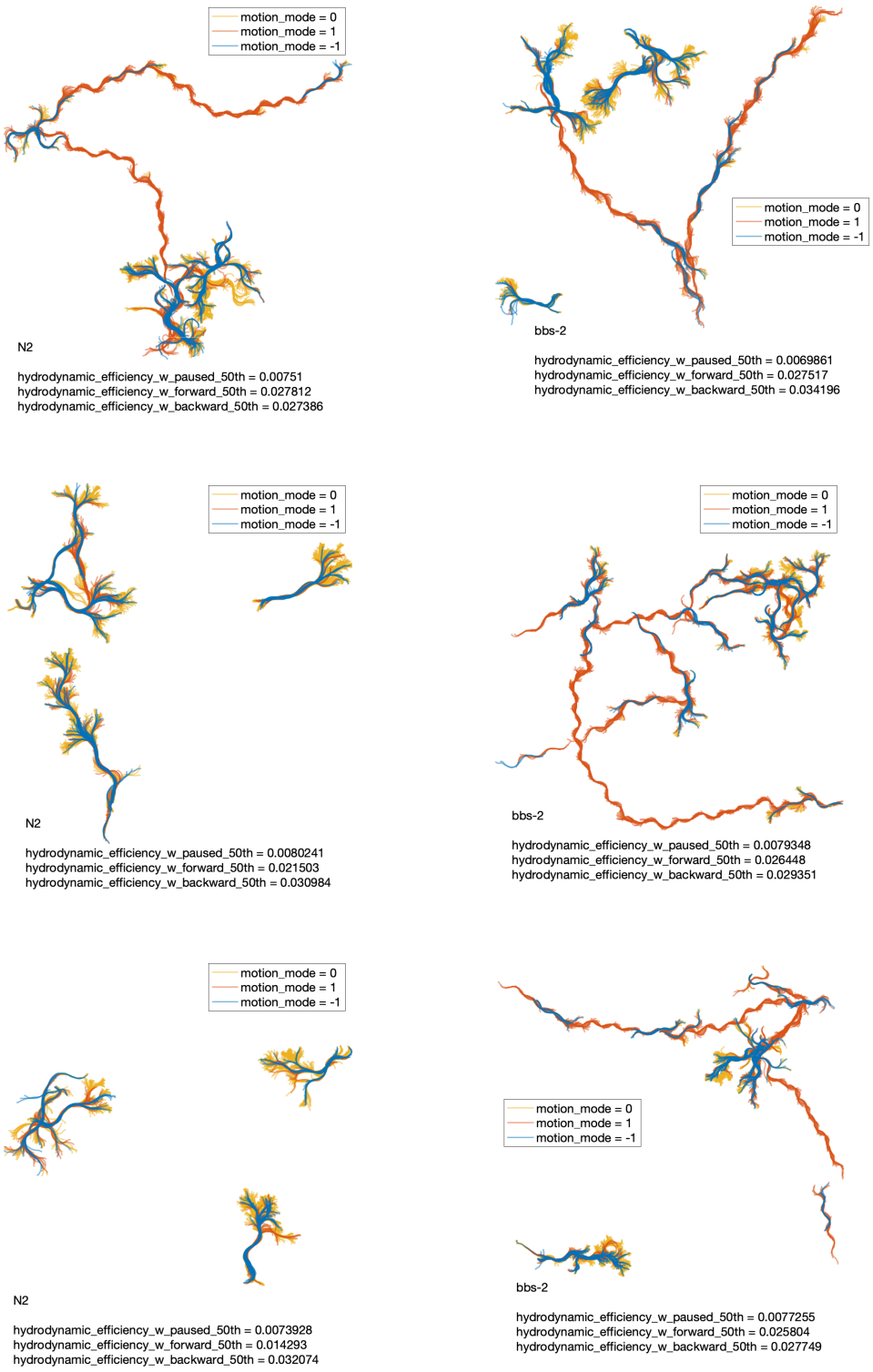

Figure 4.10: Worm skeletons (sequence of body postures) for N2 (left) and *bbs-2* (right) worms, every 10th frame shown. Taken from six different wells from the same imaging plate, ie date, time and stimulus invariant. Skeleton colour indicates paused, forward, or backward locomotion (*motion_mode* $= 0$, 1, or -1 respectively).

Efficiency when worms are paused is lower than when moving for several reasons. Firstly, the worm centroid speed is naturally lower when it is paused, as shown in fig. 4.11. In addition to this, the worms still incur a noteworthy mechanical work cost (increased dissipation), due to the presence of movements in the body despite being paused. Specifically, when worms are paused they continue to explore their environment by swinging their heads, for the purposes of foraging (a behaviour that has been widely observed and investigated [120]. This is observed in our data by inspecting the sequences of skeletons for paused worms. The head-swinging whilst paused can be seen in the N2 and *bbs-2* worms in fig. 4.10. Furthermore, fig. 4.12 compares the motion of specifically paused N2 worms with paused *kcc-2* worms. The distinctive head-swinging behaviour is clearly exhibited by N2, and incurs a high *time_avg_head_viscous_dissipation* relative to *kcc-2*. The sequence of *kcc-2* postures exhibit noticeably less head-swinging. Thus, the head (and overall) dissipation is lower, resulting in a higher efficiency.

Furthermore, we can separate both dissipation and head dissipation into backwards, forwards, and paused motion modes (see fig. 4.13). We see that, overall, dissipation is lower when worms are paused than when they are not. This is likely due to the fact that most of the body (namely the tail and midbody) is near-stationary during pauses. However, paused head dissipation is not as substantially reduced than paused total dissipation (relative to non-paused worms). This further explains why efficiency is low for paused worms, and aligns with the wide-ranging observation that the head is the most active part of the worm.

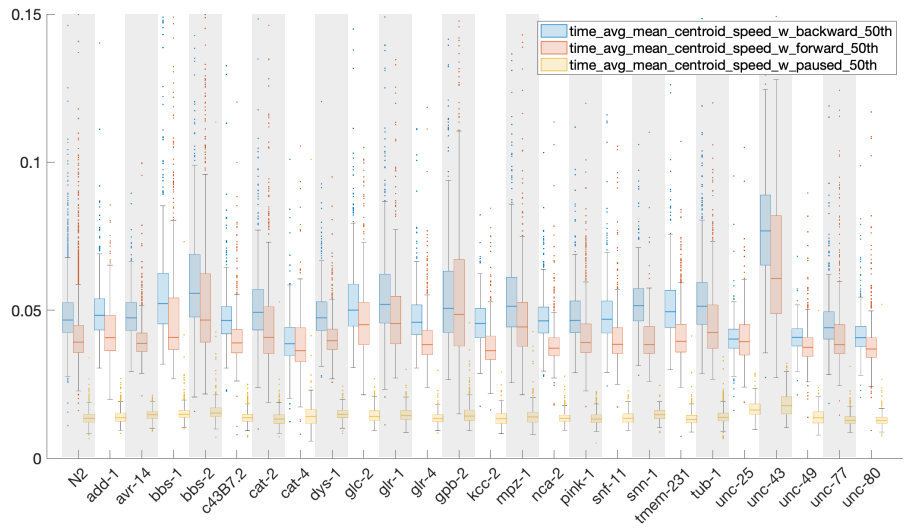

Figure 4.11: Boxplot of median time-averaged normalised centroid speed across all strains separated by motion mode (backward, forward, paused). Centroid speed is, naturally, lower when worms are paused.

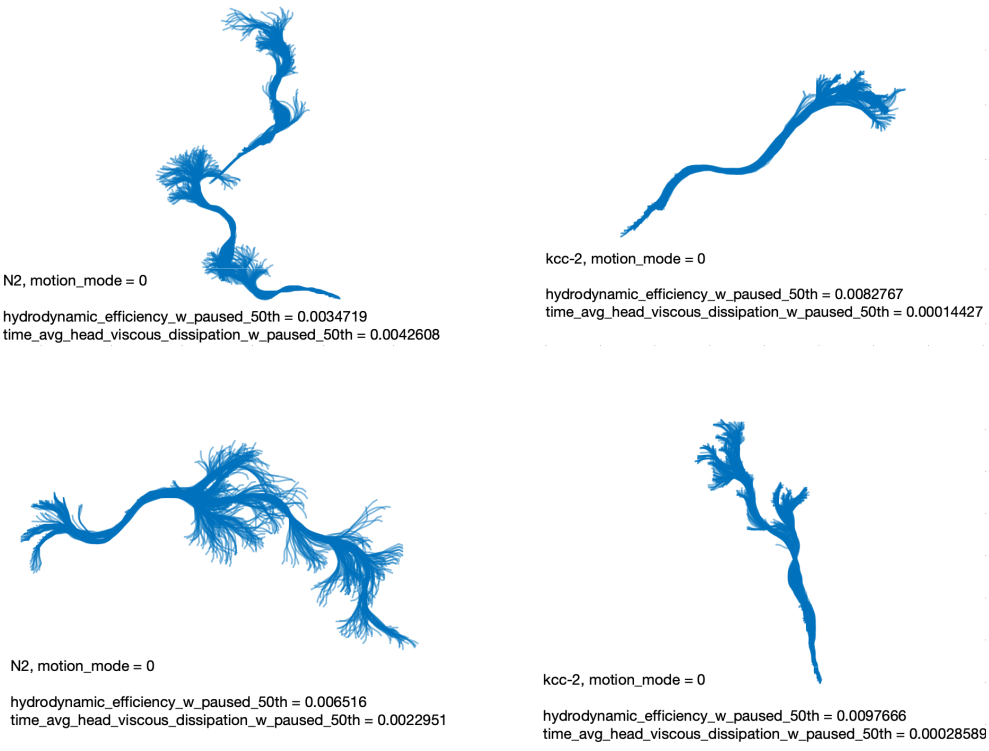

Figure 4.12: Example N2 (right) versus *kcc-2* (left) worm skeletons tracked by Tierpsy. Only paused skeletons (*motion_mode* = 0), and every 10th frame shown. The *kcc-2* worms exhibit less head-swinging than N2 when paused, resulting in a lower head dissipation for this motion mode, and consequently higher efficiency when paused.

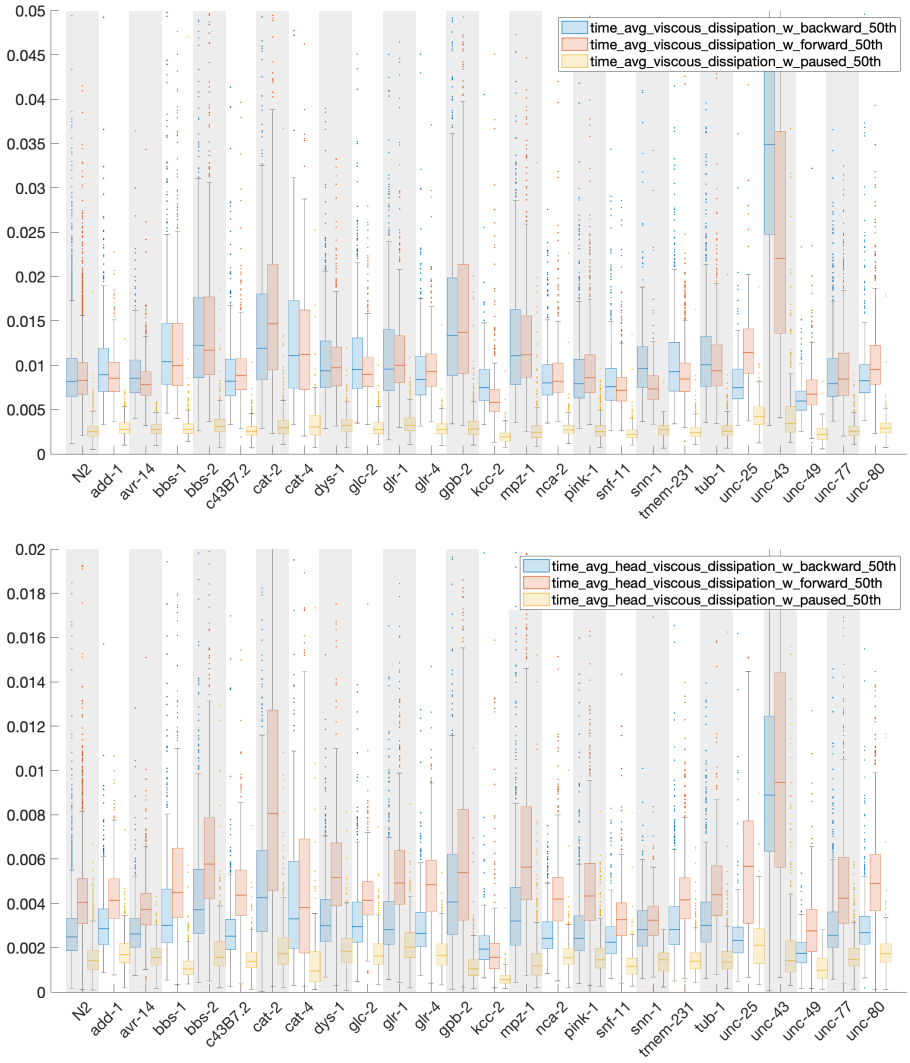

Figure 4.13: Boxplots of total dissipation and head dissipation across all strains separated by motion mode (backward, forward, paused). Dissipation is lower when worms are paused, but paused head dissipation is substantially less reduced than paused total dissipation (relative to non-paused worms). Axis truncated for ease of observation, omitting some outliers.

Efficiency is high for backward motion and reverals

We notice from fig. 4.8 that backward efficiency is consistently higher than forward efficiency, with the exception of only one strain: *unc-43*. This is because when reversing the worms centroid speed is also higher, ie worms are often moving backwards faster than they are moving forwards, as can be seen in fig. 4.11.

Worms often engage in backing motion and reversals when employing an escape response. In the escape response, they back away from an adverse stimulus quickly, resulting in a high centroid speed. Furthermore, head-swinging is suppressed in an escape response. In their natural environment, suppressing head swinging when reversing in response to adverse stimulus is key to survival, for example when encountering predacious fungi [121]. Predacious fungi can catch and trap nematodes by using constricting rings, which close around the worm when stimulated by friction, in order to then penetrate the cuticle and digest the worm. Suppressing head swinging to minimise the friction when reversing maximises the chance of successful retraction and evasion of capture. This ecologically relevant behaviour can be seen in fig. 4.13, in which head dissipation is lower for backward motion than forward. We also observe this behaviour by again inspecting worm body postures during backwards motion. Minimal head-swinging during reversals can be seen in fig. 4.10. More specifically, fig. 4.14 shows examples of N2 worms specifically reversing, exhibiting suppressed head-swinging for this motion mode. The backward head dissipation (and overall dissipation) is minimised, resulting in a high efficiency for reversals.

These skeletons are compared with those of *unc-43*, the strain that has the highest head dissipation for backward motion (and the only strain that has backward efficiency lower than forward efficiency — see fig. 4.8). The *unc-43* head motion in these examples is visibly greater than that of N2, resulting in its increased dissipation and thus lower backward efficiency.

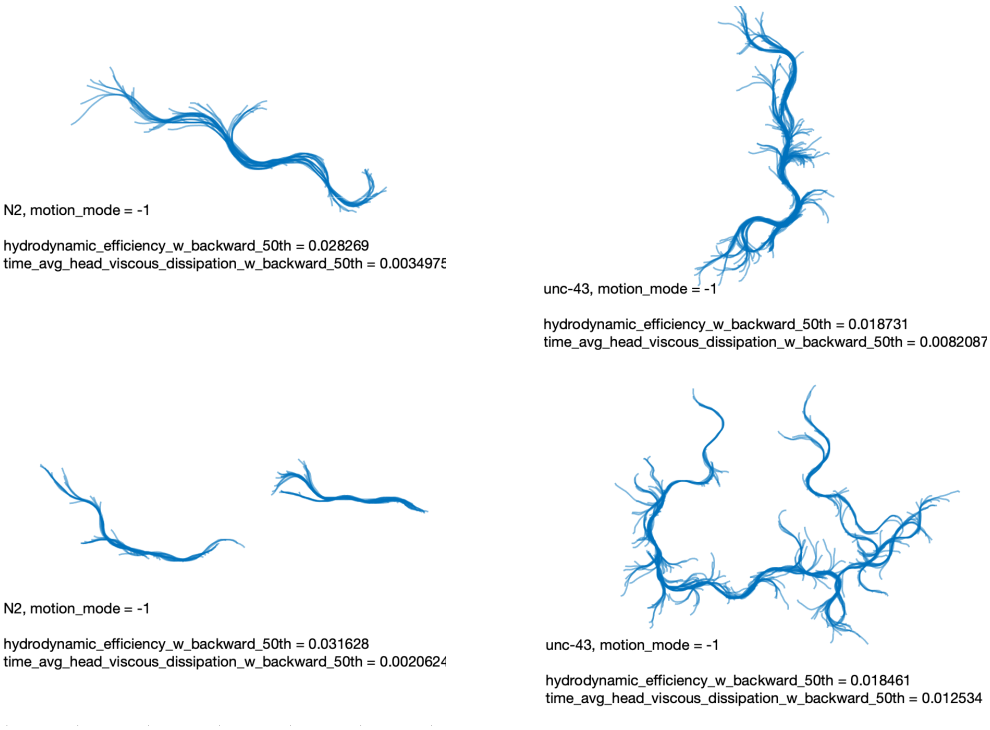

Figure 4.14: Example N2 (right) and *unc-43* (left) worm skeletons for backward motion (*motion_mode* $= -1$), every 10th frame shown. N2 worms exhibit suppressed head motion during backward motion, as a function of effective escape response. This results in reduced dissipation, and higher efficiency when these worms are reversing. The *unc-43* strain exhibits the highest head dissipation for backward motion across all strains, and visibly swings its head more than N2 when reversing.

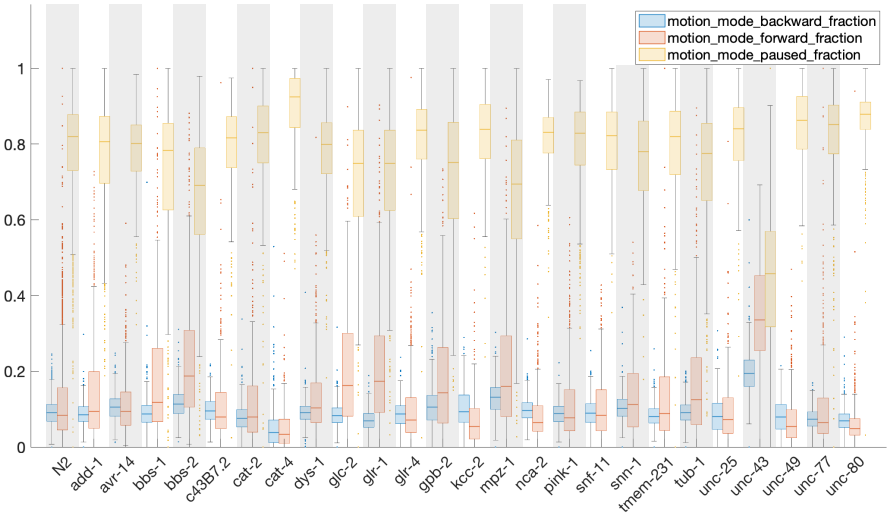

Figure 4.15: Boxplot of motion mode fraction across all strains (backward, forward, paused). All strains consistently spend more time paused than moving forward or backward.

unc-43

In addition to observing increased head swinging during reversals, is is interesting to see from the sequence of body postures in fig. 4.14 that the backing motion of *unc-43* is sustained for substantially longer than that of N2. In fact, it is the case that *unc-43* has a higher *motion_mode_backward_fraction* than any other strain (shown in fig. 4.15).

unc-43 stands out in these results as it has the highest measure of overall efficiency across all strains (see fig. 4.5). Additionally, its centroid speed is the highest across all strains for all motion modes (see fig. 4.11). In particular, *unc-43*'s time-averaged centroid speed when paused is higher than all the other strains. Observing the sequence of body postures of *unc-43* when paused (*motion_mode* = 0), shown in fig. 4.16, we see that despite plotting only 'paused' frames, the *unc-43* worms appear to exhibit a rapid stop-start motion, frequently and rapidly switching between pauses and forwards locomotion. If the switching between paused and forwards occurs at a rate of less than one second (ie the time-averaging window employed for *time_avg* features), then this will result in an increase in time-averaged centroid speed when paused. This rapid switching between motion modes can in fact be seen in fig. 4.17, in which over the trajectory of the worm, the sequence of body postures changes from paused to forward to backwards in a small number of frames. This hyperactive phenotype has been historically observed in *unc-43* (Reiner *et al* (1999) [122]). The results for the strain *unc-43* provide a promising validation of efficiency as a useful phenotyping tool.

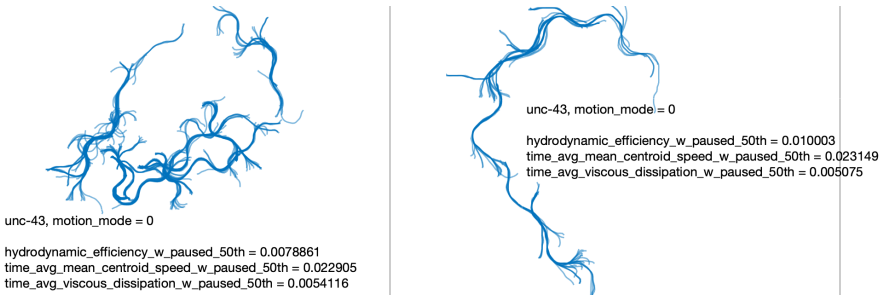

Figure 4.16: Example *unc-43* skeletons for paused motion (*motion_mode* = 0), every 10th frame shown. Translation between paused skeletons indicates that *unc-43* rapidly switches between paused and not-paused locomotion.

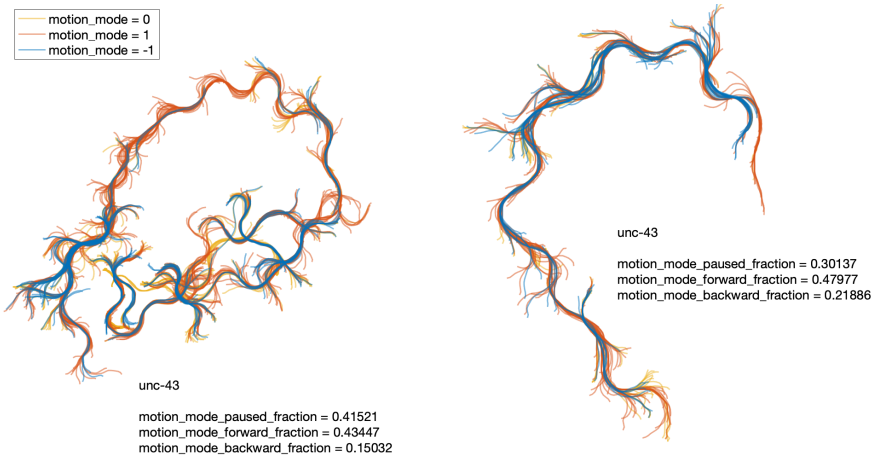

Figure 4.17: *unc-43* skeletons, every 10th frame shown. *unc-43* exhibits a rapid stop-start motion, frequently switching between paused and forward locomotion, yielding an increased time-averaged paused centroid speed

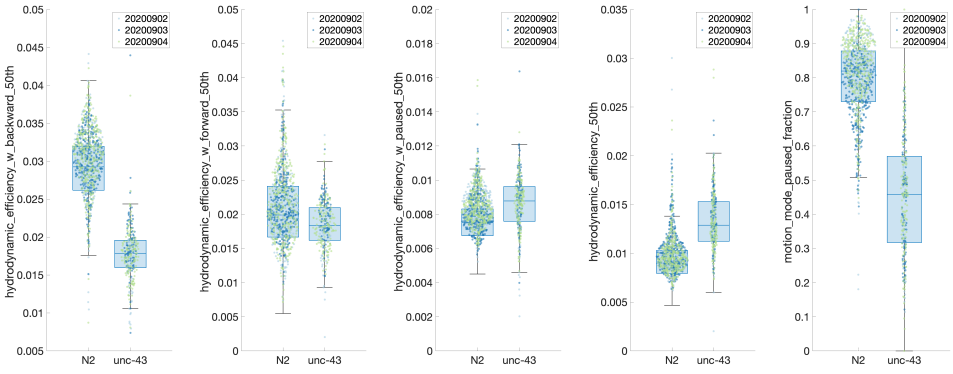

Figure 4.18: Boxplots: efficiency of *unc-43* compared with N2, overall and separated by motion mode (backward, forward, paused). *unc-43* has overall higher efficiency, as it spends significantly less time paused compared with N2 (has lower *motion_mode_paused_fraction*).

unc-43 has remarkably high overall efficiency due to its particularly small *motion_mode_paused_fraction* value — the lowest across all strains in the data (see fig. 4.15). Comparing specifically with N2 (see fig. 4.18), although *unc-43* shows lower forward and backward efficiency, it is more efficient when paused. This is due to its high paused centroid speed (discussed above), but also due to the fact that *unc-43* and N2 have the same head dissipation when paused ($p > 0.05$). Hence, *unc-43* has higher paused efficiency than N2, and is more efficient than N2 overall, because N2 is paused approximately 80% of the time and efficiency when paused is lower. The increased time N2 spends paused (incurring a lower efficiency) results in an overall lower efficiency measured.

Other epilepsy models

The *unc-43* strain has associated human diseases including intellectual disabilities and epilepsy. Specifically, the *unc-43* worms model epileptic seizures [123]. Other seizure models in epilepsy in the screening are the C43B7.2, *unc-25*, and *unc-49* worms [124–126]. *unc-49* also has a higher efficiency than N2, was found to be less active and generally slower, and in particular had lower dissipation than N2 across all motion modes, as well as lower head dissipation.

unc-25 and C43B7.2 worms were found to have significantly lower efficiency than N2. Like *unc-43*, *unc-25* also has a significantly greater time-averaged centroid speed and dissipation than N2. However, *unc-25* has significantly lower efficiency than N2 due to having a higher *motion_mode_paused_fraction*. C43B7.2 was found to have not significantly different centroid speed, dissipation, and *motion_mode_paused_fraction* compared to N2 ($p > 0.05$). It was found to have a marginally higher dissipation than N2 when paused and moving forward, resulting in its low relative efficiency.

The *kcc-2*, *snf-11*, and *snn-1* worms are also epilepsy models, specifically solute carrier and synapsin models of epilepsy. They are all found to be more effi-

cient than N2. *kcc-2* specifically has high efficiency when paused and moving forward, due to low head dissipation and in general low dissipation across all motion modes. This also applies to *snf-11*, which was additionally found to have indifferent centroid speed to N2 ($p > 0.05$ for all *time_avg_mean_centroid_speed* features). *snn-1* was found to be more active than N2, with a significantly lower *motion_mode_paused_fraction*.

Hypotonia and diminished neurotransmitter biosynthesis models have low hydrodynamic efficiency

The *nca-2*, *unc-77*, and *unc-80* worms are hypotonia models, and were all found to be less efficient than N2, due to either diminished centroid speed, or increased dissipation. The *gpb-2* worms are also associated with hypotonia (amongst a number of other disorders), and were found to have overall not significantly different efficiency from N2, despite having significantly higher dissipation, and also significantly higher centroid speed.

The *cat-2* and *cat-4* worms have associated human diseases of Segawa syndrome and Dystonia respectively, which are both disorders of diminished neurotransmitter biosynthesis. Both of these strains were found to have lower efficiency than N2, with both exhibiting significantly slower centroid speed, and *cat-2* exhibiting high dissipation.

Trends across other human disease association groups

gpb-2 worms are also associated with intellectual disabilities. Other intellectual disability models are *glr-1*, *glr-4*, and *add-1* worms. The *glr-1* strain were found to be significantly different from N2 in all features obtained apart from median efficiency. In particular, *glr-1* have significantly higher centroid speed, and significantly higher dissipation than N2. The *glr-4* strain is less efficient than N2 due

to having higher dissipation. *add-1* worms are less efficient than N2, also having higher dissipation, and marginally higher centroid speed.

Strains that model ciliopathies — disorders associated with genetic mutations encoding defective proteins, resulting in abnormal formation or function of cilia — (*bbs-2*, *bbs-1*, *tub-1*, and *tmem-231*) were generally found to be more efficient than N2, with higher centroid speeds, higher dissipation, and lower motion mode paused fraction. The hyperekplexia (startle disease) model strains — *avr-14* and *glc-2* — are both more efficient than N2, with higher centroid speed, higher dissipation, and lower motion mode paused fraction. Strains that model neurodegenerative disorders (*dys-1* and *pink-1*) were both found to be less efficient than N2.

4.5 Conclusion

4.5.1 Summary

We have analysed the results of expanding the current set of behavioural phenotypes to include features that quantify *C. elegans* gait optimality, with the aim of detecting a broader spectrum of movement defects. The quantitative gait optimality phenotypes employ tools from low Reynolds number hydrodynamics and resistive force theory, which has extensively been shown to provide effective empirical frameworks for modelling *C. elegans* locomotion. The gait efficiency of a given worm is defined as the ratio of speed to rate of mechanical work (equivalently dissipation), multiplied by the ratio of tangential to normal resistance coefficients (the drag anisotropy).

We tested these phenotypes in the context of a rare human genetic disease models screen. The types of human disease modelled in our experiment included: epilepsy, hypotonia, diminished neurotransmitter biosynthesis, intellectual disabilities, and neurodegenerative disorders. Of the 25 strains analysed, 22 were found to have statistically significantly different average efficiency compared with N2 worms. Investigating trends in the results, we found that this feature was highly correlated with the fraction of time worms spend moving forwards (or paused), and also the worm's average centroid speed.

Efficiency was overall found to be lower when worms are paused compared with when they are moving. This is due to the naturally decreased centroid speed, as well as the presence of head-swinging motions which incur a mechanical work cost. Strains with suppressed head-swinging (such as *kcc-2*) were found to be more optimal when paused than N2.

Furthermore, efficiency was found to be generally high during reversals, when the worms engaged in backing motion. This is explained by the relatively in-

creased speed (the worms often reverse quickly), and also the suppression of head-swinging when reversing. This combination has ecological relevance in the *C. elegans* escape response to predacious fungi (a situation that intuitively demands efficient motion), suggesting that this behaviour has evolved due to selection. The overall findings that efficiency is generally low during pauses and generally high during reversals make sense in retrospect, and these are uncovered by our investigation.

One strain in particular — *unc-43*, an epilepsy model — stood out as it attained the highest measured efficiency across all of the strains in the data. Furthermore, it is the only strain to exhibit higher forward efficiency than backward efficiency. This result was explained by investigating the hyperactivity exhibited by this strain, and discovering that it engages in rapid stop-start behaviour, switching frequently between the different motion modes. This hyperactivity lead to overall higher measured efficiency due to increased centroid speed, and also results in increased efficiencies separated by motion mode as the stop-start motion occurs at a frequency smaller than the one second period the time-averaged features are calculated over.

Other epilepsy models (both seizure and solute carrier) were mostly also found to have higher efficiency than N2, though not all strains were found to be categorically so. The hypotonia models were generally found to be less efficient than N2. Other trends across the disease types include: ciliopathies found to be more efficient than N2, and neurodegenerative disorder models found to be less efficient.

Evidently, it is not the case that N2 exhibits the highest 'efficiency' across the strains we have considered in this dataset. This can be attributed to characteristic movement behaviours exhibited by these wildtype worms: high motion mode paused fraction, and the motion of head swinging when paused.

4.5.2 Further considerations

We have shown that efficiency as a phenotyping tool is potentially useful for detecting differences in movement behaviours between worm strains. The results of this chapter indicate that, between the strains analysed here, quantitative differences in gait efficiency are found between individuals. Interpretability of behavioural features is a key aspect for possible usefulness, which makes efficiency a good candidate as a phenotyping lens. An alternative quantitative measure of efficiency that does not intrinsically penalise wildtype behaviours such as head-swinging when paused (a behaviour that is crucial for sensory and navigatory purposes), and generally stationary states could be devised to alternatively measure efficiency across strains. Such a measure could detect the highest efficiencies to be exhibited by wildtype worms.

The efficiency applied in this analysis did not account for or penalise any bending or high-curvature body postures, as the generalised efficiency used in Part I did. Including a penalty for bending in the body for the quantitative phenotype could provide suitable alternative measures of the efficiency. For this scenario, the relative importance of bending versus mechanical work (A_B) would need to be chosen to reflect the achievable radius of curvature of *C. elegans*, which could be context-specific, and would require more analysis. A possible alternative approach could be to estimate A_B from the value of the wavenumber, though this requires further consideration.

The time-averaged worm gait optimality features were calculated across one second windows in the tracking data. This window size was chosen to capture periods of worm locomotion under the assumption that categorical changes in movement behaviour occur at a rate above this. Alteration of the window size for calculating the time-averaged features could have significant effects on the relative efficiencies obtained across strains. Averaging over longer timescales could favour periods of sustained forward locomotion. Averaging over shorter timescales could

minimise distortions from rapid switching between motion modes, but may also be more sensitive to noise in the tracking data. Analysing the affects of time-averaging over different window sizes requires further investigation.

Recall that the tracking data was collected, after an initial 30 minute habituation period, according to: 5 minutes pre-stimulus, followed by 6 minutes of blue light in which three 10 second blue light pulses occurred at 60, 160 and 260 seconds, followed by 5 minutes post-stimulus data, resulting in a total tracking period of 16 minutes. Investigating the effects of how gait efficiency changes depending on which stimulus stage the worms are at is another avenue for further consideration in this analysis. This could lend further insight into for instance gait efficiency specifically during escape response, by isolating only the blue light period from the data.

In calculating the gait efficiency from the sequences of worm body postures, in order to obtain the force per unit length of the body acting on the surroundings, and thus the rate of mechanical work exerted by the worm, we applied resistive force theory which provides effective empirical frameworks for *C. elegans* crawling models. By this theory, the force is scaled linearly with the velocity in both the tangential and normal directions, and therefore the ratio of tangential to normal resistance coefficients $r_k = K_T/K_N$ needs to be defined. In this analysis, we fixed $r_k = 1/10$ as the globally applied value, in order to model the force, mechanical work, and thus the efficiency.

This value was chosen based on experimental measurements by Rabets *et al* (2014) [34] and also values determined numerically by Keaveny and Brown (2017) [35]. The value of the efficiency is linearly proportional to the drag anisotropy, and to further justify our chosen fixed value here we could perform a linear stability analysis to assess the dependency of the efficiency on r_k. For instance, between N2 and the disease models, how much variation in r_k would result in for example all strains being equally efficient.

As discussed in the introduction, the value of r_k for different environments has been the subject of a number of studies. We chose to fix r_k and apply this as a global drag anisotropy, but studies have shown that drag forces do not scale linearly with velocity on gels. It could be the case that a global drag anisotropy cannot be defined in this context, and it may be more appropriate to apply r_k on a frame-by-frame basis. This could be done by finding the r_k which minimises the difference between the body translation recorded in the tracking data and the translation recovered via the change in body posture in the resistive force model (rigid body motion calculation). This approach was adopted in by Keaveny and Brown (2017) [35], though on a worm-by-worm basis as opposed to frame-by-frame. The resolution and amount of noise present in the data would require significant improvement for r_k to be inferred on a frame-by-frame basis. On a worm-by-worm case, it has been shown that some strains move with more slip than wildtype, due to mutations in genes affecting cuticle structure and function. The drag anisotropy for these worms would thus be lower than for N2. A similar optimisation approach to [35] could lead to different trends in the efficiency results between the strains analysed.

Efficiency as a phenotyping lens has the scope to be applied in a variety of contexts: from disease screens, to across different environments, or across other species of nematode. If the phenotype of low efficiency in disease model strains can be reversed over the course of drug treatment assay, this could lead to the identification of new or repurposed compounds to treat associated diseases in humans. Applying the phenotyping lens across different environments and across other nematode species has the possibility of lending insight into undulatory movement behaviours that, like the escape from predacious fungi, may also have evolved due to selective pressures. Further development of these tools therefore has the potential to uncover more about the overall nature of this model organism.

End of Part II

Chapter 5

Summary and outlook

This thesis has explored the avenue of efficient undulatory microorganism locomotion in two parts. Part I extended current theoretical and computational approaches to modelling optimal undulatory locomotion, which previously predominantly focused on straight-path forwards locomotion. We obtained optimal undulatory turning gait results by posing an optimisation problem which minimised the objective function describing the cost of motion, subject to the constraint that a fixed turning angle was achieved in one period. Multiple different parametrisations of the problem were investigated, and the optimal turning gait was found to depend on the relative weighting of mechanical work versus bending cost in the objective function. We established that optimal turning gaits from high-dimensional parameter spaces can be closely approximated as travelling waves of constant curvature.

Part II developed efficiency and gait optimality measures and tools for *C. elegans* behavioural phenotypic screens. This was done in the context of a human disease model screen, which comprised of mutant strains each associated with a rare genetic disease in humans. Efficiency successfully detected differences in movement behaviours between the strains in the data, yielding quantitatively distinct results between worms. Trends between disease types were uncovered, and further work

could lead to insight into how *C. elegans* movement behaviours may have evolved for efficiency.

Characteristic differences between *C. elegans* gait in different environments (eg swimming versus crawling), under the lens of quantitative efficiency phenotypes could reasonably result in the conclusion that *C. elegans* moves more efficiently when it is crawling on agar than when it is swimming in a fluid. For instance, it achieves greater displacement per body undulation when crawling than when swimming due to increased friction in the environment. This could shine a negative light on swimming worms: they are working really hard swimming and not moving very efficiently compared to when they are crawling on agar. However, it has been shown that swim exercise in *C. elegans* actually extends healthspan and protects against degeneration [127–129]. So whilst swimming may seem inefficient compared with crawling, it is arguably good for them if it improves their quality of life.

To marry the results obtained from the distinct parts of this thesis, it could be possible to investigate the efficiency or optimality of *C. elegans* undulatory turning gaits. The well-known omega-turn is widely observed and characterised in the literature, and isolating points of high path curvature in the tracking data could provide a suitable dataset in order to test our optimal turning models. Modelling the capacity of turning versus the efficiency of swimming are two potentially competing ideas. There may be, biologically, a combination of the two that matters, and these two ideas in nature are tightly linked with each other, and also with the overarching aim of efficiency for survival. To combine models of optimal turning with efficient swimming or crawling, a mixed model or decision-making model which decides to switch between these two objectives every so often may be the best solution. To form this kind of model, choices need to be made within the framework about the objective function (potentially a multi-objective framework would be optimal), and also the shape space. Based on these choices, the resulting parametrisation of the model that can then be compared to data and biological

insights. The parameters in the model should be directly measurable or inferable from the biological data, and describe particular phenomena. The set of extractable parameters from data is dictated by the specifics of experimental setup, but the optimal gaits would thus be a function of the parameters in the model. Ultimately, our main outlook is considering how to expressly connect biological data with the theoretical models.

Bibliography

[1] P. Liao, L. Xing, S. Zhang, and D. Sun, "Magnetically Driven Undulatory Microswimmers Integrating Multiple Rigid Segments," *Small*, vol. 15, p. 1901197, Sept. 2019.

[2] R. D. Maladen, Y. Ding, P. B. Umbanhowar, and D. I. Goldman, "Undulatory swimming in sand: experimental and simulation studies of a robotic sandfish," *The International Journal of Robotics Research*, vol. 30, pp. 793–805, June 2011.

[3] F. Schwab, F. Wiesemuller, C. Mucignat, Y.-L. Park, I. Lunati, M. Kovac, and A. Jusufi, "Undulatory Swimming Performance Explored With a Biorobotic Fish and Measured by Soft Sensors and Particle Image Velocimetry," *Frontiers in Robotics and AI*, vol. 8, p. 791722, Jan. 2022.

[4] J. G. White, E. Southgate, J. N. Thomson, and S. Brenner, "The structure of the nervous system of the nematode *Caenorhabditis elegans*," *Philosophical Transactions of the Royal Society of London. B, Biological Sciences*, vol. 314, pp. 1–340, Nov. 1986.

[5] S. J. Cook, T. A. Jarrell, C. A. Brittin, Y. Wang, A. E. Bloniarz, M. A. Yakovlev, K. C. Q. Nguyen, L. T.-H. Tang, E. A. Bayer, J. S. Duerr, H. E. Bulow, O. Hobert, D. H. Hall, and S. W. Emmons, "Whole-animal connectomes of both Caenorhabditis elegans sexes," *Nature*, vol. 571, pp. 63–71, July 2019.

[6] E. M. Jorgensen and S. E. Mango, "The art and design of genetic screens: Caenorhabditis elegans," *Nature Reviews Genetics*, vol. 3, pp. 356–369, May 2002.

[7] R. S. Shapiro, A. Chavez, and J. J. Collins, "CRISPR-based genomic tools for the manipulation of genetically intractable microorganisms," *Nature Reviews Microbiology*, vol. 16, pp. 333–339, June 2018.

[8] J. Gray and G. J. Hancock, "The Propulsion of Sea-Urchin Spermatozoa," *Journal of Experimental Biology*, vol. 32, pp. 802–814, Dec. 1955.

[9] J. Lighthill, *Mathematical biofluiddynamics*. No. 17 in CBMS-NSF regional conference series in applied mathematics, Philadelphia: Society for Industrial and Applied Mathematics, 1975.

[10] A. Javer, L. Ripoll-Sa'nchez, and A. E. X. Brown, "Powerful and interpretable behavioural features for quantitative phenotyping of Caenorhabditis elegans," *Philosophical Transactions B*, vol. 373, Oct. 2018.

[11] A. Javer, M. Currie, C. W. Lee, J. Hokanson, K. Li, C. N. Martineau, E. Yemini, L. J. Grundy, C. Li, Q. Ch'ng, W. R. Schafer, E. A. A. Nollen, R. Kerr, and A. E. X. Brown, "An open-source platform for analyzing and sharing worm-behavior data," *Nature Methods*, vol. 15, pp. 645–646, Sept. 2018.

[12] S. E. Spagnolie and E. Lauga, "The optimal elastic flagellum," *Physics of Fluids*, vol. 22, p. 031901, Mar. 2010.

[13] G. I. Taylor, "Analysis of the swimming of microscopic organisms," *Proceedings of the Royal Society of London. Series A. Mathematical and Physical Sciences*, vol. 209, pp. 447–461, Nov. 1951.

[14] G. J. Hancock, "The self-propulsion of microscopic organisms through liquids," *Proceedings of the Royal Society of London. Series A. Mathematical and Physical Sciences*, vol. 217, pp. 96–121, Mar. 1953.

[15] J. Gray and H. W. Lissmann, "The Locomotion of Nematodes," *Journal of Experimental Biology*, vol. 41, pp. 135–154, Mar. 1964.

[16] H. R. Wallace, "The Dynamics of Nematode Movement," *Annual Review of Phytopathology*, vol. 6, pp. 91–114, Sept. 1968.

[17] O. Pironneau and D. F. Katz, "Optimal swimming of flagellated micro-organisms," *Journal of Fluid Mechanics*, vol. 66, pp. 391–415, Nov. 1974.

[18] S. Camalet and F. Julicher, "Generic aspects of axonemal beating," *New Journal of Physics*, vol. 2, p. 324, Oct. 2000.

[19] I. H. Riedel-Kruse, A. Hilfinger, J. Howard, and F. Julicher, "How molecular motors shape the flagellar beat," *HFSP Journal*, vol. 1, pp. 192–208, Sept. 2007.

[20] L. D. Landau, L. P. Pitaevskii, A. M. Kosevich, and E. M. Lifshitz, *Theory of Elasticity*, vol. 7. Elsevier, 3 ed., 1984.

[21] E. Lauga and C. Eloy, "Shape of optimal active flagella," *Journal of Fluid Mechanics*, vol. 730, pp. R1–1 to R1–11, Sept. 2013.

[22] E. Lauga, "Traveling waves are hydrodynamically optimal for long-wavelength flagella," *Physical Review Fluids*, vol. 5, p. 123101, Dec. 2020.

[23] S. Childress, *Mechanics of Swimming and Flying*. Cambridge University Press, July 1981.

[24] E. M. Purcell, "Life at low Reynolds number," *American Journal of Physics*, vol. 45, pp. 3–11, Jan. 1977.

[25] E. Lauga, "Life around the scallop theorem," *Soft Matter*, vol. 7, pp. 3060–3065, Apr. 2011.

[26] J. Lighthill, "Flagellar Hydrodynamics," *SIAM Review*, vol. 18, pp. 161–230, Apr. 1976.

[27] N. Cohen and J. H. Boyle, "Swimming at low Reynolds number: a beginners guide to undulatory locomotion," *Contemporary Physics*, vol. 51, pp. 103–123, Mar. 2010.

[28] E. Lauga and T. R. Powers, "The hydrodynamics of swimming microorganisms," *Reports on Progress in Physics*, vol. 72, p. 096601, Sept. 2009.

[29] J. B. Keller and S. I. Rubinow, "Slender-body theory for slow viscous flow," *Journal of Fluid Mechanics*, vol. 75, pp. 705–714, June 1976.

[30] R. E. Johnson, "An improved slender-body theory for Stokes flow," *Journal of Fluid Mechanics*, vol. 99, pp. 411–431, July 1980.

[31] R. Johnson and C. Brokaw, "Flagellar hydrodynamics. A comparison between resistive-force theory and slender-body theory," *Biophysical Journal*, vol. 25, pp. 113–127, Jan. 1979.

[32] S. Berri, J. H. Boyle, M. Tassieri, I. A. Hope, and N. Cohen, "Forward locomotion of the nematode C. elegans is achieved through modulation of a single gait," *HFSP Journal*, vol. 3, pp. 186–193, June 2009.

[33] T. Majmudar, E. E. Keaveny, J. Zhang, and M. J. Shelley, "Experiments and theory of undulatory locomotion in a simple structured medium," *Journal of The Royal Society Interface*, vol. 9, pp. 1809–1823, Aug. 2012.

[34] Y. Rabets, M. Backholm, K. Dalnoki-Veress, and W. S. Ryu, "Direct Measurements of Drag Forces in C. elegans Crawling Locomotion," *Biophysical Journal*, vol. 107, pp. 1980–1987, Oct. 2014.

[35] E. E. Keaveny and A. E. X. Brown, "Predicting path from undulations for *C. elegans* using linear and nonlinear resistive force theory," *Physical Biology*, vol. 14, p. 025001, Mar. 2017.

[36] C. J. Brokaw, "Non-Sinusoidal Bending Waves of Sperm Flagella," *Journal of Experimental Biology*, vol. 43, pp. 155–169, Aug. 1965.

[37] C. B. Lindemann and K. A. Lesich, "Flagellar and ciliary beating: the proven and the possible," *Journal of Cell Science*, vol. 123, pp. 519–528, Feb. 2010.

[38] A. K. Corsi, B. Wightman, and M. Chalfie, "A Transparent window into biology: A primer on Caenorhabditis elegans," June 2015.

[39] M. A. Sleigh, *Cilia and flagella*. London, New York: Academic Press, 1974.

[40] C. Omoto and C. Brokaw, "Structure and behaviour of the sperm terminal filament," *Journal of Cell Science*, vol. 58, pp. 385–409, Dec. 1982.

[41] F. Gittes, B. Mickey, J. Nettleton, and J. Howard, "Flexural rigidity of microtubules and actin filaments measured from thermal fluctuations in shape," *Journal of Cell Biology*, vol. 120, pp. 923–934, Feb. 1993.

[42] C. Duprat and H. Stone, eds., *Fluid-Structure Interactions in Low-Reynolds-Number Flows*. Soft Matter Series, Cambridge: Royal Society of Chemistry, 2015.

[43] H. Wallace, "Wave Formation By Infective Larvae of the Plant Parasitic Nematode Meloidogyne Javanica," *Nematologica*, vol. 15, no. 1, pp. 65–75, 1969.

[44] N. A. Croll, "Components and patterns in the behaviour of the nematode *Caenorhabditis elegans*," *Journal of Zoology*, vol. 176, pp. 159–176, June 1975.

[45] N. A. Croll, "Behavioural Analysis of Nematode Movement," in *Advances in Parasitology*, vol. 13, pp. 71–122, Elsevier, 1975.

[46] J. T. Pierce-Shimomura, T. M. Morse, and S. R. Lockery, "The Fundamental Role of Pirouettes in *Caenorhabditis elegans* Chemotaxis," *The Journal of Neuroscience*, vol. 19, pp. 9557–9569, Nov. 1999.

[47] W. S. Ryu and A. D. T. Samuel, "Thermotaxis in *Caenorhabditis elegans* Analyzed by Measuring Responses to Defined Thermal Stimuli," *The Journal of Neuroscience*, vol. 22, pp. 5727–5733, July 2002.

[48] H. A. Zariwala, A. C. Miller, S. Faumont, and S. R. Lockery, "Step Response Analysis of Thermotaxis in *Caenorhabditis elegans*," *The Journal of Neuroscience*, vol. 23, pp. 4369–4377, May 2003.

[49] L. Luo, D. A. Clark, D. Biron, L. Mahadevan, and A. D. T. Samuel, "Sensorimotor control during isothermal tracking in *Caenorhabditis elegans*," *Journal of Experimental Biology*, vol. 209, pp. 4652–4662, Dec. 2006.

[50] T. Wakabayashi, I. Kitagawa, and R. Shingai, "Neurons regulating the duration of forward locomotion in Caenorhabditis elegans," *Neuroscience Research*, vol. 50, pp. 103–111, Sept. 2004.

[51] J. M. Gray, J. J. Hill, and C. I. Bargmann, "A circuit for navigation in *Caenorhabditis elegans*," *Proceedings of the National Academy of Sciences*, vol. 102, pp. 3184–3191, Mar. 2005.

[52] W. R. Schafer, "Deciphering the Neural and Molecular Mechanisms of C. elegans Behavior," *Current Biology*, vol. 15, pp. R723–R729, Sept. 2005.

[53] D. Kim, S. Park, L. Mahadevan, and J. H. Shin, "The shallow turn of a worm," *Journal of Experimental Biology*, vol. 214, pp. 1554–1559, May 2011.

[54] S. Kohannim and T. Iwasaki, "Optimal turning gait for undulatory locomotion," in *2012 American Control Conference (ACC)*, (Montreal, QC), pp. 3459–3464, IEEE, June 2012.

[55] S. Kohannim and T. Iwasaki, "Optimal turning gait for mechanical rectifier systems with three dimensional motion," in *53rd IEEE Conference on Decision and Control*, (Los Angeles, CA, USA), pp. 5862–5867, Dec. 2014.

[56] S. Kohannim and T. Iwasaki, "Dynamical Model and Optimal Turning Gait for Mechanical Rectifier Systems," *IEEE Transactions on Automatic Control*, vol. 62, pp. 682–693, Feb. 2017.

[57] S. Alben, "Optimizing snake locomotion in the plane," *Proceedings of the Royal Society A: Mathematical, Physical and Engineering Sciences*, vol. 469, p. 20130236, Nov. 2013.

[58] T. A. Driscoll, N. Hale, and L. N. Trefethen, "Chebfun Guide," 2014.

[59] S. Brenner, "The genetics of Caenorhabditis elegans," *Genetics*, vol. 77, pp. 71–94, May 1974.

[60] The C. elegans Sequencing Consortium, "Genome Sequence of the Nematode *C. elegans* : A Platform for Investigating Biology," *Science*, vol. 282, pp. 2012–2018, Dec. 1998.

[61] E.-Z. Shen, C.-Q. Song, Y. Lin, W.-H. Zhang, P.-F. Su, W.-Y. Liu, P. Zhang, J. Xu, N. Lin, C. Zhan, X. Wang, Y. Shyr, H. Cheng, and M.-Q. Dong, "Mitoflash frequency in early adulthood predicts lifespan in Caenorhabditis elegans," *Nature*, vol. 508, pp. 128–132, Apr. 2014.

[62] K. P. Yuet, M. K. Doma, J. T. Ngo, M. J. Sweredoski, R. L. J. Graham, A. Moradian, S. Hess, E. M. Schuman, P. W. Sternberg, and D. A. Tirrell, "Cell-specific proteomic analysis in *Caenorhabditis elegans*," *Proceedings of the National Academy of Sciences*, vol. 112, pp. 2705–2710, Mar. 2015.

[63] J. S. Packer, Q. Zhu, C. Huynh, P. Sivaramakrishnan, E. Preston, H. Dueck, D. Stefanik, K. Tan, C. Trapnell, J. Kim, R. H. Waterston, and J. I. Murray, "A lineage-resolved molecular atlas of *C. elegans* embryogenesis at single-cell resolution," *Science*, vol. 365, p. eaax1971, Sept. 2019.

[64] J. J. H. Liang, I. A. McKinnon, and C. H. Rankin, "The contribution of *C. elegans* neurogenetics to understanding neurodegenerative diseases," *Journal of Neurogenetics*, vol. 34, pp. 527–548, Oct. 2020.

[65] P. Davis, M. Zarowiecki, V. Arnaboldi, A. Becerra, S. Cain, J. Chan, W. J. Chen, J. Cho, E. da Veiga Beltrame, S. Diamantakis, S. Gao, D. Grigoriadis, C. A. Grove, T. W. Harris, R. Kishore, T. Le, R. Y. N. Lee, M. Luypaert, H.-M. Muller, C. Nakamura, P. Nuin, M. Paulini, M. Quinton-Tulloch, D. Raciti, F. H. Rodgers, M. Russell, G. Schindelman, A. Singh, T. Stickland, K. Van Auken, Q. Wang, G. Williams, A. J. Wright, K. Yook, M. Berriman, K. L. Howe, T. Schedl, L. Stein, and P. W. Sternberg, "WormBase in 2022âĂŤdata, processes, and tools for analyzing *Caenorhabditis elegans*," *Genetics*, vol. 220, p. iyac003, Apr. 2022.

[66] W. Kim, R. S. Underwood, I. Greenwald, and D. D. Shaye, "OrthoList 2: A New Comparative Genomic Analysis of Human and *Caenorhabditis elegans* Genes," *Genetics*, vol. 210, pp. 445–461, Oct. 2018.

[67] Z. Altun, L. A. Herndon, C. A. Wolkow, C. Crocker, R. Lints, and D. H. Hall, "WormAtlas," 2002.

[68] G. Juarez, K. Lu, J. Sznitman, and P. E. Arratia, "Motility of small nematodes in wet granular media," *EPL (Europhysics Letters)*, vol. 92, p. 44002, Nov. 2010.

[69] S. Jung, "*Caenorhabditis elegans* swimming in a saturated particulate system," *Physics of Fluids*, vol. 22, p. 031903, Mar. 2010.

[70] S. Park, H. Hwang, S.-W. Nam, F. Martinez, R. H. Austin, and W. S. Ryu, "Enhanced Caenorhabditis elegans Locomotion in a Structured Microfluidic Environment," *PLOS ONE*, vol. 3, p. e2550, June 2008.

[71] C. Fang-Yen, M. Wyart, J. Xie, R. Kawai, T. Kodger, S. Chen, Q. Wen, and A. D. T. Samuel, "Biomechanical analysis of gait adaptation in the nematode *Caenorhabditis elegans*," *Proceedings of the National Academy of Sciences*, vol. 107, pp. 20323–20328, Nov. 2010.

[72] J. Sznitman, Prashant K. Purohit, P. Krajacic, T. Lamitina, and P. E. Arratia, "Material Properties of Caenorhabditis elegans Swimming at Low Reynolds Number," *Biophysical Journal*, vol. 98, pp. 617–626, Feb. 2010.

[73] J. Sznitman, X. Shen, R. Sznitman, and P. E. Arratia, "Propulsive force measurements and flow behavior of undulatory swimmers at low Reynolds number," *Physics of Fluids*, vol. 22, p. 121901, Dec. 2010.

[74] X. Shen, J. Sznitman, P. Krajacic, T. Lamitina, and P. Arratia, "Undulatory Locomotion of Caenorhabditis elegans on Wet Surfaces," *Biophysical Journal*, vol. 102, pp. 2772–2781, June 2012.

[75] X. N. Shen and P. E. Arratia, "Undulatory Swimming in Viscoelastic Fluids," *Physical Review Letters*, vol. 106, p. 208101, May 2011.

[76] F. Lebois, P. Sauvage, C. Py, O. Cardoso, B. Ladoux, P. Hersen, and J.-M. Di Meglio, "Locomotion Control of Caenorhabditis elegans through Confinement," *Biophysical Journal*, vol. 102, pp. 2791–2798, June 2012.

[77] A. Bilbao, E. Wajnryb, S. A. Vanapalli, and J. Blawzdziewicz, "Nematode locomotion in unconfined and confined fluids," *Physics of Fluids*, vol. 25, p. 081902, Aug. 2013.

[78] J. Hodgkin and T. Doniach, "Natural Variation and Copulatory Plug Formation in *Caenorhabditis elegans*," *Genetics*, vol. 146, pp. 149–164, May 1997.

[79] M.-A. Felix and F. Duveau, "Population dynamics and habitat sharing of natural populations of Caenorhabditis elegans and C. briggsae," *BMC Biology*, vol. 10, p. 59, Dec. 2012.

[80] N. Cohen and T. Ranner, "A new computational method for a model of C. elegans biomechanics: Insights into elasticity and locomotion performance," 2017. Publisher: arXiv Version Number: 1.

[81] E. Niebur and P. Erdos, "Theory of the locomotion of nematodes," *Biophysical Journal*, vol. 60, pp. 1132–1146, Nov. 1991.

[82] P. Sauvage, M. Argentina, J. Drappier, T. Senden, J. Simeon, and J.-M. Di Meglio, "An elasto-hydrodynamical model of friction for the locomotion of Caenorhabditis elegans," *Journal of Biomechanics*, vol. 44, pp. 1117–1122, Apr. 2011.

[83] B. Thomases and R. D. Guy, "Mechanisms of Elastic Enhancement and Hindrance for Finite-Length Undulatory Swimmers in Viscoelastic Fluids," *Physical Review Letters*, vol. 113, p. 098102, Aug. 2014.

[84] V. Padmanabhan, Z. S. Khan, D. E. Solomon, A. Armstrong, K. P. Rumbaugh, S. A. Vanapalli, and J. Blawzdziewicz, "Locomotion of C. elegans: A Piecewise-Harmonic Curvature Representation of Nematode Behavior," *PLoS ONE*, vol. 7, p. e40121, July 2012.

[85] J. Karbowski, C. J. Cronin, A. Seah, J. E. Mendel, D. Cleary, and P. W. Sternberg, "Conservation rules, their breakdown, and optimality in Caenorhabditis sinusoidal locomotion," *Journal of Theoretical Biology*, vol. 242, pp. 652–669, Oct. 2006.

[86] J. Bryden and N. Cohen, "Neural control of Caenorhabditis elegans forward locomotion: the role of sensory feedback," *Biological Cybernetics*, vol. 98, pp. 339–351, Apr. 2008.

[87] J. Karbowski, G. Schindelman, C. J. Cronin, A. Seah, and P. W. Sternberg, "Systems level circuit model of C. elegans undulatory locomotion: mathematical modeling and molecular genetics," *Journal of Computational Neuroscience*, vol. 24, pp. 253–276, June 2008.

[88] J. H. Boyle, S. Berri, and N. Cohen, "Gait Modulation in C. elegans: An Integrated Neuromechanical Model," *Frontiers in Computational Neuroscience*, vol. 6, Mar. 2012.

[89] T. D. Montenegro-Johnson, D. A. Gagnon, P. E. Arratia, and E. Lauga, "Flow analysis of the low Reynolds number swimmer *C. elegans*," *Physical Review Fluids*, vol. 1, p. 053202, Sept. 2016.

[90] A. Bilbao, A. K. Patel, M. Rahman, S. A. Vanapalli, and J. Blawzdziewicz, "Roll maneuvers are essential for active reorientation of *Caenorhabditis elegans* in 3D media," *Proceedings of the National Academy of Sciences*, vol. 115, Apr. 2018.

[91] D. A. Gagnon and T. D. Montenegro-Johnson, "Thrifty swimming with shear-thinning," *The ANZIAM Journal*, vol. 59, pp. 443–454, Apr. 2018.

[92] Z. Yu, J. Zhan, H. Wang, H. Zheng, J. Xie, and X. Wang, "Analysis of Influencing Factors on Viscosity of Agar Solution for Capsules," *Journal of Physics: Conference Series*, vol. 1653, p. 012059, Oct. 2020.

[93] M. Backholm, A. K. S. Kasper, R. D. Schulman, W. S. Ryu, and K. Dalnoki-Veress, "The effects of viscosity on the undulatory swimming dynamics of C. elegans," *Physics of Fluids*, vol. 27, p. 091901, Sept. 2015.

[94] P. Krajacic, X. Shen, P. K. Purohit, P. Arratia, and T. Lamitina, "Biomechanical Profiling of *Caenorhabditis elegans* Motility," *Genetics*, vol. 191, pp. 1015–1021, July 2012.

[95] J. H. Boyle, S. Berri, M. Tassieri, I. A. Hope, and N. Cohen, "Gait Modulation in C. Elegans: It's Not a Choice, It's a Reflex!," *Frontiers in Behavioral Neuroscience*, vol. 5, Mar. 2011.

[96] L. Parida, U. U. Ghosh, and V. Padmanabhan, "The effects of groove height and substrate stiffness on C. elegans locomotion," *Journal of Biomechanics*, vol. 55, pp. 34–40, Apr. 2017.

[97] R. S. Berman, O. Kenneth, J. Sznitman, and A. M. Leshansky, "Undulatory locomotion of finite filaments: lessons from *Caenorhabditis elegans*," *New Journal of Physics*, vol. 15, p. 075022, July 2013.

[98] E. K. Towlson, P. E. Vertes, S. E. Ahnert, W. R. Schafer, and E. T. Bullmore, "The Rich Club of the C. elegans Neuronal Connectome," *Journal of Neuroscience*, vol. 33, pp. 6380–6387, Apr. 2013.

[99] N. Cohen and J. E. Denham, "Whole animal modeling: piecing together nematode locomotion," *Current Opinion in Systems Biology*, vol. 13, pp. 150–160, Feb. 2019.

[100] Q. Wen, M. D. Po, E. Hulme, S. Chen, X. Liu, S. Kwok, M. Gershow, A. Leifer, V. Butler, C. Fang-Yen, T. Kawano, W. Schafer, G. Whitesides, M. Wyart, D. Chklovskii, M. Zhen, and A. Samuel, "Proprioceptive Coupling within Motor Neurons Drives C. elegans Forward Locomotion," *Neuron*, vol. 76, pp. 750–761, Nov. 2012.

[101] J. E. Denham, T. Ranner, and N. Cohen, "Signatures of proprioceptive control in *Caenorhabditis elegans* locomotion," *Philosophical Transactions of the Royal Society B: Biological Sciences*, vol. 373, p. 20180208, Oct. 2018.

[102] Y. Zheng, P. J. Brockie, J. E. Mellem, D. M. Madsen, and A. V. Maricq, "Neuronal Control of Locomotion in C. elegans Is Modified by a Dominant Mutation in the GLR-1 Ionotropic Glutamate Receptor," *Neuron*, vol. 24, pp. 347–361, Oct. 1999.

[103] G. J. Stephens, B. Johnson-Kerner, W. Bialek, and W. S. Ryu, "Dimensionality and Dynamics in the Behavior of C. elegans," *PLoS Computational Biology*, vol. 4, p. e1000028, Apr. 2008.

[104] A. E. X. Brown, E. I. Yemini, L. J. Grundy, T. Jucikas, and W. R. Schafer, "A dictionary of behavioral motifs reveals clusters of genes affecting *Caenorhabditis elegans* locomotion," *Proceedings of the National Academy of Sciences*, vol. 110, pp. 791–796, Jan. 2013.

[105] L. Deng, J. E. Denham, C. Arya, O. Yuval, N. Cohen, and G. Haspel, "Inhibition Underlies Fast Undulatory Locomotion in *Caenorhabditis elegans*," *eneuro*, vol. 8, pp. ENEURO.0241–20.2020, Mar. 2021.

[106] T. Kaletta and M. O. Hengartner, "Finding function in novel targets: C. elegans as a model organism," *Nature Reviews Drug Discovery*, vol. 5, pp. 387–399, May 2006.

[107] E. Culetto, "A role for Caenorhabditis elegans in understanding the function and interactions of human disease genes," *Human Molecular Genetics*, vol. 9, pp. 869–877, Apr. 2000.

[108] C. E. Lee, K. S. Singleton, M. Wallin, and V. Faundez, "Rare Genetic Diseases: Nature's Experiments on Human Development," *iScience*, vol. 23, p. 101123, May 2020.

[109] C. Gonzaga-Jauregui, J. R. Lupski, and R. A. Gibbs, "Human Genome Sequencing in Health and Disease," *Annual Review of Medicine*, vol. 63, pp. 35–61, Feb. 2012.

[110] S. A. Patten, D. Aggad, J. Martinez, E. Tremblay, J. Petrillo, G. A. Armstrong, A. La Fontaine, C. Maios, M. Liao, S. Ciura, X.-Y. Wen, V. Rafuse, J. Ichida, L. Zinman, J.-P. Julien, E. Kabashi, R. Robitaille, L. Korngut, J. A. Parker, and P. Drapeau, "Neuroleptics as therapeutic compounds stabilizing neuromuscular transmission in amyotrophic lateral sclerosis," *JCI Insight*, vol. 2, p. e97152, Nov. 2017.

[111] D. D. Shaye and I. Greenwald, "OrthoList: A Compendium of C. elegans Genes with Human Orthologs," *PLOS ONE*, vol. 6, p. e20085, May 2011.

[112] T. Stiernagle, "Maintenance of C. elegans," *WormBook*, 2006.

[113] I. Barlow, "Bleach synchronisation of C. elegans v1," tech. rep., Aug. 2019. Type: dataset.

[114] P. Islam, "Preparing worms for the COPAS (wormsorter) v1," tech. rep., Apr. 2020. Type: dataset.

[115] S. Moore and I. Barlow, "COPAS wormsorter v1," tech. rep., Apr. 2020. Type: dataset.

[116] I. Barlow, "Disease model screen protocol v1," tech. rep., Feb. 2021. Type: dataset.

[117] I. Barlow, L. Feriani, E. Minga, A. McDermott-Rouse, T. O'Brien, Z. Liu, M. Hofbauer, J. R. Stowers, E. C. Andersen, S. S. Ding, and A. E. Brown, "Megapixel camera arrays for high-resolution animal tracking in multiwell plates," preprint, Animal Behavior and Cognition, Apr. 2021.

[118] S. L. Edwards, N. K. Charlie, M. C. Milfort, B. S. Brown, C. N. Gravlin, J. E. Knecht, and K. G. Miller, "A Novel Molecular Solution for Ultraviolet Light Detection in Caenorhabditis elegans," *PLoS Biology*, vol. 6, p. e198, Aug. 2008.

[119] M. A. Churgin, S.-K. Jung, C.-C. Yu, X. Chen, D. M. Raizen, and C. Fang-Yen, "Longitudinal imaging of Caenorhabditis elegans in a microfabricated device reveals variation in behavioral decline during aging," *eLife*, vol. 6, p. e26652, May 2017.

[120] R. Shingai, M. Furudate, K. Hoshi, and Y. Iwasaki, "Evaluation of Head Movement Periodicity and Irregularity during Locomotion of Caenorhabditis elegans," *Frontiers in Behavioral Neuroscience*, vol. 7, 2013.

[121] S. Maguire, C. Clark, J. Nunnari, J. Pirri, and M. Alkema, "The C. elegans Touch Response Facilitates Escape from Predacious Fungi," *Current Biology*, vol. 21, pp. 1326–1330, Aug. 2011.

[122] D. J. Reiner, E. M. Newton, H. Tian, and J. H. Thomas, "Diverse behavioural defects caused by mutations in Caenorhabditis elegans unc-43 CaM Kinase II," *Nature*, vol. 402, pp. 199–203, Nov. 1999.

[123] T. Akita, K. Aoto, M. Kato, M. Shiina, H. Mutoh, M. Nakashima, I. Kuki, S. Okazaki, S. Magara, T. Shiihara, K. Yokochi, K. Aiba, J. Tohyama, C. Ohba, S. Miyatake, N. Miyake, K. Ogata, A. Fukuda, N. Matsumoto, and H. Saitsu, "De novo variants in CAMK 2A and CAMK 2B cause neurodevelopmental disorders," *Annals of Clinical and Translational Neurology*, vol. 5, pp. 280–296, Mar. 2018.

[124] B. A. Bamber, A. A. Beg, R. E. Twyman, and E. M. Jorgensen, "The *Caenorhabditis elegans unc-49* Locus Encodes Multiple Subunits of a Heteromultimeric GABA Receptor," *The Journal of Neuroscience*, vol. 19, pp. 5348–5359, July 1999.

[125] C. J. Locke, K. A. Caldwell, and G. A. Caldwell, "The Nematode, Caenorhabditis elegans, as an Emerging Model for Investigating Epilepsy," in *Animal Models of Epilepsy* (S. C. Baraban, ed.), vol. 40, pp. 1–25, Totowa, NJ: Humana Press, 2009. Series Title: Neuromethods.

[126] S. Q. Wong, A. Jones, S. Dodd, D. Grimes, J. W. Barclay, A. G. Marson, V. T. Cunliffe, R. D. Burgoyne, G. J. Sills, and A. Morgan, "A Caenorhabditis elegans assay of seizure-like activity optimised for identifying antiepileptic drugs and their mechanisms of action," *Journal of Neuroscience Methods*, vol. 309, pp. 132–142, Nov. 2018.

[127] J. H. Hartman, L. L. Smith, K. L. Gordon, R. Laranjeiro, M. Driscoll, D. R. Sherwood, and J. N. Meyer, "Swimming Exercise and Transient Food Deprivation in Caenorhabditis elegans Promote Mitochondrial Maintenance and Protect Against Chemical-Induced Mitotoxicity," *Scientific Reports*, vol. 8, p. 8359, Dec. 2018.

[128] H.-S. Chuang, W.-J. Kuo, C.-L. Lee, I.-H. Chu, and C.-S. Chen, "Exercise in an electrotactic flow chamber ameliorates age-related degeneration in Caenorhabditis elegans," *Scientific Reports*, vol. 6, p. 28064, Sept. 2016.

[129] R. Laranjeiro, G. Harinath, J. E. Hewitt, J. H. Hartman, M. A. Royal, J. N. Meyer, S. A. Vanapalli, and M. Driscoll, "Swim exercise in *Caenorhabditis elegans* extends neuromuscular and gut healthspan, enhances learning ability, and protects against neurodegeneration," *Proceedings of the National Academy of Sciences*, vol. 116, pp. 23829–23839, Nov. 2019.

Appendix A

Derivations, notes and calculations

A.1 Invertible linear system for rigid body motion calculation

The shape of the undulator is given by

$$\boldsymbol{x}(s,t) = \begin{bmatrix} x(s,t) \\ \\ z(s,t) \end{bmatrix} = \boldsymbol{x}_0(t) + \boldsymbol{R}(\theta(t))\boldsymbol{r}(s,t) \tag{A.1}$$

with $\boldsymbol{R}(\theta(t))$ the rotation matrix:

$$\boldsymbol{R}(\theta(t)) = \begin{bmatrix} \cos(\theta(t)) & -\sin(\theta(t)) \\ \\ \sin(\theta(t)) & \cos(\theta(t)) \end{bmatrix}. \tag{A.2}$$

Thus the unit tangent vector along the body is given by

$$\hat{\boldsymbol{t}}(s,t) = \begin{bmatrix} \hat{t}_x(s,t) \\ \\ \hat{t}_z(s,t) \end{bmatrix} = \frac{\partial \boldsymbol{x}}{\partial s} = \boldsymbol{R}\frac{\partial \boldsymbol{R}}{\partial t} \tag{A.3}$$

and the velocity is given by

$$\boldsymbol{u}(s,t) = \begin{bmatrix} u_x(s,t) \\ \\ u_z(s,t) \end{bmatrix} = \frac{\partial \boldsymbol{x}}{\partial t} = \dot{\boldsymbol{x}}_0(t) + \dot{\theta}(t)\frac{\mathrm{d}\boldsymbol{R}}{\mathrm{d}\theta}\boldsymbol{r}(s,t) + \boldsymbol{R}\frac{\partial \boldsymbol{r}}{\partial t}. \tag{A.4}$$

Explicitly, the terms that comprise this expression for the velocity: $\dot{\boldsymbol{x}}_0$, $\dot{\theta}(\mathrm{d}\boldsymbol{R}/\mathrm{d}\theta)\boldsymbol{r}$, and $\boldsymbol{R}\partial\boldsymbol{r}/\partial t$, are respectively: the translational velocity, the angular velocity (ie velocity due to rotations of the body), and the velocity due to undulations (ie changes in shape).

The fluid–body interactions are modelled by local resistive force theory. The force per unit length of the body is separated into tangential and normal components:

$$\boldsymbol{f}\cdot\hat{\boldsymbol{t}} = K_T\boldsymbol{u}\cdot\hat{\boldsymbol{t}}\,, \quad \boldsymbol{f}\cdot\hat{\boldsymbol{n}} = K_N\boldsymbol{u}\cdot\hat{\boldsymbol{n}} \tag{A.5}$$

where $\hat{\boldsymbol{n}} = \hat{\boldsymbol{t}}^{\perp}$ the unit normal vector, and K_T, K_N the tangential and normal resistance coefficients respectively. The force per unit length is thus given by

$$\boldsymbol{f}(s,t) = K_T\hat{\boldsymbol{t}}\hat{\boldsymbol{t}}^T\boldsymbol{u} + K_N(\boldsymbol{I} - \hat{\boldsymbol{t}}\hat{\boldsymbol{t}}^T)\boldsymbol{u} \tag{A.6}$$

$$= (K_T - K_N)\,\hat{\boldsymbol{t}}\,(\hat{\boldsymbol{t}}\cdot\hat{\boldsymbol{u}}) + K_N\,\boldsymbol{u}\,. \tag{A.7}$$

As required by the resistive force model, we impose the condition of zero net-force:

$$\int_0^L \boldsymbol{f}(s,t)\,\mathrm{d}s = 0, \tag{A.8}$$

and zero net-torque:

$$\int_0^L [\boldsymbol{x}(s,t) - \boldsymbol{x}_0(t)] \times \boldsymbol{f}(s,t)\,\mathrm{d}s = 0 \tag{A.9}$$

which is equivalent to

$$\int_0^L \boldsymbol{R}\boldsymbol{r}(s,t) \times \boldsymbol{f}(s,t)\,\mathrm{d}s = 0. \tag{A.10}$$

We will now confirm that the conditions of zero net force and zero net torque are linear in the velocities $\dot{x}_0(t), \dot{z}_0(t), \dot{\theta}(t)$.

To simplify notation, we denote some terms that appear in (A.1) or (A.4) as follows:

$$\frac{\mathrm{d}\boldsymbol{R}}{\mathrm{d}\theta}\boldsymbol{r}(s,t) =: \boldsymbol{d}(s,t) = \begin{bmatrix} d_x(s,t) \\ d_z(s,t) \end{bmatrix}, \tag{A.11}$$

$$\boldsymbol{R}\frac{\partial \boldsymbol{r}}{\partial t} =: \boldsymbol{v}(s,t) = \begin{bmatrix} v_x(s,t) \\ v_z(s,t) \end{bmatrix}, \tag{A.12}$$

$$\boldsymbol{R}\boldsymbol{r}(s,t) =: \boldsymbol{D}(s,t) = \begin{bmatrix} D_x(s,t) \\ D_z(s,t) \end{bmatrix}. \tag{A.13}$$

The zero net force condition (A.8) can be written separated into x and z components. The x component for this condition can be written as

$$\int_0^L \left[(K_T - K_N)\hat{t}_x(\hat{t}_x u_x + \hat{t}_z u_z) + K_N u_x\right]\mathrm{d}s = 0 \tag{A.14}$$

which can be expanded on the LHS to say

$$\int_0^L \left[(K_T - K_N)\hat{t}_x(\hat{t}_x[\dot{x}_0 + \dot{\theta} d_x + v_x] + \hat{t}_z[\dot{z}_0 + \dot{\theta} d_z + v_z]) + K_N(\dot{x}_0 + \dot{\theta} d_x + v_x)\right]\mathrm{d}s = 0. \tag{A.15}$$

Similarly, the z component for this condition is

$$\int_0^L \left[(K_T - K_N)\hat{t}_z(\hat{t}_x u_x + \hat{t}_z u_z) + K_N u_z\right] \mathrm{d}s = 0 \tag{A.16}$$

which can be expanded on the LHS to say

$$\int_0^L \left[(K_T - K_N)\hat{t}_z(\hat{t}_x[\dot{x}_0 + \dot{\theta} d_x + v_x] + \hat{t}_z[\dot{z}_0 + \dot{\theta} d_z + v_z]) + K_N(\dot{z}_0 + \dot{\theta} d_z + v_z)\right] \mathrm{d}s = 0. \tag{A.17}$$

The zero net torque condition (A.10) can be written as

$$\begin{aligned} \int_0^L \big[& D_x([K_T - K_N]\hat{t}_z[\hat{t}_x u_x + \hat{t}_z u_z] + K_N u_z) \\ & - D_z([K_T - K_N]\hat{t}_z[\hat{t}_x u_x + \hat{t}_z u_z] + K_N u_x)\big] \mathrm{d}s \\ & = 0 \end{aligned} \tag{A.18}$$

which can be expanded on the LHS to say

$$\begin{aligned} \int_0^L \big[& D_x([K_T - K_N]\hat{t}_z[\hat{t}_x(\dot{x}_0 + \dot{\theta} d_x + v_x) + \hat{t}_z(\dot{z}_0 + \dot{\theta} d_z + v_z)] + K_N[\dot{z}_0 + \dot{\theta} d_z + v_z]) \\ & - D_z([K_T - K_N]\hat{t}_x[\hat{t}_x(\dot{x}_0 + \dot{\theta} d_x + v_x) + \hat{t}_z(\dot{z}_0 + \dot{\theta} d_z + v_z)] + K_N[\dot{x}_0 + \dot{\theta} d_x + v_x])\big] \mathrm{d}s \\ & = 0. \end{aligned} \tag{A.19}$$

We can rearrange (A.15), (A.17), and (A.19) to be in the form of

$$\dot{x}_0 A_1 + \dot{z}_0 A_2 + \dot{\theta} A_3 = b \tag{A.20}$$

and hence find the entries of the matrix $\boldsymbol{A} \in \mathbb{R}^{3\times 3}$ and vector $\boldsymbol{b} \in \mathbb{R}^3$ in the linear

system

$$\boldsymbol{A}\begin{bmatrix}\dot{x}_0\\ \dot{z}_0\\ \dot{\theta}\end{bmatrix} = \boldsymbol{b}. \tag{A.21}$$

Rearranging (A.15) in this way gives

$$\begin{aligned}\dot{x}_0 \underbrace{\int_0^L \left[(K_N - K_T)\hat{t}_x\hat{t}_x + K_N\right]\mathrm{d}s}_{A_{11}} + \dot{z}_0 \underbrace{\int_0^L \left[(K_N - K_T)\hat{t}_x\hat{t}_z\right]\mathrm{d}s}_{A_{12}} \\ + \dot{\theta}\underbrace{\int_0^L \left[(K_T - K_N)\hat{t}_x(\hat{\boldsymbol{t}}\cdot\boldsymbol{d}) + K_N d_x\right]\mathrm{d}s}_{A_{13}} \\ = \underbrace{-\int_0^L \left[(K_T - K_N)\hat{t}_x(\hat{\boldsymbol{t}}\cdot\boldsymbol{v}) + K_N v_x\right]\mathrm{d}s}_{b_1}.\end{aligned} \tag{A.22}$$

Rearranging (A.17) gives

$$\begin{aligned}\dot{x}_0 \underbrace{\int_0^L \left[(K_N - K_T)\hat{t}_z\hat{t}_x\right]\mathrm{d}s}_{A_{21}} + \dot{z}_0 \underbrace{\int_0^L \left[(K_N - K_T)\hat{t}_z\hat{t}_z + K_N\right]\mathrm{d}s}_{A_{22}} \\ + \dot{\theta}\underbrace{\int_0^L \left[(K_T - K_N)\hat{t}_z(\hat{\boldsymbol{t}}\cdot\boldsymbol{d}) + K_N d_z\right]\mathrm{d}s}_{A_{23}} \\ = \underbrace{-\int_0^L \left[(K_T - K_N)\hat{t}_z(\hat{\boldsymbol{t}}\cdot\boldsymbol{v}) + K_N v_z\right]\mathrm{d}s}_{b_2}.\end{aligned} \tag{A.23}$$

Rearranging (A.19) gives

$$\begin{aligned}
&\dot{x}_0 \underbrace{\int_0^L \left[D_x([K_T-K_N]\hat{t}_z\hat{t}_x)-D_z([K_T-K_N]\hat{t}_x\hat{t}_x+K_N)\right]\mathrm{d}s}_{A_{31}} \\
&+\dot{z}_0 \underbrace{\int_0^L \left[D_x([K_T-K_N]\hat{t}_z\hat{t}_z+K_N)-D_z([K_T-K_N]\hat{t}_x\hat{t}_z)\right]\mathrm{d}s}_{A_{32}} \\
&+\dot{\theta} \underbrace{\int_0^L \left[D_x([K_T-K_N]\hat{t}_z[\hat{\boldsymbol{t}}\cdot\boldsymbol{d}]+K_N d_z)-D_z([K_T-K_N]\hat{t}_x[\hat{\boldsymbol{t}}\cdot\boldsymbol{d}]+K_N d_x)\right]\mathrm{d}s}_{A_{33}} \\
&=\underbrace{-\int_0^L \left[D_x([K_T-K_N]\hat{t}_z[\hat{\boldsymbol{t}}\cdot\boldsymbol{v}]+K_N v_z)-D_z([K_T-K_N]\hat{t}_x[\hat{\boldsymbol{t}}\cdot\boldsymbol{v}]+K_N v_x)\right]\mathrm{d}s}_{b_3}.
\end{aligned} \tag{A.24}$$

NB: $A_{12}=A_{21}$.

Hence, if we prescribe the shape of the undulator via the tangent angle $\psi(s,t)$, we obtain the vectors

$$\hat{\boldsymbol{t}}(s,t)=[\cos(\psi),\sin(\psi)]$$

and

$$\boldsymbol{r}(s,t)=\left[\int_0^L \cos(\psi)\,\mathrm{d}s,\int_0^L \sin(\psi)\,\mathrm{d}s\right].$$

From this, we can construct this 3×3 linear system to solve for the translational and angular velocities, and hence calculate the rigid body motion for the undulator.

A.2 ψ vs φ for reducing the swimmer radius of curvature analytical result

In the instantaneous scenario, taking $\theta = 0$ and hence the rotation matrix is taken to be the identity, we have that

$$\boldsymbol{x} = \boldsymbol{x}_0 + \left[\int_0^s \cos(\psi)\mathrm{d}s, \int_0^s \sin(\psi)\mathrm{d}s\right] \tag{A.25}$$

$$\equiv R(1+\epsilon f(\varphi))\big[\cos(\varphi), \sin(\varphi)\big]. \tag{A.26}$$

Let $\hat{\boldsymbol{r}}(\varphi) = [\cos(\varphi), \sin(\varphi)]$, $\hat{\boldsymbol{\varphi}}(\varphi) = [-\sin(\varphi), \cos(\varphi)]$. We take

$$\psi = \frac{s}{R} + \epsilon\tilde{\psi} \tag{A.27}$$

and hence the waveform corresponds to a circle of radius R plus some travelling wave perturbation of size ϵ.

From above we have that

$$\frac{\mathrm{d}\boldsymbol{x}}{\mathrm{d}\varphi} = R(1+\epsilon f(\varphi))\hat{\boldsymbol{\varphi}}(\varphi) + \epsilon R f' \tag{A.28}$$

$$\tag{A.29}$$

where $f' = \mathrm{d}f/\mathrm{d}\varphi$. It follows that

$$\left|\frac{\mathrm{d}\boldsymbol{x}}{\mathrm{d}\varphi}\right|^2 = R^2(1+\epsilon f(\varphi))^2 + \epsilon^2 R^2 f'^2, \tag{A.30}$$

$$\left|\frac{\mathrm{d}\boldsymbol{x}}{\mathrm{d}\varphi}\right| = R[(1+\epsilon f)^2 + \epsilon^2 f'^2]^{\frac{1}{2}}. \tag{A.31}$$

Since

$$\frac{\mathrm{d}\boldsymbol{x}}{\mathrm{d}s} = \frac{\mathrm{d}\boldsymbol{x}}{\mathrm{d}\varphi}\frac{\mathrm{d}\varphi}{\mathrm{d}s} \tag{A.32}$$

and

$$\left|\frac{\mathrm{d}\boldsymbol{x}}{\mathrm{d}s}\right| = 1 \tag{A.33}$$

it follows that

$$\left|\frac{\mathrm{d}\boldsymbol{x}}{\mathrm{d}\varphi}\right| = \frac{\mathrm{d}s}{\mathrm{d}\varphi} \tag{A.34}$$

and hence

$$\frac{\mathrm{d}s}{\mathrm{d}\varphi} = R(1 + 2\epsilon f + O(\epsilon^2))^{\frac{1}{2}} \tag{A.35}$$

$$= R(1 + \epsilon f) + O(\epsilon^2). \tag{A.36}$$

Integrating this expression yields

$$s = R(\varphi - \varphi_0) + \epsilon R \int_0^{\varphi(s)} f(\varphi')\,\mathrm{d}\varphi' + O(\epsilon^2). \tag{A.37}$$

Let

$$g(\varphi) = \int_0^{\varphi(s)} f(\varphi')\,\mathrm{d}\varphi'. \tag{A.38}$$

To determine φ_0, we begin by considering

$$\hat{\boldsymbol{t}} = \frac{\mathrm{d}\boldsymbol{x}}{\mathrm{d}s} = [\cos(\psi), \sin(\psi)]. \tag{A.39}$$

Taking ψ as given by eq. (A.27), we have

$$\cos(\psi) = \cos(s/R) - \epsilon\tilde{\psi}(s)\sin(s/R) + O(\epsilon^2), \tag{A.40}$$

$$\sin(\psi) = \sin(s/R) + \epsilon\tilde{\psi}(s)\cos(s/R) + O(\epsilon^2). \tag{A.41}$$

Using the expression in eq. (A.37) for $s(\varphi)$, we obtain

$$\cos(\psi) = \cos(\varphi - \varphi_0) - \epsilon g(\varphi)\sin(\varphi - \varphi_0) - \epsilon\tilde{\psi}(s)\sin(\varphi - \varphi_0), \tag{A.42}$$

$$\sin(\psi) = \sin(\varphi - \varphi_0) - \epsilon g(\varphi)\cos(\varphi - \varphi_0) - \epsilon\tilde{\psi}(s)\sin(\varphi - \varphi_0). \tag{A.43}$$

Since

$$\hat{\boldsymbol{t}} = \frac{\mathrm{d}\boldsymbol{x}}{\mathrm{d}s} = \frac{\mathrm{d}\boldsymbol{x}}{\mathrm{d}\varphi}\frac{\mathrm{d}\varphi}{\mathrm{d}s} \tag{A.44}$$

and from above

$$\frac{\mathrm{d}\varphi}{\mathrm{d}s} = R^{-1}(1-\epsilon f) + O(\epsilon^2) \tag{A.45}$$

we thus have

$$\hat{\boldsymbol{t}} = \hat{\boldsymbol{\varphi}} + \epsilon f'\hat{\boldsymbol{r}} + O(\epsilon^2) \tag{A.46}$$

$$= \big[-\sin(\varphi), \cos(\varphi)\big] + \epsilon f'\big[\cos(\varphi), \sin(\varphi)\big]. \tag{A.47}$$

Comparing (A.47) with (A.42) and (A.43), we see that

$$\varphi_0 = \frac{-\pi}{2}. \tag{A.48}$$

Hence,

$$f'(\varphi) = -g(\varphi) - \tilde{\psi}(s(\varphi)) \tag{A.49}$$

$$-\frac{\mathrm{d}f}{\mathrm{d}s}\frac{\mathrm{d}s}{\mathrm{d}\varphi} - \int_{-}^{\varphi(s)} f\,\mathrm{d}\varphi = \tilde{\psi}(s(\varphi)) \tag{A.50}$$

$$-\frac{\mathrm{d}f}{\mathrm{d}s}R - \frac{1}{R}\int_0^s f(s)\mathrm{d}s = \tilde{\psi}(s). \tag{A.51}$$